Spectroscopic Investigation of Molecular Probes

by

Sushil Suresh Sakpal
10CC16A26019

A thesis submitted to the
Academy of Scientific & Innovative Research
for the award of the degree of

DOCTOR OF PHILOSOPHY
in
SCIENCE

Under the supervision of
Dr. Sayan Bagchi

CSIR-National Chemical Laboratory, Pune

Academy of Scientific and Innovative Research
AcSIR Headquarters, CSIR-HRDC campus
Sector 19, Kamla Nehru Nagar,
Ghaziabad, U.P. – 201 002, India

September, 2021

Certificate

This is to certify that the work incorporated in this Ph.D. thesis entitled, *"Spectroscopic Investigation of Molecular Probes"*, submitted by *Mr. Sushil Suresh Sakpal* to the Academy of Scientific and Innovative Research (AcSIR) in partial fulfillment of the requirements for the award of the Degree of *Doctor of Philosophy in Science*, embodies original research work carried-out by the student. We, further certify that this work has not been submitted to any other University or Institution in part or full for the award of any degree or diploma. Research material(s) obtained from other source(s) and used in this research work has/have been duly acknowledged in the thesis. Image(s), illustration(s), figure(s), table(s) etc., used in the thesis from other source(s), have also been duly cited and acknowledged.

Sushil Suresh Sakpal
(Research Student)
Date: 08/09/2021

Dr. Sayan Bagchi
(Research Supervisor)
Date:08/09/2021

STATEMENTS OF ACADEMIC INTEGRITY

I Mr. Sushil Suresh Sakpal, a Ph.D. student of the Academy of Scientific and Innovative Research (AcSIR) with Registration No. 10CC16A26019 hereby undertake that, the thesis entitled "Spectroscopic Investigation of Molecular Probes" has been prepared by me and that the document reports original work carried out by me and is free of any plagiarism in compliance with the UGC Regulations on *"Promotion of Academic Integrity and Prevention of Plagiarism in Higher Educational Institutions (2018)"* and the CSIR Guidelines for "*Ethics in Research and in Governance (2020)".*

Signature of the Student
Date : 08/09/2021
Place : Pune

It is hereby certified that the work done by the student, under my/our supervision, is plagiarism-free in accordance with the UGC Regulations on *"Promotion of Academic Integrity and Prevention of Plagiarism in Higher Educational Institutions (2018)"* and the CSIR Guidelines for "*Ethics in Research and in Governance (2020)".*

Signature of the Supervisor
Name : Dr. Sayan Bagchi
Date : 08/09/2021
Place : Pune

This thesis is dedicated to

My parents, Mrs. Shubhangi Sakpal, & Mr. Suresh Sakpal

and, My honorable teacher

Mrs. Meghana Madhav Joshi

for their endless support and inspiration.

Acknowledgment

This dissertation work is a collective effort of many people who have supported and guided me during my Ph.D. tenure. I want to devote my gratitude and appreciation to their valuable contribution during this scientific endeavour.

I would like to express my sincere gratitude to my supervisor Dr. Sayan Bagchi from the CSIR-NCL, Pune, for introducing me to the exciting research world of physical chemistry. His calmness, encouragement, tremendous enthusiasm, criticism, unique approach towards science is inspirational and helped me a lot throughout my Ph.D. tenure. It's a great pleasure for me to work under his guidance which has transformed my scientific approach from the situation of a deer stand in the headlights of an oncoming truck to an independent researcher. I would like to thank Dr. Sayan Bagchi for his support and help given during this thesis work. His wisdom, kindness, and friendly nature towards the students are unforgettable for me.

I owe sincere thanks to my doctoral adviser committee (DAC) members, Dr. Narendra Kadoo, Dr. Kumar Vanka, and Dr. Jayraj Nithyanandhan for their, valuable comments, constructive criticisms which helped me to finish up all projects successfully. My thesis work would have been incomplete without the help of our collaborators. I sincerely thank our collaborator, Dr. Anirban Hazra (IISER Pune), and his student, Dr. Meghna A. Manae. I owe a special thanks to Dr. Anup Ghosh (SNBNCBS Kolkata) and Dr. Bani Kanta Sarma (JNCASR Bangalore) for their productive conversations, helpful comments, and kind suggestions. I extend my sincere thanks to Dr. Anindya Dutta (IIT Bombay) for his help and valuable suggestions. I would liketo acknowledge Dr. Arup Rath for his generous support.

I would like to take this opportunity to point out the help and support obtained from my labmates and friends, Samadhan H. Deshmukh, Srijan Chatterjee, Arathi MB, Shivshankar

Kore, Atul Chakkar during this thesis work. Also, I want to thank Mr. Tapas Haldar, who helped me to develop the expertise in sample preparation and instrument handling. I would particularly like to thank Dr. Deborin Ghosh for the fruitful discussions and help throughout the experiments and data analysis. Special thanks to graduate students from the Bagchi Lab, Dr. Somnath Kashid, Dr. Pranab Deb, and Dr. Madhumita Tarai who contributed to my research growth. I express my special thanks to all my roommates, friends and seniors in NCL for their kind help, support, and best wishes.

I extend my sincere thanks to Dr. Ashwini Kumar Nangia (former Director of CSIR-NCL), Dr. Ashish Lele (current Director of CSIR-NCL), Dr. P. A. Joy (former chair of the Physical and Materials Chemistry Division), Dr. BLV Prasad (former chair of the Physical and Materials Chemistry Division), and Dr. T. G. Ajithkumar (current chair of the Physical and Materials Chemistry Division) for allowing me to access all the instrumental facilities. I express my thanks to the eminent scientists of NCL for enriching me with knowledge and valuable information. I am thankful to the student academic office of NCL for their help in the documentation required for the fellowship and thesis work. I express my sincere acknowledgment to Dr. Sunita Barve, Mr. Gati Krushna Nayak, and other library staff members for the library access. I would also acknowledge NCL staff who have helped me in all the non-research activities throughout my Ph.D. tenure.

I acknowledge the University Grant Commission (UGC) for providing the fellowship to pursue my Ph.D. in CSIR-NCL and the Academy of Scientific and Innovative Research (AcSIR) for allowing me to present my work in the form of a thesis.

I would like to dedicate all achievements to my honorable teachers Mrs. Meghana Madhav Joshi (Former Vice headmistress of K.E.S.G.D. Ambekar high school, Birwadi, Mahad, Raigad) and Mr. Anand Abhyankar (Former Head of Chemistry Department of Dr. Babasaheb Ambedkar college, Mahad, Raigad). I would like to owe my gratitude to my teacher Mrs. Madhura Moghe for her valuable guidance. The guidance and financial support of these teachers opened up a door of higher education for me.

I find no words to express my thanks to my parents Mrs. Shubhangi Sakpal and Mr. Suresh Sakpal, because nothing could have been possible without their love, sacrifices, and encouragement. Most importantly, I would like to thank my younger brother Mr. Sumit Sakpal for his patience and excellent support throughout this work. My sincere gratitude to God Almighty for giving me this life with good friends and relatives in the surrounding.

Sushil Suresh Sakpal

Table of Contents

List of Tables

List of Figures

Chapter 1

Introduction

Structure-function relationships are fundamental to molecular systems irrespective of their size and composition. Interactions and dynamics are key to the structure-function relation. So, it is imperative to understand the role of interactions and dynamics on how a certain structure is related to function. Although there are numerous ways of solving this central dogma of science, broadly speaking, we can either take the theoretical route or the experimental route. Each route has its own advantage and disadvantage. Theoretical calculations and simulations provide a molecular picture of the process. However, these approximation based results need to be validated from experiments. On the other hand, experiments provide results devoid of assumptions, but cannot provide the molecular level understanding of the processes. Being a chemist, I prefer to be able to visualize the processes and this cannot be achieved sole from a single experiment.

In this context, the ideal situation is the bridge the gap between theory and experiment such that the experimental results can be explained at a molecular level on the basis on theory. Spectroscopy, in my opinion, is an ideal way to bridge theory and experiment. The experimental observables, when compared with the exact same parameters obtained from theory, can open up a new avenue to understand structure-function relationships from a macroscopic to microscopic level. Spectroscopy involves light-matter interactions where the frequency of the light can be widely tuned depending upon the problem we would like to address. The huge frequency range of the electromagnetic spectrum provides us an opportunity to perform various spectroscopies.

Molecular probes and spectroscopy are inter-related. These probes differ depending on the choice of the spectroscopic technique involved. Several dyes are used a probe in UV-visible absorption spectroscopy and fluorescence spectroscopy. The sensitivity of these dyes to the environment allows us to decipher the surrounding of the molecule. On the other hand, vibrational infrared probes provide bond-specific local information. Certain properties are

essential for the moiety to perform as a good spectroscopic molecular probe. First, the spectroscopic signal of the probe must be present in an uncluttered region, i.e. where the background absorption is negligible. The spectroscopic transitions must have high extinction coefficient. The probe must be sensitive to its local surrounding such as hydrogen bonding, electrostatic field, or protonation-deprotonation states (pH). The variation in such factors must be manifested as a change in intensity, peak maxima, peak width, or other spectral features which can be quantified. In addition, the small moieties are preferably used as spectroscopic probes which minimally perturb to the system. Furthermore, preferably the transition of the molecule should not be coupled with other parts of molecules. In case such a coupling is present, it might be extremely difficult to decipher the molecular picture from the complex spectrum. Last, but not the least, the observable associated to the molecular probe should be obtainable directly both from experiments and theory.

1.1 Different forms of spectroscopy

Based on the light-matter interaction, spectroscopy is mainly classified into absorption and emission spectroscopy. UV-Visible spectroscopy is an absorption type of spectroscopy that pertains to the measurement and interpretation of discrete wavelengths of UV or visible light absorbed by or transmitted through a sample. In this spectroscopy, the light of a particular wavelength region (200-800 nm) is absorbed by the molecules causes the excitation of the electrons from the ground state to a higher energy state. Molecules containing π-electrons or non-bonding electrons can absorb UV or visible light to excite these electrons to higher anti-bonding molecular orbitals. The selection of a particular excited state for the transition mainly depends on the wavelength of absorbed light. The four possible types of UV-Vis transition (π–π*, n–π*, σ–σ*, and n–σ*) are shown in the Figure 1.1a. UV-Vis spectroscopic data is commonly represented as a plot of absorbance vs wavelength. This simple and versatile spectroscopic technique is widely used in various applications.[1-4]

Fluorescence spectroscopy is emission spectroscopy that analyzes the fluorescence properties of compounds that are either showing native fluorescence or that have been labeled using an appropriate fluorophore. In this spectroscopy, molecules are excited with a light of a suitable wavelength which further emits the radiation at longer wavelengths within its emission band. Different processes involved in the fluorescence mechanism are shown in Figure 1.1b. The excitation energy provided to the molecule promotes it from the ground electronic state to one of the several vibrational states of the excited electronic state. Due to the collisions with other molecules, the excited molecules decay to the lowest vibrational state of the excited electronic state. These molecules relax back to the several vibrational levels in the ground electronic state via a radiative emission known as fluorescence. Fluorescence detection offers the detection and quantification of very low analyte concentration in the range of nM to pM. The high levels of sensitivity and specificity make it an important technique for various applications.[5-8]

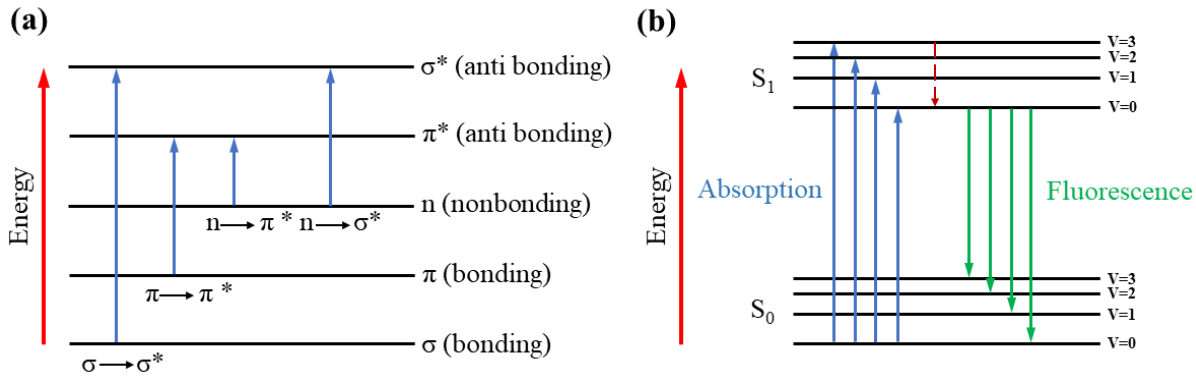

Figure 1.1 (a) Transition involved in the UV-Visible spectroscopy. (b) Various processes involved in the fluorescence spectroscopy.

Unlike UV-visible and fluorescence spectroscopy, Infrared (IR) spectroscopy deals with much smaller energy transitions that occur between various vibrational and rotational states. The absorption-based data acquisition method is generally used in IR spectroscopy. IR spectroscopy is commonly employed in the determination of molecular structure, qualitative

and quantitative analysis of chemical species.[9-12] A change in the dipole moment is a necessary condition for the molecular vibrations to absorb IR radiation. The frequency of the absorbed radiation depends on the bond strength of the bond or group that vibrates. Since bond-specific vibrations absorb at particular vibrational frequencies, each molecule has a characteristic IR spectrum. The infrared portion of the electromagnetic spectrum is usually classified into the near (14000-4000 cm^{-1}), mid (4000-400 cm^{-1}) and far-infrared (400-10 cm^{-1}) regions. The IR spectroscopic analysis used in this thesis is focused on the mid-infrared region.

Similar to IR spectroscopy, Raman spectroscopy is another form of vibrational spectroscopy which is based on the scattering of light. The Raman effect occurs at inelastic scattering, where the wavelength of scattered light is different from that of the incident light. Although both are vibrational spectroscopy, IR spectroscopy senses a change in dipole moments while Raman spectroscopy observes a change in the polarizability of a molecular bond. The Raman active modes are the bond vibrations that are subjected to a change in the molecular bond polarizability. In contrast to IR spectroscopy, Raman spectroscopy is used to analyze the homonuclear diatomic molecules due to changes in polarizability. Raman spectroscopy is versatile tool for various qualitative and quantitative analysis of chemical structure.[13-15]

Although the intrinsic spectroscopic signal or macroscopic observable of system under interest can provide global information about the system, the microscopic environment remains unexplored. Recently, molecular level understanding of interactions and dynamics has been elucidated by using site-specific probes in various spectroscopic measurements.

1.2 Molecular probes - proxy to interaction and dynamics

Fluorescence and infrared (IR) spectroscopy have generally used the molecular probes which provide the valuable insight about the specific function of biological systems.[16-21] In recent years, fluorescent probes are commonly used in the biophysical reasearch due to its versatility, sensitivity, quantitative ability.[22-23] The fluorescent probes senses binding with a specific target which manifest as the significant enhancement in its fluorescent properties.[24] In addition, fluorescent probes also used to explore the solvent effect on chemical processes due to its sensitivity to solvent polarity.[25] IR probes are highly sensitive to surrounding environment and widely employed as site-specific vibrational reporters to investigate the local electrostatics and dynamics, and hydrogen-bonding environments.[26-29] Recently, there has been a surge in the use of an modified unnatural amino acids and nucleosides containing small IR probes,[30] which inserted into the specific site of proteins and DNAs.

Theoretical and computational studies of molecular probes are complementary and supportive to experimental measurements. Theoretical and computational methods are also used to understand the structure and function of chemical and biological systems with its ability of prediction and validation of different hypotheses by characterizing various states of molecules. The Density Functional Theory (DFT) is commonly employed in the investigation of structural, vibrational and optical properties of various materials.[31] The infrared and raman spectroscopies in tandem with a quantum chemical calculations have been used in the vibrational analysis of molecular systems.[32] In addition, atomistic molecular dynamics (MD) simulation is an essential tool to investigate several processes which is responsible for the biomolecular function.[33-35] Prof. Martin Karplus, Michael Levitt and Arieh Warshel (Nobel laureates in chemistry, 2013) showed the importance of quantum chemical methods in the study of metalloenzymes.

1.3 Spectroscopic experiments used in tandem with theoretical calculations

Traditionally, the study of chemical and biological materials mainly focussed on the characterization of the bulk structure and properties of molecules; hence the microscopic structures of molecules remain poorly understood. Sometimes, experimental methods alone are not sufficient to recognize the intermediate transition states responsible for the function of molecules in chemical or biological processes. In this thesis, we have obtained meaningful insight about the system with the combination of experiments and theoretical methods that would not be possible to achieve with the use of two approaches independently.

Recently, computational chemistry has made considerable advances in chemistry and biology. Dentistry Functional Theory (DFT) provides a wealth of information about the structural and spectral properties of the molecules and plays a crucial role in studying molecular structures and their interactions.[36-37] Furthermore, the Time-dependent DFT (TD-DFT) method is commonly used to compute the UV–vis spectra and excited states properties of molecules.[38] In this thesis, TD-DFT calculations complement the experimental results that have been used to reveal a photophysics of warfarin, a fluorophore and anticoagulant drug in biology.

In the condensed phase, atoms are in constant motion, and the dynamics of these molecules have a profound effect on the desired molecular function and intermolecular interactions. Unfortunately, the experimental techniques cannot observe the motions of individual atoms/molecules, but the molecular dynamics (MD) simulation can discriminate the underlying dynamics. When a solute dissolves in a solvent mixture, then the solute is preferentially solvated by a particular component of the mixture. It has been reported that the local solvation structure of the solute molecule in the mixed solvent can be different from that found in the bulk solution.[39-40] Herein, we have added a solute in viscous deep

eutectic solvent (Reline) and measure the effect of water addition on the microscopic structure of reline through the dissolved solute perspective. In this study, MD simulation in combination with vibrational spectroscopy has been used to identify various solute-solvent interactions, further indicating the solute perspective maximum extent of hydration for a deep eutectic solvent.

1.4 Multiple spectroscopic approaches used in tandem

In certain circumstances, a single spectroscopic method cannot provide information about the specific characteristics of the molecules. Spectral analysis of systems in combination with different spectroscopic approaches is a possible solution to such problems. The combined spectroscopic measurements offer detailed information about the system.

Vibrational frequencies are highly sensitive to local environments, so IR probes are used as a site-specific marker in a simple and complex system. The infrared (IR) probe often suffers from an unexpected complex absorptive line shape due to the Fermi resonance between a fundamental band and a nearest resonant overtone/combination band. Depending on the surrounding environment, Fermi resonance exhibits overlapping peaks or distinct spectral features in the IR spectrum.[41-42] Isotopic substitution is a possible method to verify the existence of Fermi resonance but it also has a limitation, such as substituted compounds may not be readily available.

Multidimensional ultrafast vibrational spectroscopy provides additional information than the FTIR experiments. Two dimensional IR (2D IR) spectroscopy measure the temporal evolution of vibrational frequencies at a sub-picosecond timescale. The combination of high temporal resolution and bond-specific vibrations makes it a promising tool for studying molecular interactions and dynamics. We have used one of the characteristics of 2D-IR spectroscopy, the detection of off-diagonal cross-peaks, which reveal the presence of Fermi

resonance and differential solvation dyanamics for the ester carbonyl vibrational probes in protic solvents.

This thesis includes spectroscopic responses of different molecular probes including fluorescent as well as vibrational probes in small molecules and proteins. The use of just one spectroscopic technique at times fails to provide an unambiguous understanding of the system. It has been shown here that multiple spectroscopic techniques when used in tandem with theoretical calculations can remove any ambiguity and provide a conclusive understanding of the system. Depending on the size of the solute and the viscosity of the solvent, the frequency evolution of the solute depends on the solvent's fluctuations as well as the inherent reorientation dynamics of the solute. Here, we show that a polarization dependent spectroscopic technique can decipher the identity of the solvent molecules in a ternary mixture with which the solute molecules interact predominantly. Another key problem in understanding the site-specific interactions and dynamics is the presence of "dark states" which are coupled to a normal mode vibration (Fermi resonance). Using time-resolve vibrational spectroscopy at different time delays we show here that structure (vibrational coupling) can be differentiated from interconversion dynamics between different conformations. In a nutshell, this thesis provides a detailed report on the subtle manoeuvres in different spectroscopic techniques using various molecular probes to overcome the ambiguity in our fundamental understanding of the molecular systems.

In this thesis, we have examined the photophysics of the widely used fluorophore in the aqueous solution which has been previously performed in the organic solvents. The combined spectroscopic and theoretical calculation removes the ambiguity in the erroneous conformation-based peak assignment. Our results show that the dual absorption arises not from different conformations but from transitions involving different excited states. We

have employed this photophysical information to recognize the protonated/deprotonated status of the protein-bound fluorophore.

In another work, we have quantified the interaction and dynamics sensed by the thiocyanate vibrational probe in a deep eutectic solvent (DES). In any general application involving DES, water is added to decrease the high inherent viscosity of the DES. The upper limit of hydration in DES and the corresponding structural variation of DES have been previously studied in the absence of any solute. As the solute molecule is an intrinsic part of any "green" application of the DES, understanding the upper hydration limit of DES from the solute's perspective is desirable. Our spectroscopic study exhibits the transition point from the ionic mixture to an aqueous solution of DES (water in DES to DES in water) from the solute's perspective. Our result shows that the transition from the solute's perspective happens at a lower water content that reported in the previous study in the absence of the solute.

The spectroscopic characteristics of the molecular probes changes with the participation of different interactions like hydrogen bonding and electrostatic interaction with the surrounding environment. Furthermore, the peak-assignments get more complicated by the presence of Fermi resonance peaks in the same spectral range. It is imperative to unambiguously assign the transitions to obtain a fundamental understanding of the peaks and their related structural conformations/dynamics. This thesis includes a linear and time-resolved vibrational spectroscopic study of carbonyl probes which show multiple peaks in the protic solvents. In this study, we have used polarization dependent two dimensional IR spectroscopy (2D IR) to assign the peak either to the bright states (hydrogen-bonded population) or dark states (Fermi resonance). In addition, we have studied the hydrogen bond making and breaking dynamics of the carbonyl group in alcohols of varing chain-lengths.

In short, various experimental methods including fluorescence, UV-Vis, IR, and two-dimensional IR (2D IR) spectroscopies in combination with theoretical calculation have been used to investigate the spectroscopic response of fluorescence (warfarin) and vibrational probes including ammonium thiocyanate (NH_4SCN) and ester-based carbonyl probes.

1.5 Outline of thesis

The outline of the thesis is as follows:

In this thesis, we have performed several spectroscopic experiments combined with theoretical calculations to study the characterization and application of molecular probes in various solvents and biological environments. This thesis work will be hepful for biochemists and physical chemists to quantify the interaction and dynamics in a site-specific manner.

Chapter 2 comprises detailed information about the experimental and computational methods used in this thesis.

Chapter 3 includes the photophysical study of warfarin, a fluorophore and potent anticoagulant drug in biology. Herein, experimental measurements and theoretical calculations have been carried out to explore the spectroscopic characteristics of warfarin in an aqueous solution. In the solution phase, warfarin exists in different isomeric forms, and previously, these isomers have been assigned to the origin of the dual absorption of warfarin. In this context, we have performed pH-dependent experiments on warfarin and its structurally constrained derivatives which demonstrate that the coumarin moiety is solely responsible for the dual absorption profile. Using a combination of steady-state and time-resolved spectroscopic experiments, along with quantum chemical calculations, we assign the observed dual absorption to two distinct $\pi \rightarrow \pi^*$ transitions of coumarin moiety of

warfarin. Furthermore, we unambiguously identify the isomeric form of warfarin that binds to human serum albumin in aqueous buffer. This work can further provide the valuable insight about the warfarin and other coumarin-based drug-receptor complexes.

Chapter 4 deals with a widely used deep eutectic solvent (DES) so called reline, which is a mixture of choline chloride (hydrogen bond acceptor) and urea (hydrogen bond donor) in 1:2 molar ratio. Water is commonly used as a cosolvent to reduce the viscosity of the reline. In this study, the disruption of reline's nanostructure around the dissolved solute upon addition of water has been examined by using a polarization-selective two dimensional infrared spectroscopy and molecular dynamics simulations. The ammonium thiocyanate (NH_4SCN) is used as a vibrational probe. Although water molecules are gradually incorporated in the solute's solvation shell even at lower hydration levels, DES is partially able to sustain its heterogeneous nanostructure around the solute up to 41 wt% of added water. This water content indicates the upper hydration limit of the deep eutectic solvent above which the solute senses an aqueous solvation environment. Interestingly, our solute perspective transition point is lower than reported for "water in DES" to "DES in water" transition. Similar to DES, our study will be helpful to modulate the properties of other green solvent media with the appropriate addition of water.

Chapter 5 discussed the origin of various spectral features in the vibrational spectrum of the ester carbonyl group, which is widely used as a vibrational probe for local interaction and dynamics. The ester carbonyl group interacts with various hydrogen bonding partners throughout its application, which modulates its frequency and line shape. The complicated IR spectrum restricts the utility of ester moiety as a site-specific probe that demands a thorough spectral analysis of ester moieties in protic environments. Here, we have performed FTIR and two dimensional IR (2D IR) experiments which indicate the Fermi resonance associated with a ester carbonyls. In addition, we have observed a variation in the

solvent exchange surrounding different esters with a change in the steric effect of alcohols. This work will be helpful to identify the underlying phenomena (Fermi resonance or differential solvation) linked to the vibrational probes in hydrogen bonding environments.

Chapter 6 includes the future scope for all three working chapters (Chapter 3, Chapter 4 and Chapter 5) and the summary of the thesis.

1. 6 References

1. Liu, P.-F.; Avramova, L. V.; Park, C., Revisiting absorbance at 230nm as a protein unfolding probe. *Anal. Biochem.* **2009,** *389*, 165-170.

2. Alupoaei, C. E.; García-Rubio, L. H., Growth behavior of microorganisms using UV-Vis spectroscopy: Escherichia coli. *Biotechnol. Bioeng.* **2004,** *86*, 163-7.

3. Behzadi, S.; Ghasemi, F.; Ghalkhani, M.; Ashkarran, A. A.; Akbari, S. M.; Pakpour, S.; Hormozi-Nezhad, M. R.; Jamshidi, Z.; Mirsadeghi, S.; Dinarvand, R.; Atyabi, F.; Mahmoudi, M., Determination of nanoparticles using UV-Vis spectra. *Nanoscale* **2015,** *7*, 5134-5139.

4. Sedghi, R.; Javadi, H.; Heidari, B.; Rostami, A.; Varma, R. S., Efficient Optical and UV–Vis Chemosensor Based on Chromo Probes–Polymeric Nanocomposite Hybrid for Selective Recognition of Fluoride Ions. *ACS Omega* **2019,** *4*, 16001-16008.

5. Sahoo, H., Fluorescent labeling techniques in biomolecules: a flashback. *RSC Adv.* **2012,** *2*, 7017-7029.

6. Andersen, C. M.; Mortensen, G., Fluorescence Spectroscopy: A Rapid Tool for Analyzing Dairy Products. *J. Agric. Food Chem.* **2008,** *56*, 720-729.

7. Flessau, S.; Wolter, C.; Pöselt, E.; Kröger, E.; Mews, A.; Kipp, T., Fluorescence spectroscopy of individual semiconductor nanoparticles in different ethylene glycols. *Phys. Chem. Chem. Phys.* **2014,** *16*, 10444-10455.

8. Romani, A.; Clementi, C.; Miliani, C.; Favaro, G., Fluorescence Spectroscopy: A Powerful Technique for the Noninvasive Characterization of Artwork. *Acc. Chem. Res* **2010,** *43*, 837-846.

9. Madarasi, P. K.; Sivasankar, C., Infrared spectroscopic detection of ketene formation from carbene and CO sources: an amide synthesis. *New J. Chem.* **2020,** *44*, 8718-8727.

10. Wang, M.; Fu, C.; Liu, X.; Lin, Z.; Yang, N.; Yu, S., Probing the mechanism of plasma protein adsorption on Au and Ag nanoparticles with FT-IR spectroscopy. *Nanoscale* **2015,** *7*, 15191-15196.

11. Vimont, A.; Thibault-Starzyk, F.; Daturi, M., Analysing and understanding the active site by IR spectroscopy. *Chem. Soc. Rev.* **2010,** *39*, 4928-4950.

12. Surewicz, W. K.; Mantsch, H. H.; Chapman, D., Determination of protein secondary structure by Fourier transform infrared spectroscopy: A critical assessment. *Biochemistry* **1993,** *32*, 389-394.

13. Yang, G.; Nanda, J.; Wang, B.; Chen, G.; Hallinan, D. T., Self-Assembly of Large Gold Nanoparticles for Surface-Enhanced Raman Spectroscopy. *ACS Appl. Mater. Interfaces* **2017,** *9*, 13457-13470.

14. Zong, C.; Xu, M.; Xu, L.-J.; Wei, T.; Ma, X.; Zheng, X.-S.; Hu, R.; Ren, B., Surface-Enhanced Raman Spectroscopy for Bioanalysis: Reliability and Challenges. *Chem. Rev.* **2018,** *118*, 4946-4980.

15. Agrawal, G.; Samal, S. K., Raman Spectroscopy for Advanced Polymeric Biomaterials. *ACS Biomater. Sci. Eng.* **2018,** *4* (4), 1285-1299.

16. Chalyavi, F.; Hogle, D. G.; Tucker, M. J., Tyrosine as a Non-perturbing Site-Specific Vibrational Reporter for Protein Dynamics. *J. Phys. Chem. B* **2017,** *121*, 6380-6389.

17. Martin, J. P.; Fetto, N. R.; Tucker, M. J., Comparison of biological chromophores: photophysical properties of cyanophenylalanine derivatives. *Phys. Chem. Chem. Phys.* **2016,** *18*, 20750-20757.

18. Schmitz, A. J.; Hogle, D. G.; Gai, X. S.; Fenlon, E. E.; Brewer, S. H.; Tucker, M. J., Two-Dimensional Infrared Study of Vibrational Coupling between Azide and Nitrile Reporters in a RNA Nucleoside. *J. Phys. Chem. B* **2016,** *120*, 9387-9394.

19. Ma, J.; Pazos, I. M.; Zhang, W.; Culik, R. M.; Gai, F., Site-specific infrared probes of proteins. *Annu Rev Phys Chem* **2015,** *66*, 357-377.

20. Lee, G.; Kossowska, D.; Lim, J.; Kim, S.; Han, H.; Kwak, K.; Cho, M., Cyanamide as an Infrared Reporter: Comparison of Vibrational Properties between Nitriles Bonded to N and C Atoms. *J. Phys. Chem. B* **2018,** *122*, 4035-4044.

21. Carter, K. P.; Young, A. M.; Palmer, A. E., Fluorescent Sensors for Measuring Metal Ions in Living Systems. *Chem. Rev.* **2014,** *114*, 4564-4601.

22. Tutol, J. N.; Peng, W.; Dodani, S. C., Discovery and Characterization of a Naturally Occurring, Turn-On Yellow Fluorescent Protein Sensor for Chloride. *Biochemistry* **2019,** *58*, 31-35.

23. Chen, Z.-j.; Ai, H.-w., A Highly Responsive and Selective Fluorescent Probe for Imaging Physiological Hydrogen Sulfide. *Biochemistry* **2014,** *53*, 5966-5974.

24. Suzuki, Y.; Yokoyama, K., Development of Functional Fluorescent Molecular Probes for the Detection of Biological Substances. *Biosensors* **2015,** *5*, 337-363.

25. Reichardt, C., Solvatochromic Dyes as Solvent Polarity Indicators. *Chem. Rev.* **1994,** *94*, 2319-2358.

26. Fried, S. D.; Bagchi, S.; Boxer, S. G., Measuring electrostatic fields in both hydrogen-bonding and non-hydrogen-bonding environments using carbonyl vibrational probes. *J. Am. Chem. Soc.* **2013,** *135*, 11181-11192.

27. Deb, P.; Haldar, T.; Kashid, S. M.; Banerjee, S.; Chakrabarty, S.; Bagchi, S., Correlating Nitrile IR Frequencies to Local Electrostatics Quantifies Noncovalent Interactions of Peptides and Proteins. *J. Phys. Chem. B* **2016,** *120* (17), 4034-4046.

28. Ye, S.; Zaitseva, E.; Caltabiano, G.; Schertler, G. F.; Sakmar, T. P.; Deupi, X.; Vogel, R., Tracking G-protein-coupled receptor activation using genetically encoded infrared probes. *Nature* **2010,** *464* (7293), 1386-9.

29. Krummel, A. T.; Zanni, M. T., Evidence for Coupling between Nitrile Groups Using DNA Templates: A Promising New Method for Monitoring Structures with Infrared Spectroscopy. *J. Phys. Chem. B* **2008,** *112* (5), 1336-1338.

30. Waegele, M. M.; Culik, R. M.; Gai, F., Site-Specific Spectroscopic Reporters of the Local Electric Field, Hydration, Structure, and Dynamics of Biomolecules. *J. Phys. Chem. Lett.* **2011,** *2* (20), 2598-2609.

31. Ounalli, C.; Essid, M.; Bruno, G.; Abid, S.; Santoro, A.; Aloui, Z., Structural, vibrational, optical properties and theoretical studies of new noncentrosymmetric material: Bis(2-Amino-5-(methylthio)-1,3,4-thiadiazol-3-ium) pentachloroantimonate. *J. Mol. Struct.* **2021,** *1240*, 130538.

32. Ocola, E. J.; Shin, H. W.; Laane, J., Infrared and Raman spectra and theoretical calculations for benzocyclobutane in its electronic ground state. *Spectrochim. Acta A Mol. Biomol. Spectrosc.* **2015,** *136*, 58-63.

33. Plattner, N.; Noé, F., Protein conformational plasticity and complex ligand-binding kinetics explored by atomistic simulations and Markov models. *Nat. Commun.* **2015,** *6*, 7653.

34. Shan, Y.; Kim, E. T.; Eastwood, M. P.; Dror, R. O.; Seeliger, M. A.; Shaw, D. E., How Does a Drug Molecule Find Its Target Binding Site? *J. Am. Chem. Soc.* **2011,** *133* (24), 9181-9183.

35. Bowman, G. R.; Bolin, E. R.; Hart, K. M.; Maguire, B. C.; Marqusee, S., Discovery of multiple hidden allosteric sites by combining Markov state models and experiments. *Proc. Natl. Acad. Sci. U.S.A.* **2015,** *112* (9), 2734-9.

36. Khayer, K.; Haque, T., Density Functional Theory Calculation on the Structural, Electronic, and Optical Properties of Fluorene-Based Azo Compounds. *ACS Omega* **2020,** *5* (9), 4507-4531.

37. Rajapandian, V.; Subramanian, V., Calculations on the Structure and Spectral Properties of Cytochrome c551 Using DFT and ONIOM Methods. *J. Phys. Chem. A* **2011,** *115*, 2866-2876.

38. Bernini, C.; Zani, L.; Calamante, M.; Reginato, G.; Mordini, A.; Taddei, M.; Basosi, R.; Sinicropi, A., Excited State Geometries and Vertical Emission Energies of Solvated Dyes for DSSC: A PCM/TD-DFT Benchmark Study. *J. Chem. Theory Comput.* **2014,** *10*, 3925-3933.

39. Kwac, K.; Lee, C.; Jung, Y.; Han, J.; Kwak, K.; Zheng, J.; Fayer, M. D.; Cho, M., Phenol-benzene complexation dynamics: Quantum chemistry calculation, molecular dynamics simulations, and two dimensional IR spectroscopy. *J. Chem. Phys.* **2006,** *125*, 244508.

40. Kwak, K.; Park, S.; Fayer, M. D., Dynamics around solutes and solute-solvent complexes in mixed solvents. *Proc. Natl. Acad. Sci. U.S.A.* **2007,** *104* (36), 14221-6.

41. Zhang, J.; Wang, L.; Zhang, J.; Zhu, J.; Pan, X.; Cui, Z.; Wang, J.; Fang, W.; Li, Y., Identifying and Modulating Accidental Fermi Resonance: 2D IR and DFT Study of 4-Azido-l-phenylalanine. *J. Phys. Chem. B* **2018,** *122*, 8122-8133.

42. Park, J. Y.; Mondal, S.; Kwon, H.-J.; Sahu, P. K.; Han, H.; Kwak, K.; Cho, M., Effect of isotope substitution on the Fermi resonance and vibrational lifetime of unnatural amino acids modified with IR probe: A 2D-IR and pump-probe study of 4-azido-L-phenyl alanine. *J. Chem. Phys.* **2020,** *153*, 164309.

Chapter 2

Experimental and Computational Methods

2.1 UV-Visible Absorption Spectroscopy

All the steady-state absorption spectrum were recorded on a Shimadzu UV 3600 Plus spectrophotometer using a quartz cuvette of 1 cm optical path length. A tungsten lamp has been used as a source for visible light and a deuterium lamp is utilized for the UV region. To avoid the possibility of aggregation or re-absorption effects, very dilute solutions having OD < 0.1 at their excitation wavelength are used for the absorption measurements. A schematic diagram of the UV-vis spectrophotometer has been shown in Figure 2.1. The light obtained from the corresponding sources illuminates onto the monochromator, which dispersed it into different wavelengths. This dispersed light falls onto the beam splitter which split it into two beams. One beam remains undeflected and interact with the sample solution while the second beam gets reflected by 90^0 and passes through the reference solution. The UV-vis signal generated by the differential absorption from the reference and the sample solution is represented as absorption versus wavelength plot.

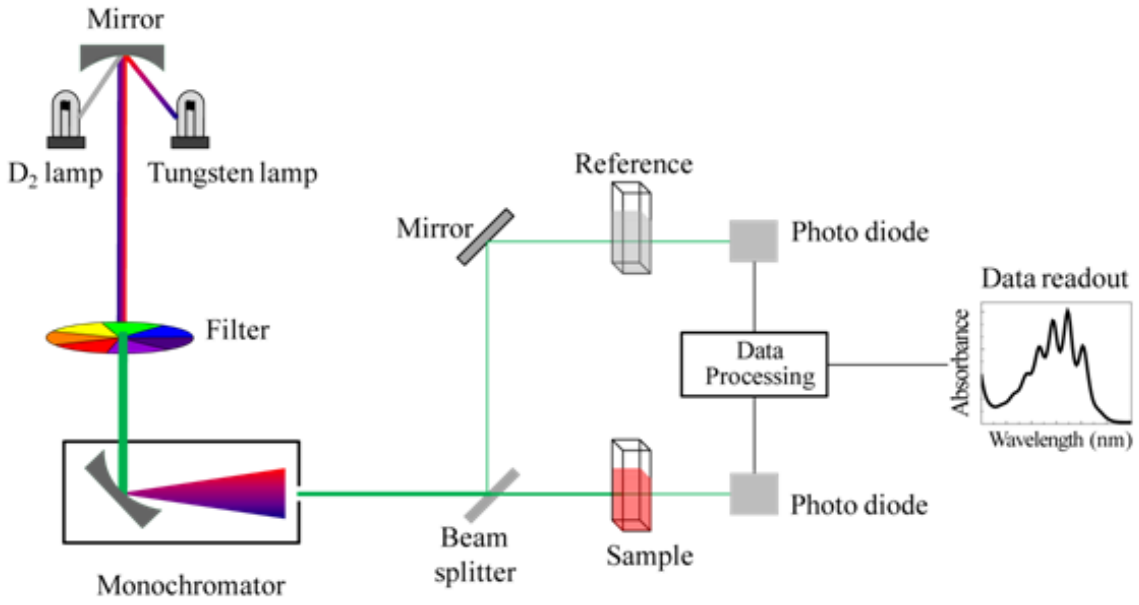

Figure 2.1 Schematic diagram of UV-Visible absorption spectrophotometer.

2.2 Steady-State Fluorescence Spectral Measurement

The steady-state fluorescence spectra were measured on a PTI Quanta Master steady-state spectrofluorometer using quartz cell of 1 cm path length. A schematic diagram of the spectrofluorometer is shown in Figure 2.2

2.2.1 Light sources

In the spectrofluorometer, gas discharge lamps like xenon lamps and high-pressure mercury lamps are commonly utilized. In addition to that, some other lamps like incandescent lamps (tungsten lamp), laser (tunable dye laser), etc are also used.

2.2.2 Gratings

In most of the spectrofluorometers, diffraction gratings are used rather than prisms. The performance specifications of a monochromator include dispersion, efficiency, and stray light levels. Dispersion is usually given in nm/mm. The slit width is expressed in nm/mm. A monochromator for fluorescence spectroscopy should have low stray light levels to avoid scattered or stray light problems.

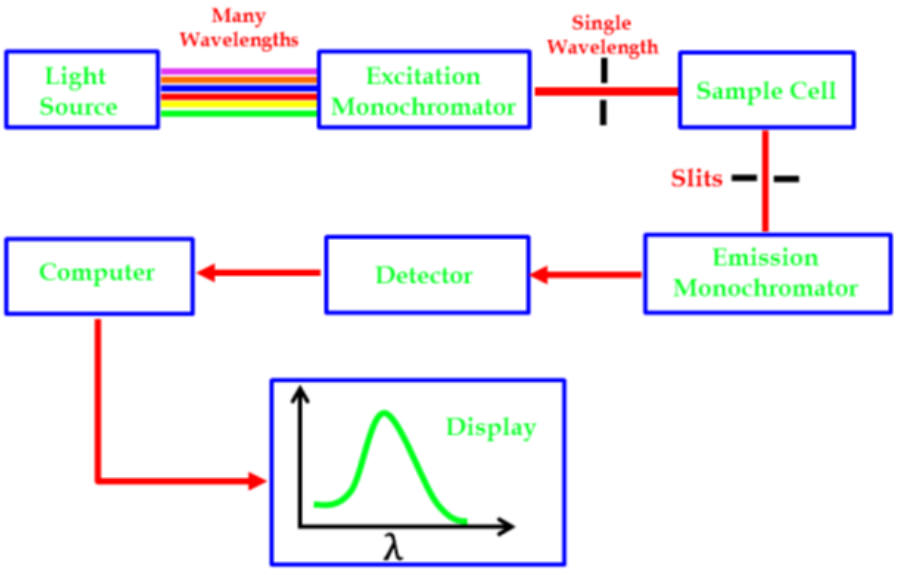

Figure 2.2 Block diagram of a spectrofluorometer.

2.3 Time-Correlated Single Photon Counting (Picosecond) measurement

The lifetime was recorded using a DeltaFlex time-correlated single-photon counting (TCSPC) spectrometer using 310 nm excitation light with a full width at half-maximum (fwhm) of the instrument response function ~50 ps. The excitation light was obtained from a tunable Mai-Tai Laser with a repetition rate of 80 MHz which was scaled down to 1/10th, i.e. 8 MHz, with a pulse picker. A hybrid photomultiplier (HPPD) was used as a detector in the above setup. The decays were collected at magic angle polarization with respect to vertically polarized excitation light to eliminate the effects of rotational anisotropy.

2.4 Fourier Transform Infrared Spectroscopy (FTIR)

The inherent properties of the FTIR spectrometer make it superior compared to the conventional dispersive infrared spectrometer. A schematic diagram of a Fourier transform infrared spectrophotometer (FTIR) is shown in Figure 2.3. Instead of monochromator grating, the light generated from an infrared source are controlled using an interferometer. The IR beam is directed to a beam splitter in the interferometer, which splits it into two beams, one undeflected and the other reflected at a 90° angle. The reflected beam falls onto the fixed mirror and reflects back to the beam splitter. The undeflected beam goes to the moving mirror and also comes back to the beam splitter. The movement of the moving mirror changes the path length of the beam shined onto it. The beams reflected from both the mirrors meet and recombine at the beam splitter, but the path lengths of these two beams are different, which create both constructive and destructive interferences. The combined beam containing these interference patterns, also called an interferogram, is finally focused on the sample. After it passes through the sample, the sample absorbs specific wavelengths or frequencies. The radiation transmitted from the sample contains a time-domain interferogram signal that finally reaches the detector and provides information about the

amount of energy absorbed at every wavelength. The Fourier transformation formalism is used to convert the interferogram from time-domain to frequency-domain signal. The FTIR spectroscopy has the following advantages 1) The interferometer geometry scan all frequencies simultaneously and reduces the data acquisition time drastically. 2) It provides other benefits such as good signal to noise ratio and higher resolution. The IR absorption spectra reported in this thesis were recorded on a FTIR-Brucker Vertex 70 spectrometer with 2 cm^{-1} resolution at room temperature. For each sample, ~90 µL of the sample solution was loaded into a demountable cell consisting of two windows (CaF_2, 3 mm thickness, Shenzen Laser Co. Ltd.), separated by a mylar spacer of 56 µm thickness.

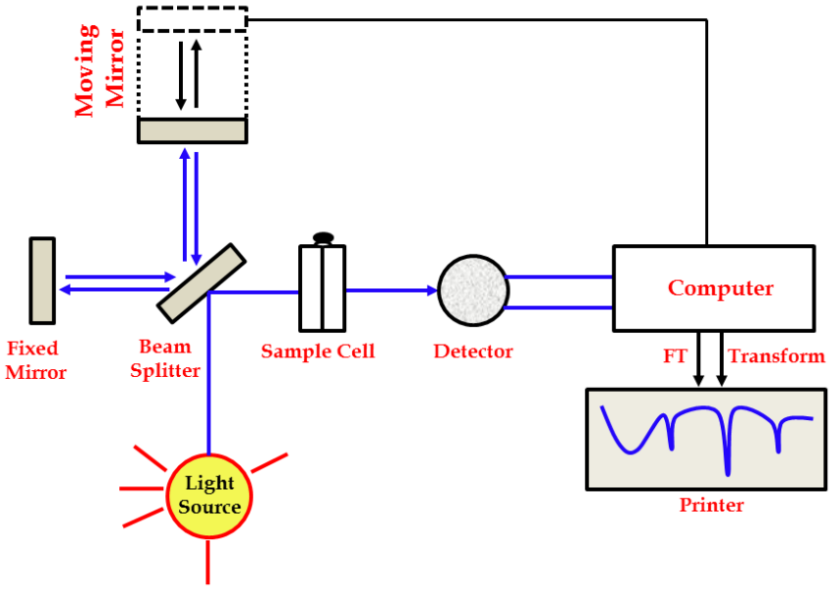

Figure 2.3 Schematic diagram of Fourier transform infrared (FTIR) spectrophotometer

2.5 Two-dimensional Infrared Spectroscopy (2D IR) spectroscopy

Recently, two dimensional infrared (2D IR) spectroscopy has been used as an experimental tool to investigate ultrafast fluctuations, structural evolution and interchanging dynamics in solution phase. The additional dimension in 2D IR spectroscopy helps to explore the vibrational transitions that are hidden in FTIR spectroscopy. The 2D IR technique is an ultrafast IR analog of 2D NMR and is a very sensitive tool to determine the structure and dynamics in the condensed phase. Despite its wide application, 2D NMR spectroscopy is limited to measure the dynamics occurs at a timescale in the range of ms to μs. In contrast, 2D IR spectroscopy quantifies the dynamics at sub-picosecond timescale.

2.5.1 2D IR Experimental setup, pulse sequence

2D IR spectroscopy is a third-order non-linear spectroscopic method, where three successive femtosecond IR pulses interact with a sample that generates the vibrational echo pulse. 2D IR experiments described in this thesis are performed on the pulse shaper based spectrometer (Phasetech). The schematic representation of the 2D IR experimental setup is presented in Figure 2.4. Ti:Sapphire regenerative amplifier generates ultrashort pulses of femtosecond timescale at peak maxima 800 nm with a repetition rate of 1 KHz which are used to pumped the optical parametric amplifier (OPA). The signal and idler beams of OPA, combined using difference frequency generation (DFG) in a $AgGaS_2$ crystal, produces IR pulses of ~ 50 fs duration. These IR pulses are further directed to the pump-probe geometry based spectrometer, where it is split into a strong pump pulse and a weak probe pulse. The pump pulse is then passed through the acousto-optics modulator (AOM). AOM makes two temporally separated pump pulses using the pulse shaping method which modulates the phase and amplitude of the pulses. The pump pulse further passes through a waveplate and a polariser which allows us to perform a polarisation selective 2D IR experiment.

Furthermore, the pump pulses enter into a motorised delay stage that modulates the time delay between the pump and probe pulses used to acquire the 2D IR spectrum. The pump and probe pulses were spatially and temporarily overlapped and focused at the sample using parabolic mirrors. The pulses span sufficient bandwidth to excite the v = 0 - 1 and v = 1 - 2 transitions simultaneously. The interaction of both pump and probe pulses with the sample generates the vibrational echo signal in phase to the probe pulse. Furthermore, the signal dispersed on a monochromator (Princeton instruments) and detected by a liquid nitrogen cooled MCT IR array detector (Infrared Associates).

Polarisation selective pump-probe experiment (PSPP) and 2D IR experiments were performed in the $\langle XXXX \rangle$ and $\langle XXYY \rangle$ polarization conditions, where the polarization of the pump beam was either parallel or perpendicular with respect to that of the probe beam. Pump polarization before the sample was controlled using the combination of a quarter-wave plate and a polarizer, as discussed above. The polarization dependent pump-probe data were analysed to obtain the isotropic population decay.

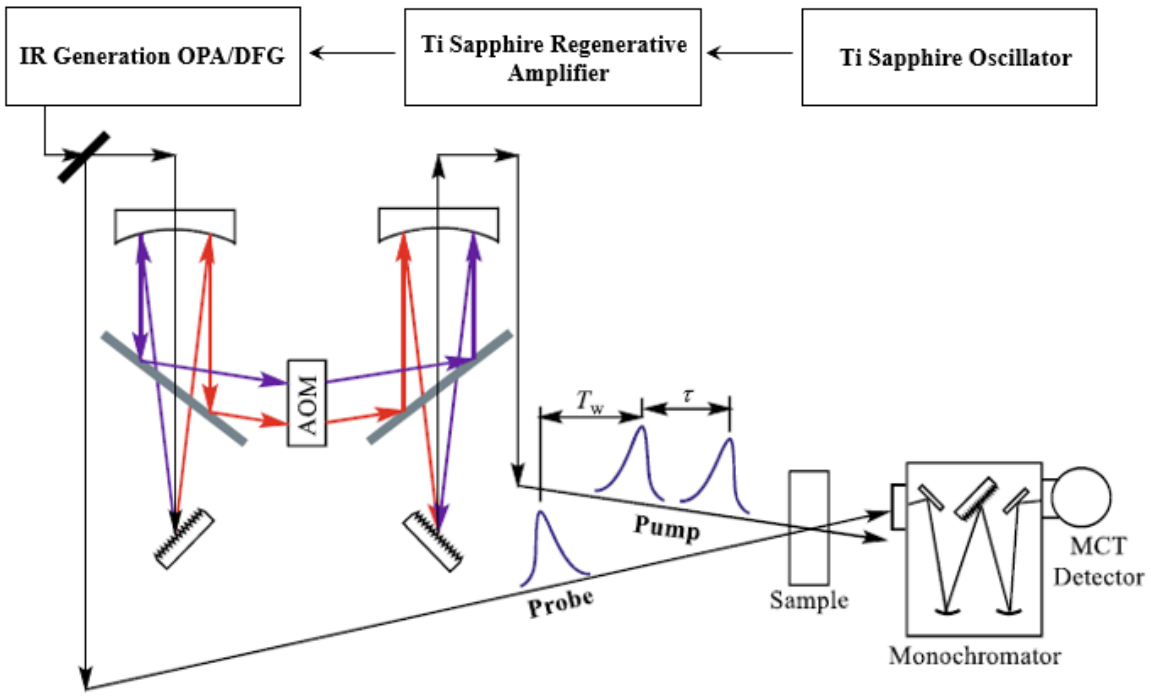

Figure 2.4 Experimental setup for the pulse shaper based 2D IR spectroscopy.

The 2D IR experiment is mainly based on the three time periods between three successive femtosecond pulses shown in Figure 2.5. The first pulse interacts with the vibrational oscillator and creates a quantum coherence state between vibrational ground (v = 0) and excited (v = 1) states. The second pulse in the sequence confines this coherence to one of the two vibrational states. The time interval between pulse 1 and 2 is called a coherence time (τ) and between pulse 2 and 3 is called a population period or waiting time (T_w). After waiting time (T_w), the third pulse create another coherence between v = 0 to v = 1 and v = 1 to v = 2 vibrational states at which all molecules are oscillating in phase. The controlled modulation of the time intervals between pulse 1 - 2 (τ) and pulse 2 - 3 (T_w) and the emitted vibrational echo frequency (ω_t) provides the experimental data for 2D IR spectroscopy. The data are represented as a two-dimensional correlation map of the excitation frequency (ω_τ) versus detection frequency (ω_t), which describes the vibrational transitions that occur during the coherence and detection period.

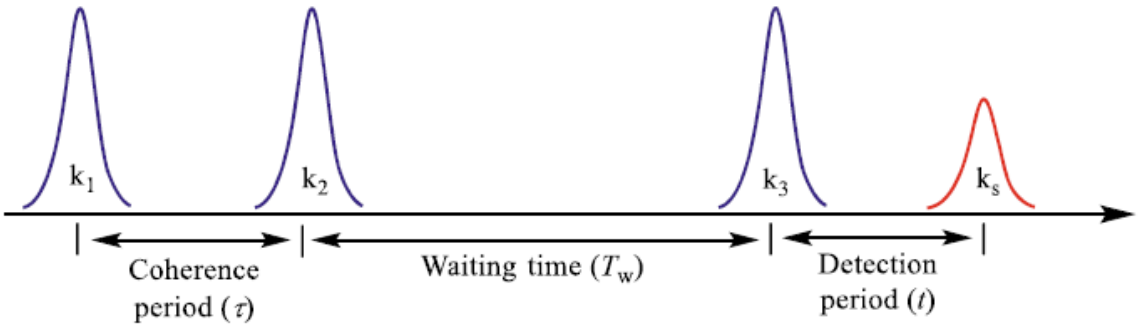

Figure 2.5 Pulse sequence used in the 2D IR experiment.

2.5.2 Spectral signatures of different ultrafast processes in 2D IR spectrum

2D IR experiment involves the interaction of the three femtosecond IR pulses with the sample which emits the vibrational echo signal in the following order: The first pulse excites the sample and each molecule is labeled with the initial frequency ω_τ. The second pulse stops the coherence and starts the population period T_w, during which the labeled molecules experience ultrafast fluctuation or chemical exchange dynamics. The interactions of the third pulse end population period and start second coherence period (detection time), which ends with the emission of vibrational echo signal composed of final frequency ω_t of the labeled molecules. The 2D IR spectrum is a correlation of initial and final frequency represented as a contour plot.

The typical 2D IR spectrum consists of two peaks, one peak present on the diagonal corresponds to v = 0 - 1 transition (blue peak) and another off-diagonal peak corresponds to v = 1 - 2 transition (red peak) occurs at lower frequency along the ω_t axis due to the vibrational anharmonicity (Figure 2.6a and b). The diagonal (v = 0 - 1) peak arises from ground state bleaching and stimulated emission, while off-diagonal (v = 1 - 2) peak coming from excited state absorption. The difference between the center frequency of the diagonal (blue) and off-diagonal (red) peak gives the vibrational anharmonicity of the system.

2.5.3 Spectral diffusion

The line shape of the 2D IR peaks is mainly affected by the undergoing processes such as ultrafast structural fluctuation and conformational dynamics which provides the information about the range of frequency sampled during the given waiting time T_w. At T_w = 0, the similarity between the initial and the final frequency shows a peak elongated along the diagonal in 2D IR spectrum as shown in Figure 2.6b. However, with increase in T_w, the peak shape becomes more symmetrical, essentially circular, when each molecule has sampled all possible conformations (Figure 2.6c). The structural fluctuation causes diffusion of spectral lines throughout the spectrum over time and this process is known as spectral diffusion.

2.5.4 Chemical exchange

The chemical exchange dynamics is observed by the evolution of the off-diagonal cross peaks as a function of T_w. In chemical exchange process, the population associated with one chemical species may be transferred to another chemical species during the population period. As shown in Figure 2.6 (d), at very short T_w, ~ 0 ps, when the two species are unable to interchange, only two peaks occurs along the diagonal coming from v = 0 – 1 transitions of the two different chemical species. With the increase in the population period, two chemical species interchanging between one another under thermal equilibrium causes the growth of two off-diagonal cross peaks in 2D IR spectrum. Similar to the v = 0 - 1 transitions, v = 1 - 2 transitions also shows the growth of cross peaks arising due to the chemical exchange process (for simplicity, not shown in the Figure 2.6d).

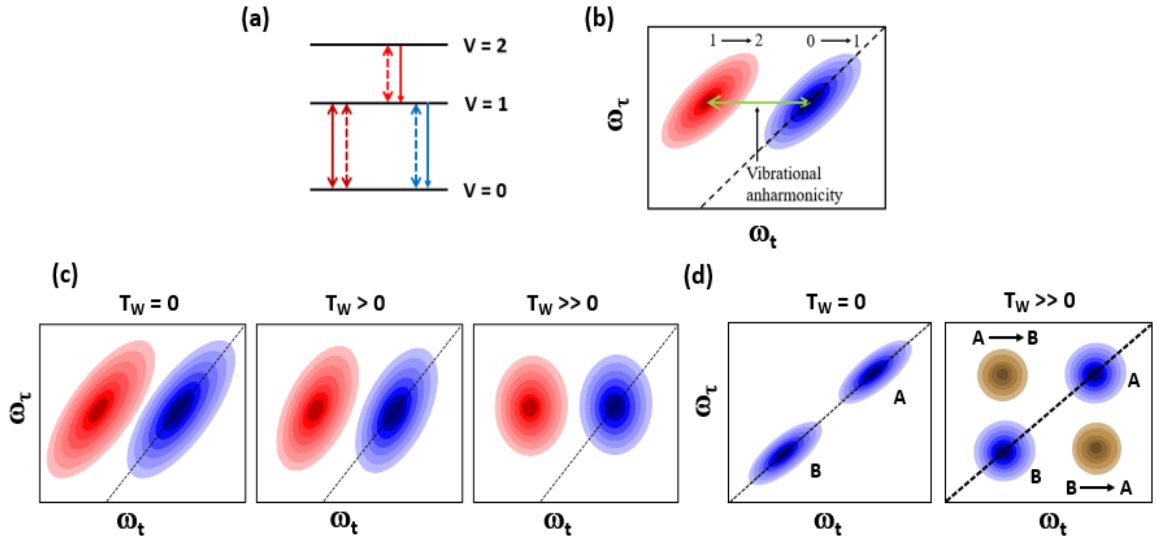

Figure 2.6 (a) Vibrational energy levels involved in the 2D IR spectra. (b) A typical 2D IR spectrum also shown along with the vibrational anharmonicity. (c) A representation of the process of spectral diffusion as a function of T_w. (d) A representation of chemical exchange using 2D IR spectra. Exchange has been shown only between 0 →1 transitions.

2.5.5 Analysis of 2D IR spectrum

2D IR correlation spectrum consists of the peaks with different positions, signs, amplitudes and line shapes as characteristics of the vibrational eigenstates of the vibrational system and their interactions with the surrounding environments. The variation in the spectral line shapes in 2D IR experiments are sensitive to the ultrafast structural fluctuations of molecules, peptides, and proteins in the solution phase. The frequency-frequency correlation function (FFCF) is used to quantitatively determine the amplitude and timescale of the frequency fluctuation as a function of T_w. Several methods have been developed to extract the FFCF directly from T_w dependent 2D IR spectrum. The global fitting of the 2D IR spectra at the different waiting times by varying the set of parameters was the first approach to get the FFCF from 2D IR spectrum. Asbury et.al. suggested the dynamical line width to correlate FFCF, which is a line width for the fixed value of ω_t.[1] Also, some of the research

groups defined FFCF by the ratio of the sum and difference of the spectral width along the diagonal and antidiagonal axis (i.e. the ellipticity of the 2D IR line shape).[2] However, the analysis of the 2D IR spectrums become more challenging when diagonal and off-diagonal peaks overlap due to the smaller anharmonicity. To overcome this problem, Michael Fayer (Stanford University) suggested a center line slope (CLS) method[3] to determine the FFCF. The center line slope method involves the line constructed by joining the maximum intense point obtained by plotting the lines along the ω_τ axis and parallel to ω_t axis, FFCF is defined as the inverse of the center line slope. The main advantages of CLS method over all other methods are insensitivity to the pulse duration, sloping absorptive background, and overlap between diagonal and off-diagonal peaks.

In this thesis, T_w-dependent evolution of the 2D IR spectral line shape was modeled with center line slope (CLS) method.[7] Evolution of CLS with increasing time delay was fitted with a bi-exponential function,

$$C(t) = a_1 e^{\left(\frac{t}{\tau_1}\right)} + a_2 e^{\left(\frac{t}{\tau_2}\right)}$$

The sum of the amplitudes ($a_1 + a_2$) provides the initial values of the CLS decay at 200 fs. This initial value is a measure of the heterogeneity around the solute. The larger the initial value, the larger is the heterogeneity.

2.6 Quantum calculations

2.6.1 TDDFT and EOM-CCSD calculations

Geometries of 4-hydroxycoumarin, 4-methoxycoumarin, and different isomeric forms of warfarin were optimized using density functional theory (DFT) with the hybrid functional B3LYP[4-5] and the 6-31+G(d,p) basis set. The SMD solvation model is used as a solvent continuum during geometry optimization.[6] The calculation of transition energies and oscillator strengths of the higher singlet excited states were performed using time-dependent density functional theory (TDDFT) with the same functional and basis set. Molecular orbital diagrams of all possible forms of every compound were computed at the Hartree−Fock (HF) level of theory with the 6-31+G(d,p) basis set. The equation-of-motion coupled-cluster singles and doubles (EOM-CCSD) method, with the same 6-31+G(d,p) basis set was used to calculate accurate oscillator strengths of isolated 4-methoxycoumarin. The DFT, TDDFT, and HF calculations were performed using the Gaussian 09 program,[7] and the EOM-CCSD calculations were carried out using Molpro 2012.[8-9]

2.7 Molecular dynamics simulations

All atom classical molecular dynamics simulation of reline water system was performed using the GROMACS 2016.5 package.[10] Force field parameters for reline were taken from the well-benchmarked work of Doherty et. al.[11] Thiocyanate and ammonium ions were modelled with GAFF force field and TIP3P model was used for water.[12] To check the validity of the water model, bulk density of the reline water mixtures were computed and compared with the experimental values.[13] The reline simulation box was made of a thiocyanate ion solvated in 1:2 molar ratio of choline chloride and urea. The volume of the cubic box was monitored to mimic the experimental thiocyanate concentration of ~0.1M. The reline water mixtures, namely 3W, 5W, 10W and 15W were made by inserting

additional water according to the corresponding water mole fraction. LINCS algorithm was used to constrain all covalently attached hydrogen bonds. Periodic boundary condition was used with short range electrostatic cut-off of 16 Å. Before the equilibrium step, steepest decent energy minimisation with 2 fs step size was performed. The system was equilibrated with velocity rescale thermostat at 300K for 1 ns and subsequently with Parrinello-Rahman barostat at 300K, 1 bar for 5 ns. Production runs were carried out for additional 100 ns. Hydrogen-bonding analysis was performed with GROMACS in-built tool with an angle cut-off of 30º and a distance cut-off of 3.5 Å. TRAVIS has been used to calculate three-dimensional SDF plot.[14]

2.8 References

1. Asbury, J. B.; Steinel, T.; Kwak, K.; Corcelli, S. A.; Lawrence, C. P.; Skinner, J. L.; Fayer, M. D., Dynamics of water probed with vibrational echo correlation spectroscopy. *J. Chem. Phys.* **2004,** *121*, 12431-12446.

2. Lazonder, K.; Pshenichnikov, M. S.; Wiersma, D. A., Easy interpretation of optical two-dimensional correlation spectra. *Opt. Lett.* **2006,** *31* (22), 3354-3356.

3. Kwak, K.; Park, S.; Finkelstein, I. J.; Fayer, M. D., Frequency-frequency correlation functions and apodization in two-dimensional infrared vibrational echo spectroscopy: A new approach. *J. Chem. Phys.* **2007,** *127*, 124503.

4. Lee, C.; Yang, W.; Parr, R. G., Development of the Colle-Salvetti correlation-energy formula into a functional of the electron density. *Phys. Rev. B* **1988,** *37*, 785-789.

5. Becke, A. D., Density-functional thermochemistry. III. The role of exact exchange. *J. Chem. Phys.* **1993,** *98*, 5648.

6. Marenich, A. V.; Cramer, C. J.; Truhlar, D. G., Universal Solvation Model Based on Solute Electron Density and on a Continuum Model of the Solvent Defined by the Bulk Dielectric Constant and Atomic Surface Tensions. *J. Phys. Chem. B* **2009,** *113*, 6378-6396.

7. Frisch, M. J.; Trucks, G. W.; Schlegel, H. B.; Scuseria, G. E.; Robb, M. A.; Cheeseman, J. R.; Scalmani, G.; Barone, V.; Mennucci, B.; Petersson, G. A.; et al., Gaussian 09,A.01, Wallingford CT. **2009**.

8. Werner, H.; Knowles, P.; Knizia, G.; Manby, F.; Schütz, M.; Celani, P.; Korona, T.; Lindh, R.; Mitrushenkov, A.; Rauhut, G., Molpro. *version 2010.1, a package of ab initio programs* **2010**.

9. Werner, H.-J.; Knowles, P. J.; Knizia, G.; Manby, F. R.; Schütz, M., Molpro: a general-purpose quantum chemistry program package. *WIREs Comput. Mol. Sci.* **2012,** *2*, 242-253.

10. Abraham, M.; Murtola, T.; Schulz, R.; Páll, S.; Smith, J.; Hess, B.; Lindahl, E., GROMACS: High performance molecular simulations through multi-level parallelism from laptops to supercomputers. *SoftwareX* **2015,** *1*, 19-25.

11. Doherty, B.; Acevedo, O., OPLS Force Field for Choline Chloride-Based Deep Eutectic Solvents. *J. Phys. Chem. B* **2018,** *122*, 9982-9993.

12. Wang, J.; Wolf, R. M.; Caldwell, J. W.; Kollman, P. A.; Case, D. A., Development and testing of a general amber force field. *J. Comput. Chem.* **2004,** *25*, 1157-74.

13. Yadav, A.; Pandey, S., Densities and Viscosities of (Choline Chloride + Urea) Deep Eutectic Solvent and Its Aqueous Mixtures in the Temperature Range 293.15 K to 363.15 K. *J. Chem. Eng. Data* **2014,** *59*, 2221-2229.

14. Brehm, M.; Kirchner, B., TRAVIS - A Free Analyzer and Visualizer for Monte Carlo and Molecular Dynamics Trajectories. *J. Chem. Inf. Model.* **2011,** *51*, 2007-2023.

Chapter 3

The Curious Case of Aqueous Warfarin: Structural Isomers or Distinct Excited States?

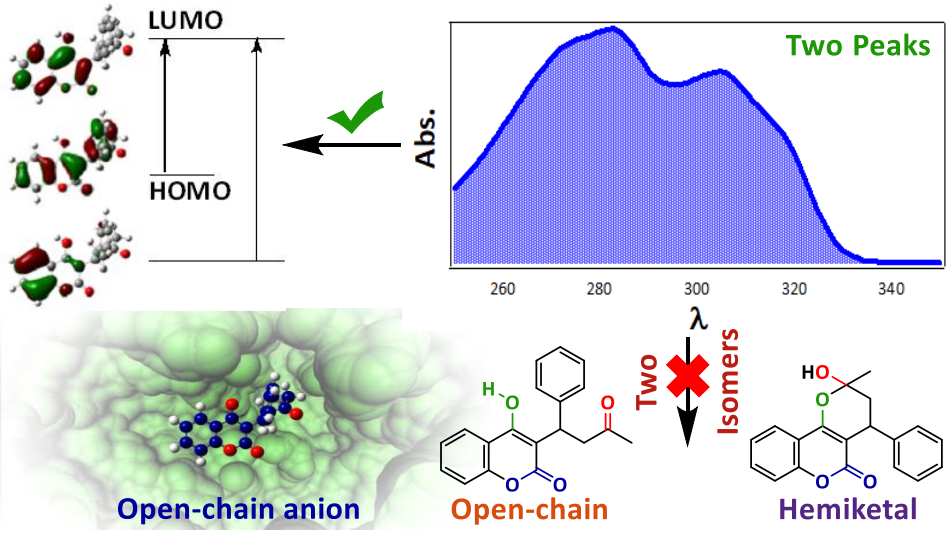

3.1 Introduction

Coumarin derivatives have drawn significant interest in chemistry and biology, due to their pharmaceutical importance as well as their fluorescent properties. Warfarin, a coumarin derivative of clinical significance, is a highly potent anticoagulant drug that reduces the risk of strokes and heart attacks by preventing blood clots in veins.[1-3] Moreover, warfarin binds to human serum albumin (HSA),[4] the most abundant protein in blood plasma which transports hormones, fatty acids, bilirubin, and drugs in the human body.[5-6] The high affinity and selectivity of warfarin towards HSA and the extensive increase in its fluorescence upon binding to the protein makes warfarin a prototype fluorescent probe in biology.[7] Fluorescence lifetimes of warfarin in aqueous solution, free or bound to blood plasma proteins, have been correlated to blood coagulation.[8] Interestingly, warfarin is known to exist in various isomeric forms.[9-12] The conjugation between the functional groups gives rise to the coumarin and the chromone structures in various solvents (Figure 3.1).[13-14] Furthermore, the proximity of the hydroxyl and the carbonyl moieties allows open-chain and cyclic hemiketal conformations, leading to four possible isomers of warfarin. In addition, the deprotonated forms (anion) are also involved in the structural diversity of warfarin in water. Therefore, the structural determination of warfarin in water is imperative from the perspective of biological applications.[15]

Surprisingly, the current structural assignment in aqueous solution is directly implemented from the indirect spectroscopic evidences of warfarin in non-aqueous solvents. Nuclear magnetic resonance (NMR) studies in different organic solvents have indicated the predominance of the coumarin structural form over the chromone.[14, 16-17] The coexistence of hemiketal and open-chain isomeric forms has also been suggested from NMR peak positions.[16-18] However, due to the low solubility of warfarin in water, the NMR based structural information of warfarin in aqueous medium is currently unavailable.

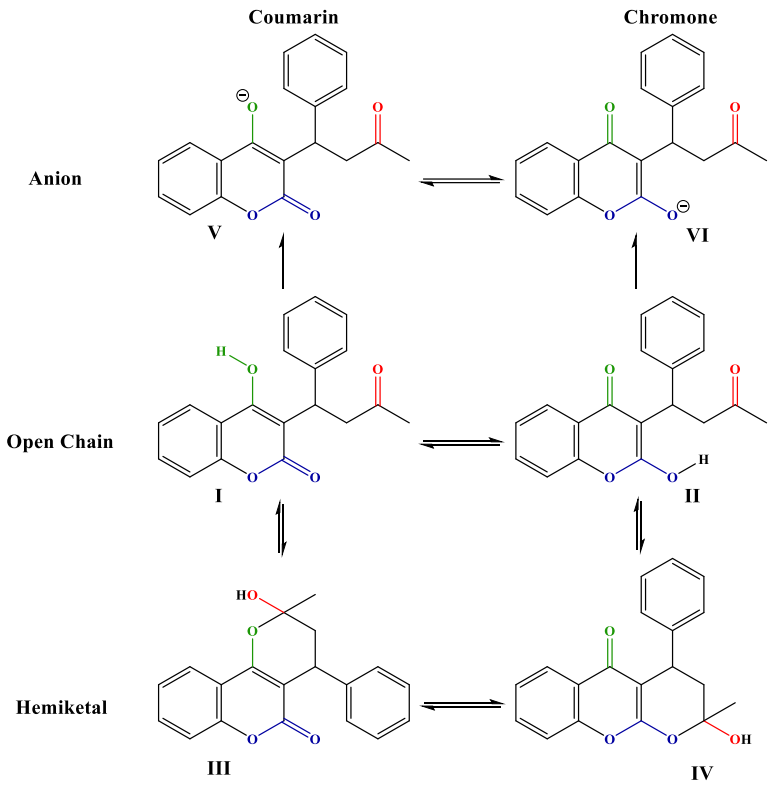

Figure 3.1 Possible isomers of warfarin: (I) coumarin open-chain, (II) chromone open-chain, (III) coumarin hemiketal, (IV) chromone hemiketal, (V) coumarin anionic, and (VI) chromone anionic. The hydroxyl, ketone, and ester functional groups are shown in green, red, and blue, respectively.

Recently, in lieu of NMR, the absorption spectroscopy of warfarin in organic solvents and in solvent mixtures has been used to identify the warfarin isomers. The absorption spectrum of warfarin consists of two overlapping peaks in the 250-350 nm range, which have been assigned to the hemiketal (~280 nm) and the open chain isomers (~310 nm).[19] Although the absorption experiments were not performed in an aqueous solution, several structural studies on ring-chain isomerism as well as various biological applications of warfarin have used these absorption-spectrum based structural interpretations.[10-11, 20-27] The ambiguity in these interpretations increases with another recent report suggesting that these two absorption peaks of warfarin arise not from the different isomeric forms, but from $n \rightarrow \pi^*$ and $\pi \rightarrow \pi^*$ transitions.[26] The biological significance of warfarin and the

existence of several coumarin containing drug molecules demand an unambiguous structural assignment in aqueous medium.

In this report, we investigate the origin of the dual absorption of warfarin in aqueous solution using a combination of time-averaged and time-resolved spectroscopic experiments and quantum mechanical calculations. Absorption and emission spectroscopic measurements on warfarin in aqueous solutions at different pH values are performed. In addition, experiments are performed on structurally constraints derivatives of warfarin which are proficient at forming only a single isomeric form of warfarin. Interestingly, we observe a similar dual absorption pattern for both the structurally constrained warfarin derivatives, irrespective of being restricted to one particular isomer. These results demonstrate that the lower and the higher wavelength transitions in the absorption spectrum of warfarin do not arise from two different structural isomers. Furthermore, steady state emission spectroscopy also shows similar results. Our results show that the ring-chain isomerism of molecules structurally related to warfarin cannot be explained using the relative populations of the two absorption bands, as they have been done in the past. Further, our results demonstrate that the dual absorption is due to two distinct $\pi \rightarrow \pi^*$ transitions of warfarin. Quantum chemical calculations indicate that the dual absorption band arises due to distinct transitions to accessible excited states. The transitions occur from two energetically close occupied molecular orbitals (MO) to the lowest unoccupied molecular orbital (LUMO) associated with the coumarin moiety of warfarin. Time-resolved emission spectroscopy on coumarin derivatives confirms that warfarin exists in its anionic form in water at pH greater than 6.0. Further, experiments are performed in the presence of HSA to identify the isomer of warfarin that binds to the blood plasma protein in aqueous buffer. Our results reveal that warfarin adopts an open-chain anionic form when bound to HSA, independent of the pH of the aqueous buffer.

3.2 Materials and sample preparation

Warfarin (analytical standard), 4-hydroxycoumarin (98%), pyranocoumarin (analytical standard) and HSA were purchased from Sigma-Aldrich and their purity was checked using the HPLC-MS technique. Methoxywarfarin and 4-methoxycoumarin were synthesized using the standard methylation method and the purity of the synthesized compounds was checked by NMR spectroscopy and HPLC-MS technique.[28] All solvents were of spectroscopy grade (Sigma-Aldrich). Each compound was dissolved independently in aprotic solvents and aqueous buffer such that the final concentration of the liquid sample is 60 μM for the absorption and emission experiments.

3.3 Results and discussion

The ground state structures of different isomeric forms of warfarin in water are optimized using DFT (Table 3.1). We consider every possible structural conformer of warfarin to remove any bias reported in previous studies. The open-chain and the cyclic hemiketal coumarin structures (I and III) are found to be more stable than the corresponding chromone structures (II and IV). Nevertheless, in case of any equilibrium between structure I and III, the equilibrium is expected to shift towards the lower energy hemiketal structure. The calculated $S_0 \rightarrow S_1$ transition wavelengths and corresponding oscillator strengths further suggest that the chromone isomers are not only energetically unfavorable, but also would not contribute to the absorption spectrum of warfarin. Due to the strong conjugation between hydroxyl oxygen and ester carbonyl of the anionic form of warfarin, both isomers V and VI show the same geometry in the DFT calculation (Figure 3.2). Only one resonance structure also supports the presence of single species of the deprotonated form of warfarin in solution at higher pH.

Table 3.1 Calculated spectral parameters for $S_0 \rightarrow S_1$ electronic transitions of various forms of warfarin in water (SMD solvation model) using DFT and TDDFT B3LYP/6-31+G(d,p)

Structure	**Open-chain**		**Hemiketal**		**Anion**
	I	**II**	**III**	**IV**	**(V/VI)**
Relative ground state energy (kcal/mol)	3.6	10.6	0.0	8.0	288.4
Absorption λ_{max}(nm)	316.7	309.7	303.1	309.7	319.3
Oscillator strength (f)	0.56	0.03	0.66	0.04	0.44

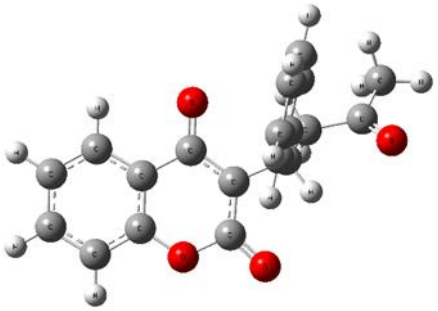

Figure 3.2 The single resonance structure of deprotonated form of warfarin (structures V and VI) obtained during the geometry optimization using DFT B3LYP/6-31+G(d,p) calculation.

In previous studies, the dual absorption of warfarin in non-aqueous solvent and aqueous solution at different pH has been assigned to the various isomeric forms of warfarin (Figure 3.3a).[19, 27] Similarly, absorption spectra of warfarin in aqueous solution exhibit two distinct absorption peaks centered at ~280 nm and ~310 nm at lower pH (Figure 3.3b). An increase in the pH results in a decrease in the absorbance of the ~280 nm peak with a simultaneous increase in the absorbance of the ~310 nm peak. Moreover, a small red-shift is observed in the peak at ~310 nm for pH values greater than 5. Based on previous structural assignments (Figure 3.3a), the origin of the dual absorption profile can be speculated to arise from the open-chain (~310 nm) and the hemiketal isomers (~280 nm). Although this speculation may

appear qualitatively consistent with our calculated wavelengths, confounding results are obtained when control experiments are performed on structurally constrained warfarin derivatives.

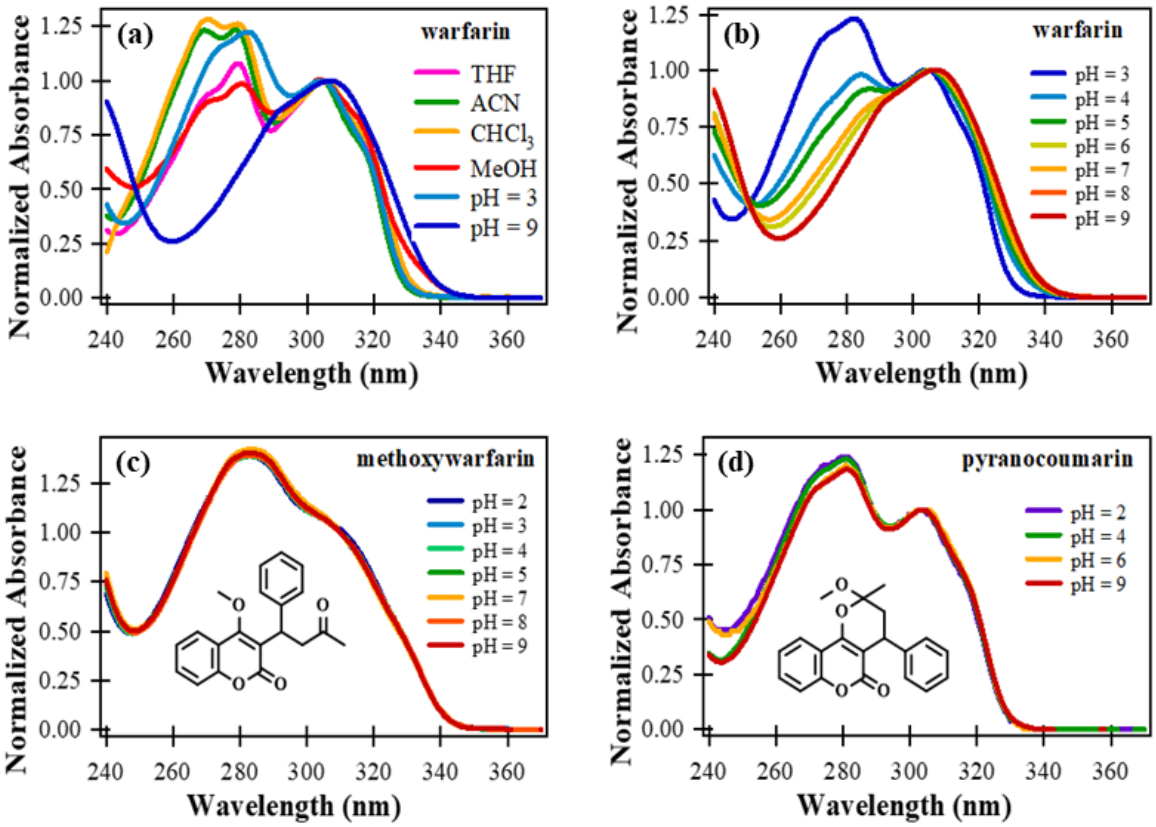

Figure 3.3 (a) Normalized (at 310 nm) absorption spectra of warfarin in different non-aqueous solvents and aqueous solutions of acidic (pH = 3) and basic (pH = 9) pH. Similar spectra in non-aqueous solvents have been previously used as the basis of structural assignment of warfarin. Normalized (at 310 nm) absorption spectra of (b) warfarin, (c) methoxywarfarin and (d) pyranocoumarin in aqueous solution of different pH. The structures of methoxywarfarin and pyranocoumarin are shown along with the spectra.

Two structurally constrained warfarin derivatives, methoxywarfarin and pyranocoumarin (structures in Figure 3.3c-d) are selected, which, by virtue of their structures, are restricted to exclusively open-chain and hemiketal conformers, respectively. Surprisingly, similar to warfarin, both methoxywarfarin and pyranocoumarin have dual absorptions at ~280 nm and

~310 nm (Figure 3.3c-d) irrespective of their confinement to one specific isomeric form. However, unlike warfarin, the absorption spectra of methoxywarfarin and pyranocoumarin do not show any pH dependence. The inability of methoxywarfarin and pyranocoumarin to convert to the anionic form is the likely explanation for the invariance of the absorption spectra with changing pH. The stability of pyranocoumarin may be debatable in acidic solution. A possible general reaction mechanism in the acidic solution is shown in Figure 3.4a. The oxygen atom present in the cyclic ring of pyranocoumarin can capture a proton. The participation of lone pair of electrons of the methoxy group can generate oxonium ion, which causes the opening of a cyclic ring of pyranocoumarin moiety. Subsequent attack of water on the carbon atom of the oxonium ion can form open chain structure of warfarin. However, the absorption experiments performed in non-aqueous solvents eliminate the contribution from the structure expected through ring opening process in the dual absorption pattern of pyranocoumarin. (Figure 3.4b). These observations in structurally constrained warfarin derivatives are in conflict with the earlier structural assignments of warfarin on the sole basis of absorption spectrum.[19] This gives rise to the question: what then is the origin of the two bands.

(a)

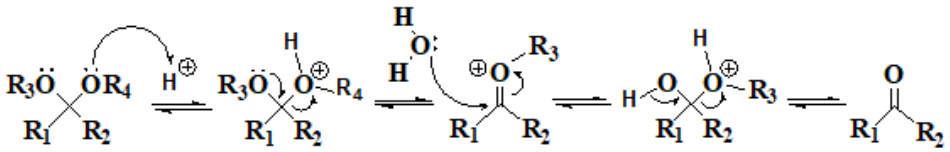

(b)

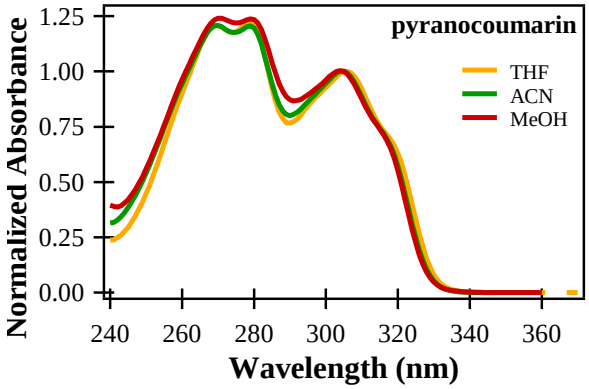

Figure 3.4 (a) General reaction mechanism for the formation of open chain form from the close structure of pyranocoumarin. (b) Normalized absorption spectra of pyranocoumarin in three non-aqueous solvents.

A recent study has reported that the dual absorption of warfarin arises from $n \rightarrow \pi^*$ and $\pi \rightarrow \pi^*$ transitions.[26] The cleavage of a single carbon-carbon bond of warfarin separates the 4-hydroxycoumarin and phenylbutanone (structures are shown in Figure 3.5a) without affecting the conjugation length, the absorption spectrum of warfarin can be considered to be a combination of the absorption spectra of the two moieties. Negligible absorption due to the $n \rightarrow \pi^*$ transition of the keto-carbonyl group at ~260 nm is observed for phenylbutanone (Figure 3.5a). The absorption spectrum of 4-hydroxycoumarin (Figure 3.5a-b) shows a similar spectral profile and pH dependent nature as that of warfarin. Furthermore, pH independent dual absorption of 4-methoxycoumarin (Figure 3.5c), similar to that of 4-methoxywarfarin, further suggests that the single absorption band at higher pH in both warfarin and 4-hydroxycoumarin (pKa of 4.1) arises due to the anionic species. More importantly, both the transition frequency and the weak intensity of the $n \rightarrow \pi^*$ absorption in phenylbutanone suggest that the $n \rightarrow \pi^*$ transition does not contribute to the dual absorption

of warfarin. These results clearly illustrate that the 4-hydroxycoumarin moiety of warfarin is solely responsible for the dual absorption profile. This is a significant conclusion, although the assignment of the two bands still remains unresolved.

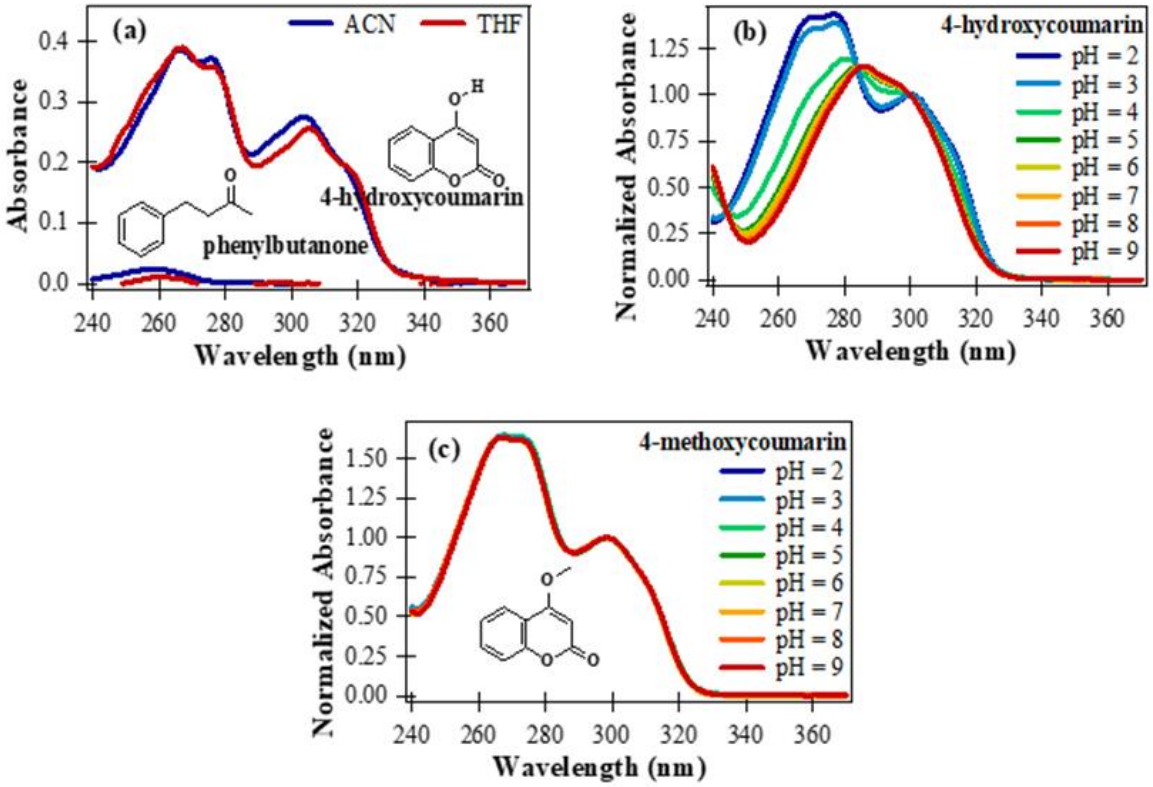

Figure 3.5 Absorption spectra of (a) phenybutanone and 4-hydroxycoumarin in ACN and THF; normalized absorption spectra of (b) 4-hydroxycoumarin and (c) 4-methoxycoumarin in aqueous solutions of different pH. The structures of phenylbutanone, 4-hydroxycoumarin, and 4-methoxycoumarin are shown along with the spectra.

In a previous report on coumarin, the dual absorption was predicted to arise from HOMO→LUMO and HOMO – 1→LUMO transitions.[29-30] As our results suggest that the dual absorption pattern of warfarin arises mainly from the 4-hydroxycoumarin moiety, TDDFT calculations are performed for all possible Franck-Condon transitions on the optimized geometries of 4-hydroxycoumarin (neutral and anionic), 4-methoxycoumarin and warfarin (all coumarin type isomers). The HF molecular orbitals (MO) are also computed.

Schematic representations of all possible transitions in 4-hydroxycoumarin, its anion and 4-methoxycoumarin (within 260-340 nm), the corresponding oscillator strengths (f), and the MOs are shown in Figure 3.6a-c and Figure 3.7a-c. In addition, the schematic representations from similar calculations on different coumarin type isomers of warfarin in the experimental absorption range are also shown in Figure 3.6d-f and Figure 3.7d-f. The involvement of only π orbitals in every transition in Figure 3.6 is clearly shown in a different orientation of molecular orbitals in Figure 3.7. Furthermore, the *n* type orbitals are quite buried and the first *n* type orbital below the HOMO is HOMO – 5 or HOMO – 6 as presented in Figure 3.8 and 3.9. Therefore, these calculations provide further theoretical support to disregard the contribution of $n \rightarrow \pi^*$ transition to the absorption spectrum. According to energy profile diagrams, HOMO→LUMO, HOMO – 1→LUMO $\pi \rightarrow \pi^*$ transitions contribute to the dual absorption of 4-hydroxycoumarin and 4-methoxycoumarin. The dual absorption profile of warfarin at lower pH, can also be elucidated to arise from transition originating from distinct, but energetically close occupied orbitals to the LUMO. The DFT calculated wavelengths show strong synergy with experiments results. Theoretically calculated oscillator strength corresponding to any transition is comparable with the experimentally observed optical density. For deprotonated warfarin and 4-hydroxycoumarin, oscillator strengths are relatively high for HOMO→LUMO transitions, while they are small for other higher energy transitions. These results explain the experimentally observed single absorption nature of the anionic species at high pH. In addition, the calculated absorption wavelength is the highest for the warfarin anion, which also explains the red-shift observed in the warfarin absorption spectrum with increase in pH.

The only observation that is not reproduced by the TDDFT calculations is the relative intensities of the lower and higher wavelength transitions in the experimental absorption spectra of warfarin and 4-hydroxycoumarin at low pH. Therefore, a more accurate, albeit

computationally expensive method, EOM-CCSD, has been used to perform calculations on 4-methoxycoumarin to address this issue (Table 3.2).[31] 4-methoxycoumarin is selected instead of warfarin to reduce computational cost as well as to restrict any contribution from the anionic form in the dual absorption. This calculation has been carried out in the gas phase because the inclusion of solvent effects increases computational costs significantly and moreover, EOM-CCSD calculations with continuum solvation models are known to have large errors.[32] The oscillator strengths predicted by EOM-CCSD are remarkably consistent with experimental absorbance. The absolute values of the excitation energies predicted by EOM-CCSD are higher than those anticipated by TDDFT and experiment, and this is possibly due to cancellation of errors in TDDFT and because EOM-CCSD calculations are performed for the isolated molecule corresponding to the gas phase, while the experimental spectrum is obtained in solution.

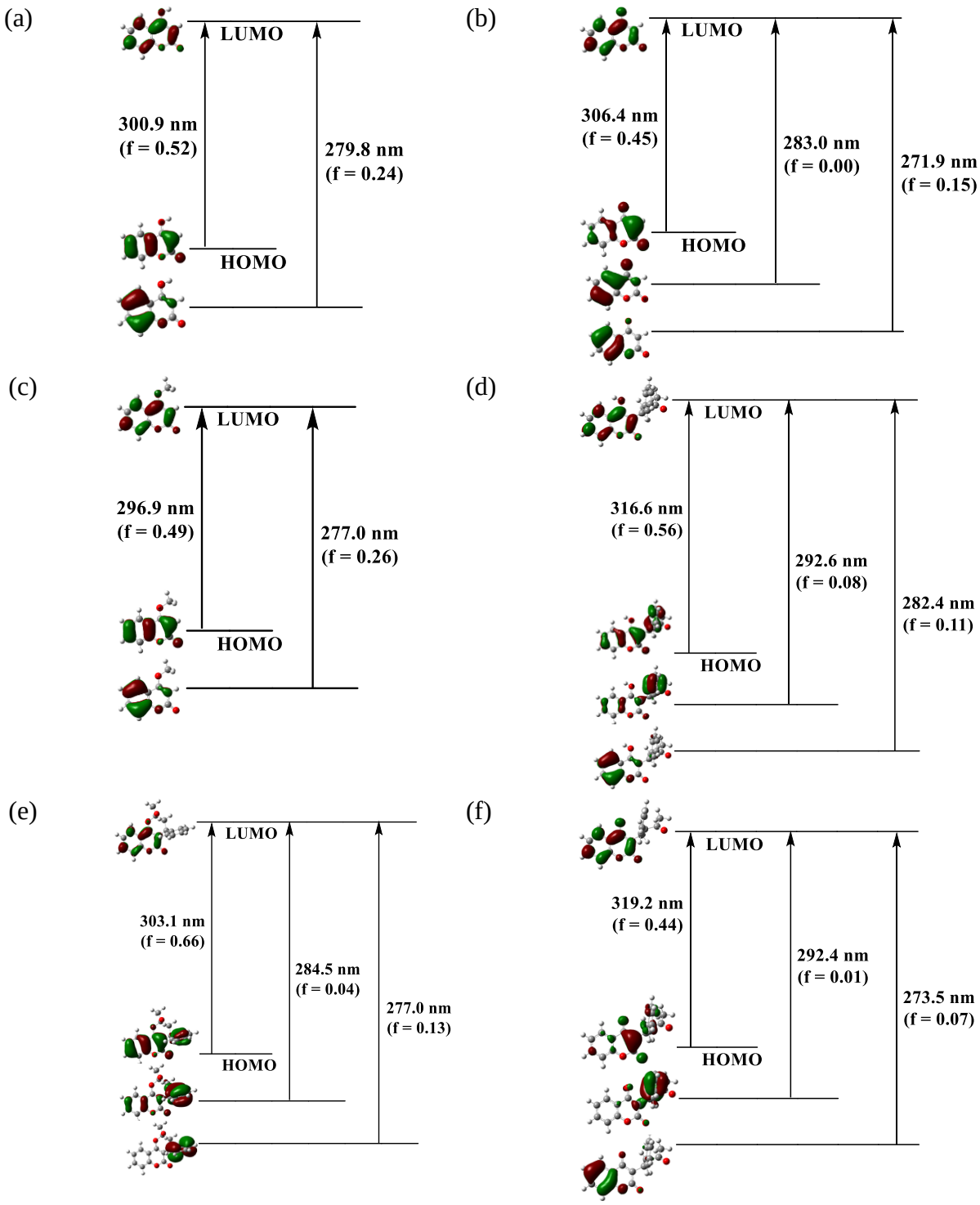

Figure 3.6 Energy level diagrams for (a) 4-hydroxycoumarin and (b) its anion; (c) 4-methoxycoumarin, and warfarin in its (d) open-chain, (e) cyclic hemiketal and (f) anionic forms in aqueous medium (SMD solvation model). Molecular orbitals are calculated at the HF/6-31+G(d,p) level of theory while the excitation energies are calculated using the TDDFT B3LYP/6-31+G(d,p) method.

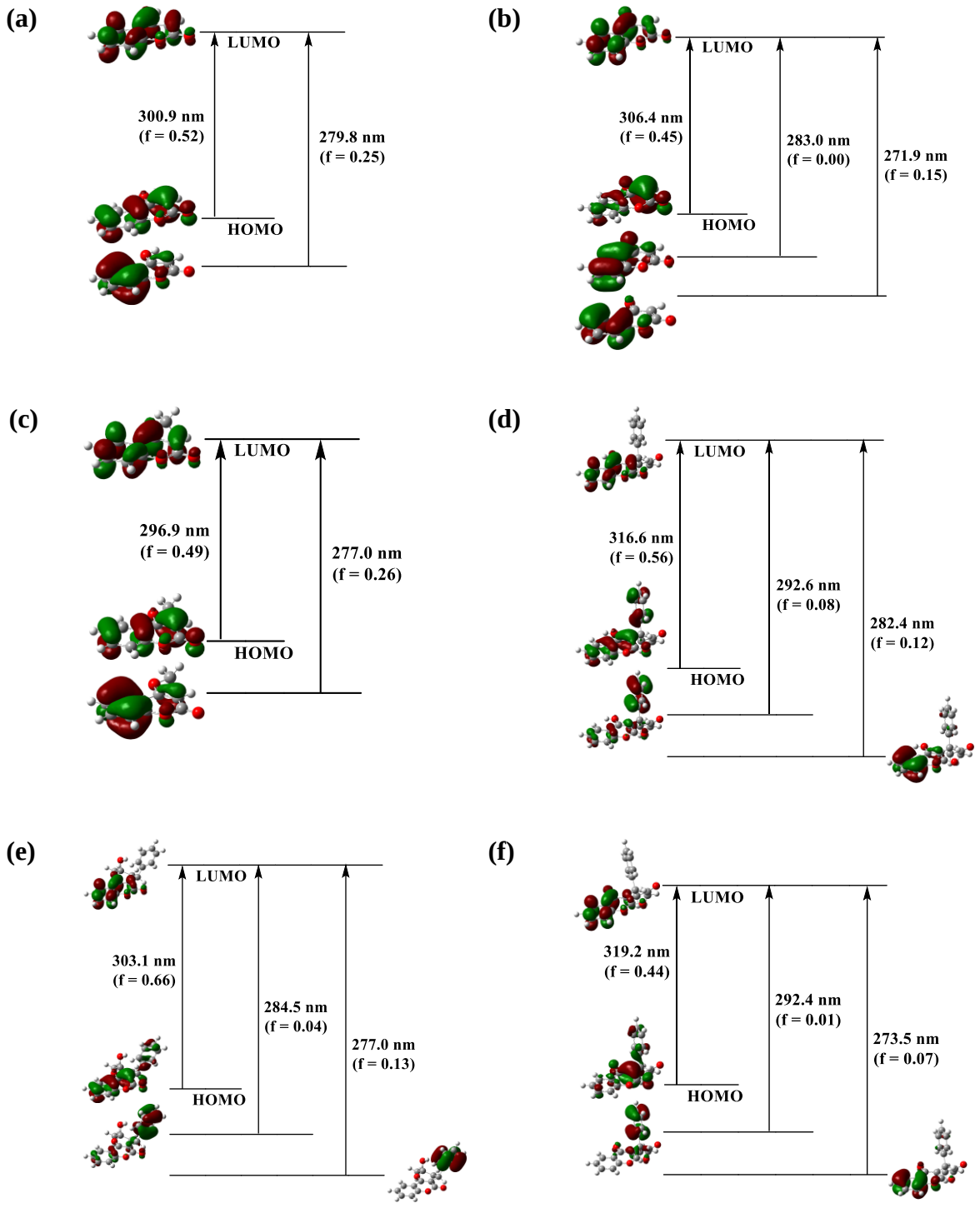

Figure 3.7 Energy level diagrams for (a) 4-hydroxycoumarin and (b) its anion; (c) 4-methoxycoumarin, (d) open-chain form, (e) cyclic hemiketal form and (f) anion of warfarin in water (SMD solvation model). Molecular orbitals are calculated at the HF/6-31+G(d,p) level of theory while the excitation energies are calculated using the TDDFT B3LYP/6-31+G(d,p) method.

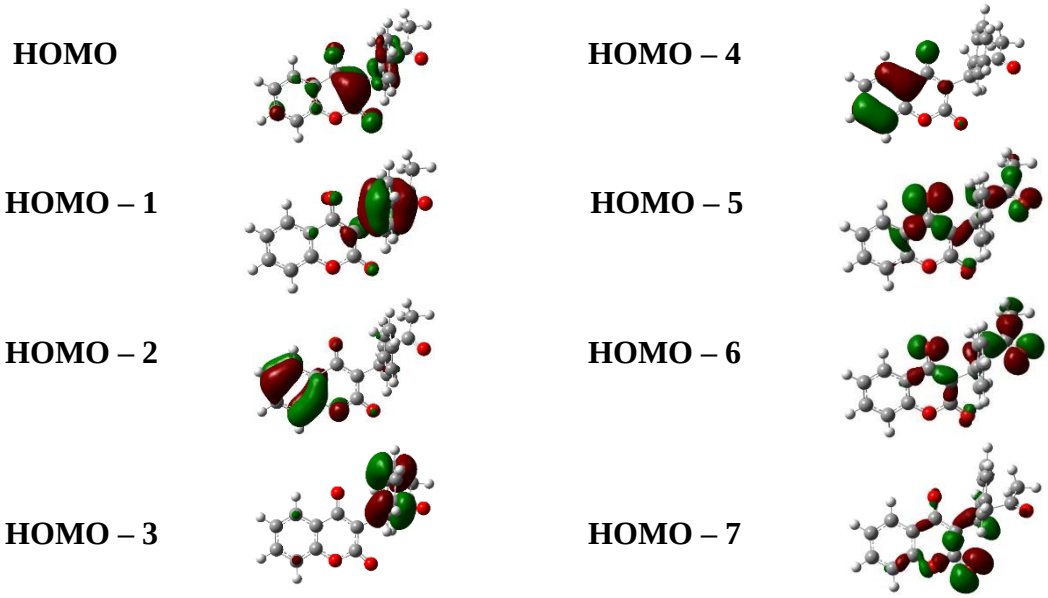

Figure 3.8 Some occupied molecular orbital picture (calculated at the HF/6-31+G(d,p) level of theory) of open-chain and hemiketal form of warfarin in water (SMD solvation model). Molecular orbital dominated by *n* character appears HOMO – 5 and HOMO – 6 energy level respectively for open-chain and hemiketal form.

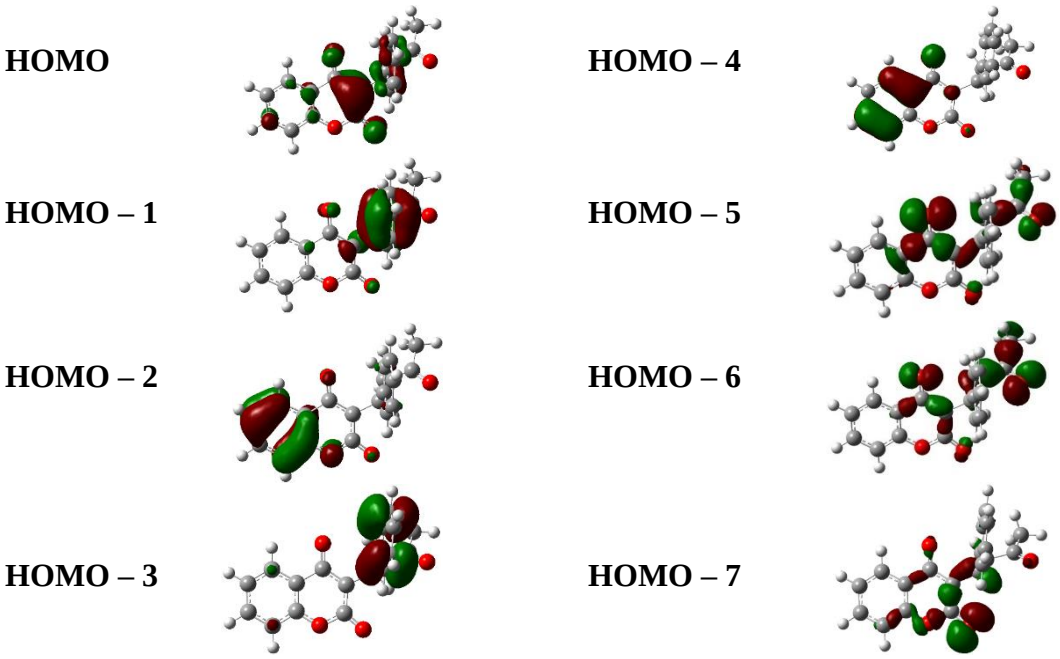

Figure 3.9 Some occupied molecular orbital picture (calculated at the HF/6-31+G(d,p) level of theory) of deprotonated form of warfarin in water (SMD solvation model). Molecular orbital dominated by *n* character appears from HOMO – 5 energy level.

Table 3.2 Calculated spectral parameters for electronic transitions of 4-methoxycoumarin in vacuum at EOM-CCSD/6-31+G(d,p) level of theory.

	Absorption λ_{max} (nm)	**Oscillator strength (f)**	**Predominant orbitals involved**
1st allowed transition	272.0	0.10	HOMO → LUMO
2nd allowed transition	235.1	0.24	(HOMO – 1) → LUMO and HOMO → LUMO

To confirm the theoretical predictions, steady-state and time-resolved emission experiments are performed on warfarin. Similar to previous reports, emission peaks, independent of the excitation wavelengths, are observed at ~356 nm and ~390 nm at pH = 3 and pH = 9, respectively (Figure 3.10a-b).[11, 19, 24] If warfarin exists in its different isomeric forms, multiple distinct emission bands are expected. The single emission band supports the theoretical prediction that the dual absorption arises not from structural isomers, rather due to excitations from two distinct energetically accessible states. As radiative emission occurs exclusively for $S_1 \rightarrow S_0$ transition, any fluorophore excited to S_2 (second excited singlet state) would initially decay to S_1 through internal conversion. This explains the single emission peak of warfarin at 356 nm, irrespective of excitation of molecule to S_2 (280 nm) or S_1 (310 nm). However, at pH = 9, the red shifted single emission peak at 392 nm is the emission of the anionic form of warfarin. The results obtained from the DFT calculations on excited state structures of warfarin (Table 3.3) agree well with the experimental results.

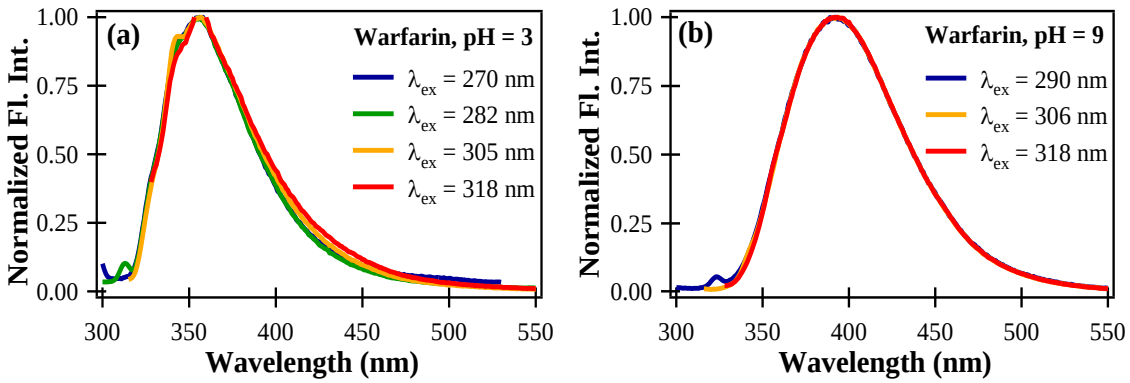

Figure 3.10 Normalized emission spectra of warfarin in (a) pH = 3 and (b) pH = 9 at different excitation wavelengths.

Table 3.3 Calculated spectral parameters for emission of various forms of warfarin in water (SMD solvation model). Experimental emission maxima are also given for comparison.

Structure	**Open Chain (I)**	**Hemiketal (III)**	**Anion**
Calculated λ_{em} (nm)	341.1	349.0	374.0
Oscillator strength (f)	0.72	0.69	0.42
Experimental λ_{em} (nm)	356		392

Earlier studies, limited by instrumental resolution, have speculated ultrafast excited state dynamics of warfarin to be responsible for single emission band in steady state fluorescence spectra. Time resolved emission experiments on warfarin at pH = 3 and pH = 9 with λ_{ex} = 310 nm are performed. Time profiles, collected at several wavelengths across the steady state fluorescence spectra (Figure 3.11a-b) exhibit a uniform decay rate at pH = 3 and pH = 9, irrespective of emission wavelengths, indicating the absence of any excited state dynamic process of time scale slower than 50 ps in warfarin. A single exponential fit to the emission time profile at 360 nm provides the fluorescence lifetime of warfarin at pH = 3 to be ~55 ps. Emission time profiles of deprotonated warfarin at pH = 9 also indicate a constant, yet slower, decay rate of ~125 ps irrespective of the emission wavelength.

These observed emission lifetimes are consistent with the fluorescence quantum yields (φ) at pH = 3 ($\varphi = 2.71\times10^{-3}$) and pH = 9 ($\varphi = 4.77\times10^{-3}$), calculated using anthracene as a standard reference compound at its excitation wavelength (305 nm) in cyclohexane (φ = 0.36).[33] The calculated non-radiative decay rate, observed to be ~2.3 times slower at pH = 9, further confirm the presence of the anionic species at higher pH. The rigidity due to extended conjugation in the anion diminishes the non-radiative decay processes and thereby increases the emission quantum yield as well as emission lifetime of warfarin anion. As discussed earlier, our theoretical calculations illustrate that a single species of deprotonated warfarin is present in solution at higher pH.

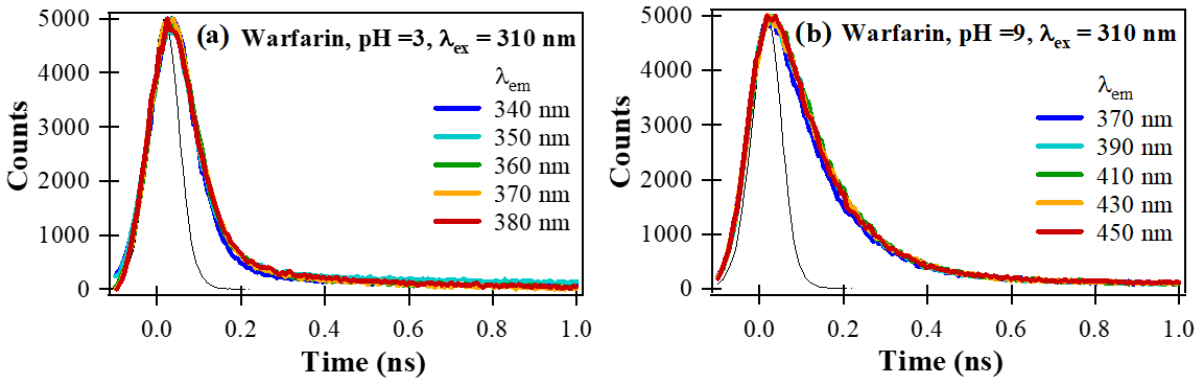

Figure 3.11 Time-resolved fluorescence profiles of warfarin in (a) pH = 3 and (b) pH = 9 at different emission wavelengths, as indicated (λ_{ex} = 310 nm). Black solid line represents instrumental response function (IRF).

Since warfarin is used as an anticoagulant drug as well as a prototype fluorescent probe in biology, it is crucial to ascertain which isomeric form of warfarin binds to HSA. The reported X-ray diffraction data of the crystal structure of warfarin-HSA complex are consistent with the open-chain form of the warfarin molecule,[34] however, the protonated or deprotonated status of warfarin, when bound to HSA cannot be determined from X-ray diffraction. To determine the protonation status of warfarin in the enzyme environment, we perform absorption and emission experiments of warfarin-HSA complex at three different

pH values (3, 7.4 and 9). Although, HSA is not in its native form in the solution of pH 3 and 9,[35-36] the extent of denaturation for each subdomain is different..[37] Therefore, the structure of the binding domain of warfarin might remain the same even at different pH conditions. The absorption spectrum at any pH value exhibits a single absorption band at ~310 nm (Figure 3.12a). The emission spectrum shows a single fluorescence peak at ~382 nm (Figure 3.12b). Interestingly, both absorption as well as emission spectra of HSA bound warfarin are almost independent of pH. The similarity between the absorption spectra of warfarin, when bound to HSA, and its deprotonated form indicates that warfarin is present in the open-chain anionic form in HSA binding pocket. However, the emission spectrum shows ~10 nm blue-shift from that obtained for deprotonated warfarin in aqueous solution (pH = 9). The high micro-viscosity of the binding pocket, as compared to the surrounding, can elucidate the blue shift of the emission maximum. In a previous report,[38] a gradual blue shift of warfarin emission maxima has been reported with increasing viscosity of the solvent. The above experimental results also suggest that pH of the protein solution has minimal effect on the warfarin binding site, and that the warfarin molecule is sequestered in the protein pocket.

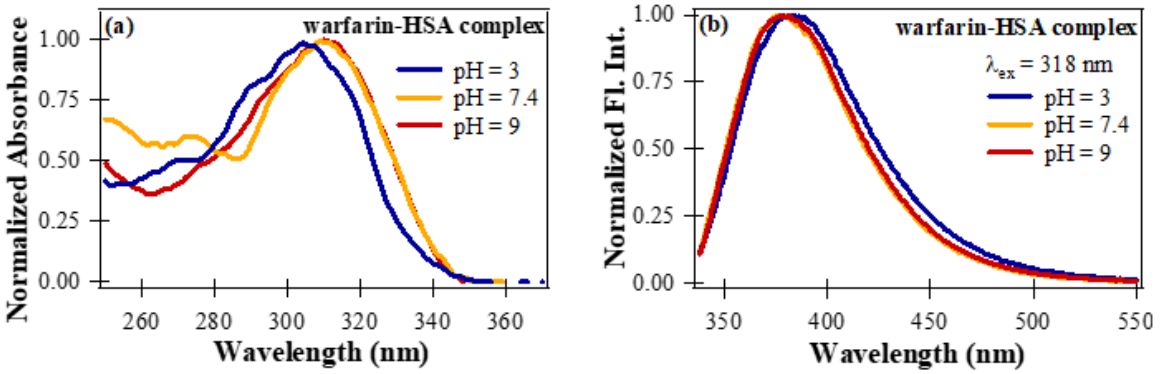

Figure 3.12 (a) Normalized absorption spectra of warfarin-HSA complex in aqueous solutions of different pH, HSA solutions in corresponding pH were used as reference during

UV-Vis absorption experiments. (b) Normalized emission spectra of warfarin-HSA complex in aqueous solutions of different pH (λ_{ex} = 318 nm).

3.4 Conclusions

Using a combined theoretical and experimental study of warfarin, we confirm that only coumarin moiety of warfarin is solely responsible for the absorption spectrum of warfarin in its aqueous form. We demonstrate that the manifestation of dual absorption feature in the absorption spectrum is not associated with the existence of multiple isomeric forms of warfarin in solution, rather due to excitations arising from two closely spaced occupied molecular orbitals to the lowest unoccupied molecular orbital. Our study also illustrates that the ring-chain isomerism of molecules structurally analogous to warfarin, as reported in previous studies, cannot be explained using the spectral characteristics of the warfarin absorption spectrum. Further, this comprehensive study eliminates the possibility of $n \rightarrow \pi^*$ transition contributing to the dual absorption feature of warfarin. The steady state and the time resolved emission experiments provide additional support to distinguish between the neutral and the deprotonated isomers of warfarin. Furthermore, these results allow us to determine that warfarin exists in the open-chain anionic form in the active site of HSA. Finally, as the coumarin moiety which mostly contributes to the absorption and emission spectrum of warfarin, is present in many drugs, our study will be helpful in the investigation of various drug-receptor interactions.

3.5 References

1. Li, T.; Chang, C. Y.; Jin, D. Y.; Lin, P. J.; Khvorova, A.; Stafford, D. W., Identification of the gene for vitamin K epoxide reductase. *Nature* **2004,** *427*, 541-544.

2. Rost, S.; Fregin, A.; Ivaskevicius, V.; Conzelmann, E.; Hörtnagel, K.; Pelz, H. J.; Lappegard, K.; Seifried, E.; Scharrer, I.; Tuddenham, E. G.; Müller, C. R.; Strom, T. M.; Oldenburg, J., Mutations in VKORC1 cause warfarin resistance and multiple coagulation factor deficiency type 2. *Nature* **2004,** *427*, 537-541.

3. Mohr, J. P.; Thompson, J. L. P.; Lazar, R. M.; Levin, B.; Sacco, R. L.; Furie, K. L.; Kistler, J. P.; Albers, G. W.; Pettigrew, L. C.; Adams, H. P.; Jackson, C. M.; Pullicino, P., A comparison of warfarin and aspirin for the prevention of recurrent ischemic stroke. *N. Engl. J. Med.* **2001,** *345*, 1444-1451.

4. Peyrin, E.; Guillaume, Y. C.; Guinchard, C., Characterization of solute binding at human serum albumin site II and its geometry using a biochromatographic approach. *Biophys. J* **1999,** *77*, 1206-1212.

5. Liu, R.; Perez-Aguilar, J. M.; Liang, D.; Saven, J. G., Binding site and affinity prediction of general anesthetics to protein targets using docking. *Anesth. Analg.* **2012,** *114*, 947-955.

6. Nicholson, J. P.; Wolmarans, M. R.; Park, G. R., The role of albumin in critical illness. *Br. J. Anaesth.* **2000,** *85*, 599-610.

7. CF., C., Optical studies of drug-protein complexes. IV. The interaction of warfarin and dicoumarol with human serum albumin. *Mol. Pharmacol.* **1970,** *1*, 1-12.

8. Rosengren, A. M.; Karlsson, B. C.; Nicholls, I. A., Monitoring the distribution of warfarin in blood plasma. *ACS Med. Chem. Lett.* **2012,** *3*, 650-652.

9. Smirnova, T. D.; Nevryueva, N. V.; Shtykov, S. N.; Kochubei, V. I.; Zhemerichkin, D. A., Determination of warfarin by sensitized fluorescence using organized media. *J. Anal. Chem.* **2009,** *64*, 1114-1119.

10. Vasquez, J. M.; Vu, A.; Schultz, J. S.; Vullev, V. I., Fluorescence enhancement of warfarin induced by interaction with beta-cyclodextrin. *Biotechnol. Prog.* **2009,** *25*, 906-914.

11. Al-Dubaili, N.; Saleh, N., Sequestration Effect on the Open-Cyclic Switchable Property of Warfarin Induced by Cyclodextrin: Time-Resolved Fluorescence Study. *Molecules* **2017,** *22*, 1326.

12. Otagiri, M.; Imai, T.; Koinuma, H.; Matsumoto, U., Spectroscopic study of the interaction of coumarin anticoagulant drugs with polyvinylpyrrolidone. *J. Pharm. Biomed. Anal.* **1989,** *7*, 929-935.

13. Valente, E. J.; Porter, W. R.; Trager, W. F., Conformations of selected 3-substituted 4-hydroxycoumarins in solution by nuclear magnetic resonance. Warfarin and phenprocoumon. *J. Med. Chem.* **1978,** *21*, 231-234.

14. Valente, E. J.; Lingafelter, E. C.; Porter, W. R.; Trager, W. F., Structure of warfarin in solution. *J. Med. Chem.* **1977,** *20*, 1489-1493.

15. Nowak, P. M.; Sagan, F.; Mitoraj, M. P., Origin of Remarkably Different Acidity of Hydroxycoumarins-Joint Experimental and Theoretical Studies. *J. Phys. Chem. B* **2017,** *121*, 4554-4561.

16. Giannini, D. D.; Chan, K. K.; Roberts, J. D., Carbon-13 nuclear magnetic resonance spectroscopy. Structure of the anticoagulant warfarin and related compounds in solution. *Proc. Natl. Acad. Sci. U. S. A.* **1974,** *71*, 4221-4223.

17. Pisklak, M.; Maciejewska, D.; Herold, F.; Wawer, I., Solid state structure of coumarin anticoagulants: warfarin and sintrom. C-13 CPMAS NMR and GIAO DFT calculations. *J. Mol. Struct.* **2003,** *649*, 169-176.

18. Guasch, L.; Peach, M. L.; Nicklaus, M. C., Tautomerism of Warfarin: Combined Chemoinformatics, Quantum Chemical, and NMR Investigation. *J. Org. Chem.* **2015,** *80*, 9900-9909.

19. Karlsson, B. C. G.; Rosengren, A. M.; Andersson, P. O.; Nicholls, I. A., The spectrophysics of warfarin: Implications for protein binding. *J. Phys. Chem. B* **2007,** *111*, 10520-10528.

20. Dar, A. A.; Chat, O. A., Cosolubilization of Coumarin30 and Warfarin in Cationic, Anionic, and Nonionic Micelles: A Micelle-Water Interfacial Charge Dependent FRET. *J. Phys. Chem. B* **2015,** *119*, 11632-11642.

21. Kumar, P.; Kumar, V.; Gupta, R., Detection of the anticoagulant drug warfarin by palladium complexes. *Dalton Trans.* **2017,** *46*, 10205-10209.

22. Guasch, L.; Sitzmann, M.; Nicklaus, M. C., Enumeration of Ring-Chain Tautomers Based on SMIRKS Rules. *J. Chem. Inf. Model.* **2014,** *54*, 2423-2432.

23. Karlsson, B. C. G.; Olsson, G. D.; Friedman, R.; Rosengren, A. M.; Henschel, H.; Nicholls, I. A., How Warfarin's Structural Diversity Influences Its Phospholipid Bilayer Membrane Permeation. *J. Phys. Chem. B* **2013,** *117*, 2384-2395.

24. Karlsson, B. C. G.; Rosengren, A. M.; Andersson, P. O.; Nicholls, I. A., Molecular Insights on the Two Fluorescence Lifetimes Displayed by Warfarin from Fluorescence Anisotropy and Molecular Dynamics Studies. *J. Phys. Chem. B* **2009,** *113*, 7945-7949.

25. Malde, A. K.; Stroet, M.; Caron, B.; Visscher, K. M.; Mark, A. E., Predicting the Prevalence of Alternative Warfarin Tautomers in Solution. *J. Chem. Theory Comput.* **2018,** *14*, 4405-4415.

26. Kumari, R.; Nath, M., Synthesis and characterization of novel trimethyltin(IV) and tributylltin(IV) complexes of anticoagulant, WARFARIN: Potential DNA binding and plasmid cleaving agents. *Inorg. Chem. Commun.* **2018,** *95*, 40-46.

27. Rosengren, A. M.; Karlsson, B. C. G., Spectroscopic evidence for the presence of the cyclic hemiketal form of warfarin in aqueous solution: Consequences for bioavailability. *Biochem. Biophys. Res. Commun.* **2011,** *407*, 318-320.

28. Chou, P. T.; Martinez, M. L.; Clements, J. H., Reversal of excitation behavior of proton-transfer vs. charge-transfer by dielectric perturbation of electronic manifolds. *J. Phys. Chem.* **1993,** *97*, 2618-2622.

29. Song, P. S.; Gordon, W. H., 3rd, A spectroscopic study of the excited states of coumarin. *J. Phys. Chem.* **1970,** *74*, 4234-4240.

30. Moore, T. A.; Harter, M. L.; Song, P.-S., Ultraviolet spectra of coumarins and psoralens. *J. Mol. Spectrosc.* **1971,** *40*, 144-157.

31. Caricato, M.; Trucks, G. W.; Frisch, M. J.; Wiberg, K. B., Oscillator Strength: How Does TDDFT Compare to EOM-CCSD? *J. Chem. Theory Comput.* **2011,** *7*, 456-466.

32. Ren, S.; Harms, J.; Caricato, M., An EOM-CCSD-PCM Benchmark for Electronic Excitation Energies of Solvated Molecules. *J. Chem. Theory Comput.* **2017,** *13*, 117-124.

33. Berlman, I. B., *Handbook of Fluorescence Spectra of Aromatic Molecules*. Academic Press: New York, 1971.

34. Petitpas, I.; Bhattacharya, A. A.; Twine, S.; East, M.; Curry, S., Crystal structure analysis of warfarin binding to human serum albumin - Anatomy of drug site I. *J. Biol. Chem.* **2001,** *276*, 22804-22809.

35. Shaw, A. K.; Pal, S. K., Spectroscopic studies on the effect of temperature on pH-induced folded states of human serum albumin. *J Photochem Photobiol B* **2008,** *90* (1), 69-77.

36. Wilting, J.; van der Giesen, W. F.; Janssen, L. H.; Weideman, M. M.; Otagiri, M.; Perrin, J. H., The effect of albumin conformation on the binding of warfarin to human serum albumin. The dependence of the binding of warfarin to human serum albumin on the hydrogen, calcium, and chloride ion concentrations as studied by circular dichroism, fluorescence, and equilibrium dialysis. *J Biol Chem* **1980,** *255*, 3032-7.

37. Wallevik, K., Reversible denaturation of human serum albumin by pH, temperature, and guanidine hydrochloride followed by optical rotation. *J Biol Chem* **1973,** *248*, 2650-2655.

38. Kasaimorita, S.; Horie, T.; Awazu, S., INFLUENCE OF THE N-B TRANSITION OF HUMAN-SERUM ALBUMIN ON THE STRUCTURE OF THE WARFARIN-BINDING SITE. *Biochim. Biophys. Acta* **1987,** *915*, 277-283.

Chapter 4

The Transition of a Deep Eutectic Solution to Aqueous Solution: A Dynamical Perspective of the Dissolved Solute

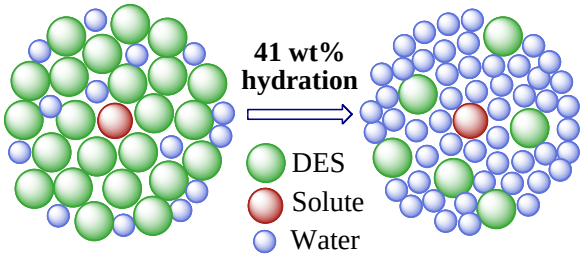

4.1 Introduction

Fuelled by searching for environmentally benign solvents for sustainable chemical processes, deep eutectic solvents (DESs) have emerged as green solvents with a wide range of applications.[1-5] A typical DES consists of an hydrogen bond acceptor (HBA) and an hydrogen bond donor (HBD), mixed in the eutectic molar ratio.[3, 6-8] DES nanostructures, stabilized by inter-component hydrogen bond interactions, can be further tuned by the addition of cosolvents capable of disrupting the native hydrogen bond networks.[6-10] As water can act as both HBA and HBD, these neoteric solvents are highly water-miscible and hygroscopic.[11-12] Recent reports demonstrate that water addition in the eutectic mixtures alters the DES nanostructures and consequently impacts their physicochemical properties.[6] Trends in these properties suggest an upper limit of DES hydration, above which, DES behaves like an aqueous solution.[13-15]

Reline, composed of urea (HBD) and choline chloride (ChCl, HBA) in a 2:1 molar ratio, is one of the most widely studied DESs. This solvent has extensive use in biodiesel synthesis, surface coating, and enzymatic reactions.[16-18] Owing to the hygroscopic nature of both urea and ChCl, the presence of water changes the macroscopic properties of reline and perturbs the DES nanostructure.[19] Experimental and theoretical studies have reported water's effect on the physicochemical properties and molecular arrangement of reline.[6, 15, 20-22] Notably, an unusual transition from an ionic mixture ("water in reline") to an aqueous solution ("reline in water") at 51 wt% water was recently reported by Hammond et al. using neutron diffraction experiments and empirical potential surface refinement (EPSR).[8]

Although various reports studied the disruption of reline nanostructure at certain hydration levels,[6-7, 9, 15] all the studies focused on understanding the phenomenon from the solvent's perspective in the absence of any dissolved solute. The effect of increasing water content in reline from the solute's perspective has yet to be explored. A favorable arrangement of the

DES components around the solute provides an ideal environment for applications like selective catalysis and efficient synthesis.[2] The disruption of the preferred molecular organization in the presence of water might perturb the favorable solute-reline interactions, limiting the use of reline in such applications. Furthermore, water is often intentionally added to improve the DES properties, for example, to lower viscosity.[6, 15] Does the solute sense the transition from a heterogeneous ionic mixture to an aqueous solution at the same water content reported by Hammond et al.? In other words, what is the hydration limit above which the interactions between the solute molecule and the DES components cease to exist?

Herein, we report the polarization-selective evolution of the solute's vibrational frequencies, which provides the answers to the questions mentioned above. We also perform molecular dynamics (MD) simulations on different reline-water systems in the solute's presence to obtain a molecular understanding of the solute-solvent interactions at different hydration levels. The structural dynamics of the solvent produce frequency evolution within its inhomogeneously broadened vibrational bands. These dynamics are quantified by the frequency-frequency correlation function (FFCF) through time-dependent line shape analysis of two dimensional infrared (2D IR) spectra.[23-24] When dissolved in a relatively slow-moving solvent, the solute can reorient on a much faster timescale than the solvent's complete structural evolution. The rapid reorientation of the solute contributes to a polarization selectivity of the frequency evolution over time, known as reorientation-induced spectral diffusion (RISD).[25] A recent report on room temperature ionic liquids (RTIL) shows that polarization dependence of the solute's FFCF can distinguish a slowly evolving environment from an aqueous solution.[23] Considering the gradual lowering of viscosity upon increasing water content in the DESs, polarization-selective 2D IR spectroscopy is suitable to identify the transition from a eutectic to an aqueous environment from the solute's perspective.

4.2 Materials and sample preparation

Urea (>99.8%), choline chloride (ChCl, >98.9%), deuterium oxide (D_2O, >99.9%), and ammonium thiocyanate (NH_4SCN, >99.9%) were purchased from Sigma-Aldrich and used without further purification. To avoid any absorption of moisture, choline chloride and urea were dried in a vacuum oven at 373K for 24 hours and then stored in an N_2-filled glove box. Reline and reline–water mixtures were prepared by a previously reported procedure.[6, 15, 26] Reline was prepared in a glove box by mixing urea with ChCl in a 2:1 molar ratio. The mixture was then heated and stirred up to 2 h at 343K. To avoid further contact with moisture, reline was then stored in the glove box. Reline–water mixtures (xW) were prepared by adding x moles of reline to one mole of D_2O. For example, 1:2:3 molar ratios of ChCl/urea/water is referred to as 3W. Reline-water mixtures of 3W, 5W, 10W, and 15W were used for experiments. NH_4SCN was dissolved in reline and reline-water mixtures independently such that the final concentration of a solution is 50 mM for the IR and 2D IR studies.

4.3 Results and discussion

Ammonium thiocyanate (NH_4SCN, >99.9%), being a small solute molecule, reorients at a time scale much faster than that of DES structural dynamics. In addition, the reorientation time scale of the solute is comparable with that of water fluctuation. Therefore, the small thiocyanate solute allows us to obtain the reorientation induced spectral diffusion (RISD) in DES-like environments from polarization selective 2D IR experiments.[25] The anion (chloride)-water interaction is a dominant one in reline-water mixtures and thus it is essential to explore these interactions to obtain a molecular level understanding. Here, SCN^- has a dual advantage. (1) It is a commonly used vibrational probe[26-29] and (2) due to its very small size, SCN^- is capable of mimicking the local water-chloride anion interaction and dynamics

with minimally perturbing the solvent medium. Herein, we have performed polarization-selective 2D IR experiments on ammonium thiocyanate dissolved in reline and reline-water mixtures (Figure 4.1 and 4.2). We prepared a series of aqueous reline mixtures (xW) by mixing x (ranging from 0 to 15) moles of water (D_2O) with one mole of reline. Water-reline molar ratios (xW) of 3W, 5W, 10W, and 15W were used (the detailed weight% and mol% are given in Table 4.1) as solvents along with neat reline and water.

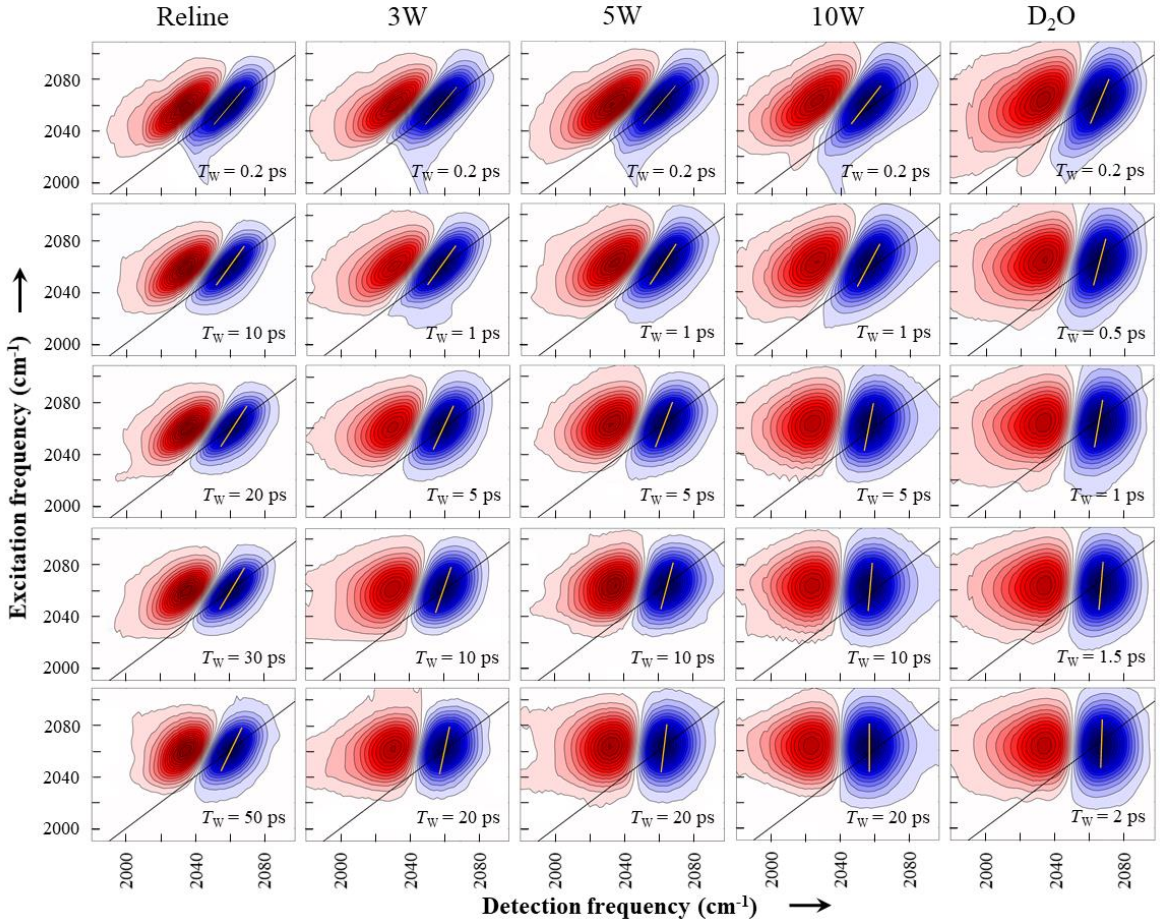

Figure 4.1 2D IR spectra of SCN^- in reline, in reline-water (D_2O) mixtures, and in water (D_2O) at $\langle XXXX \rangle$ polarization condition. The peak pairs correspond to $\bar{\nu}_{CN}$. The water content increases from left to right. For a certain hydration level, T_w increases from top to bottom. The CLS is shown in each 2D IR spectrum with a yellow line.

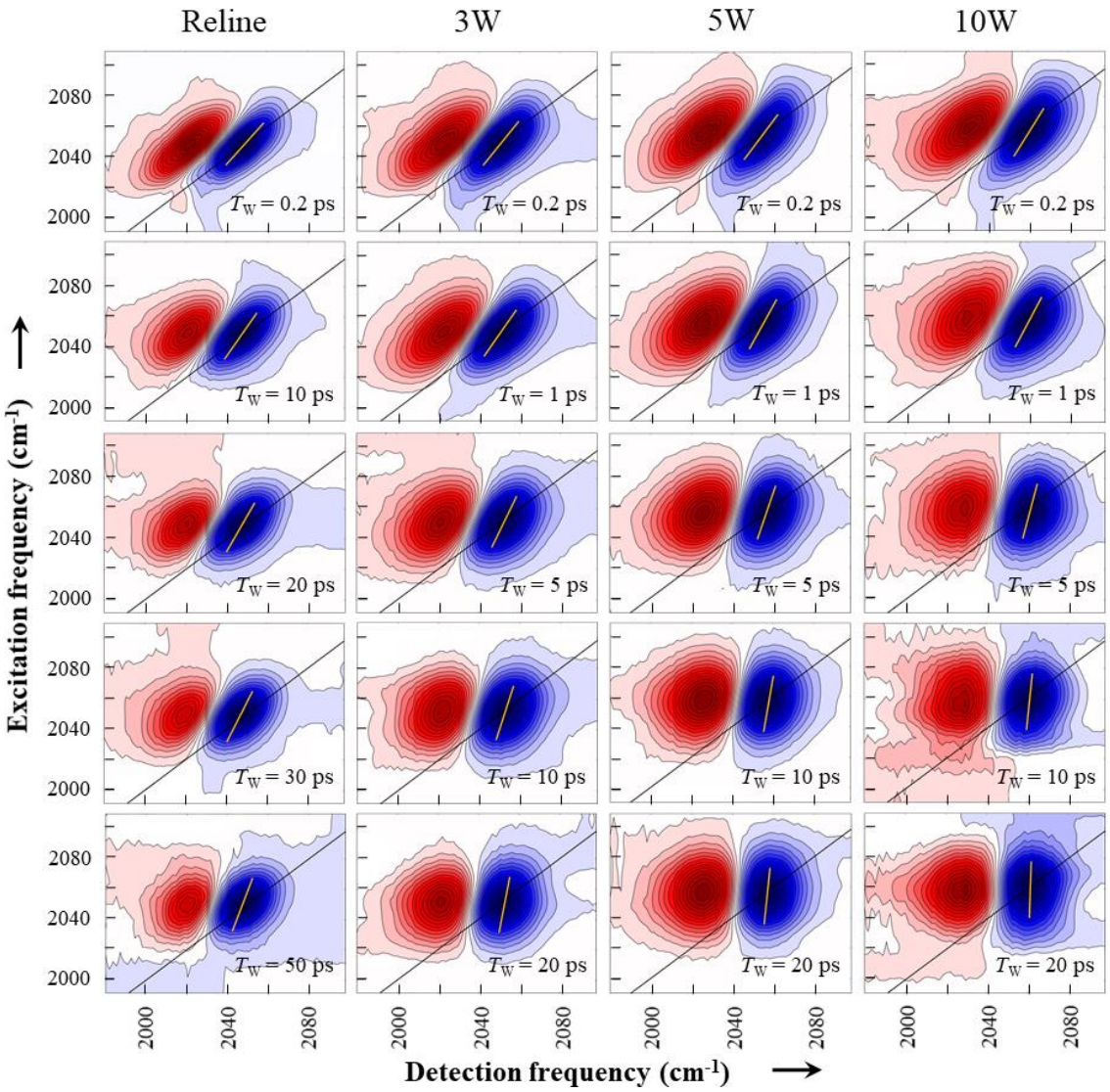

Figure 4.2 2D IR spectra of SCN^- in reline and in reline-water (D_2O) mixtures at $\langle XXYY \rangle$ polarisation. The peak pairs correspond to $\bar{\nu}_{CN}$. The water content increases from left to right. For a certain hydration level, T_w increases from top to bottom. The CLS is shown in each 2D IR spectrum with a yellow line.

Table 4.1 The reline-water composition used in the experiments.

Reline-Water system	Water (mol %)	Water (weight %)
Reline	0	0
3W	50.0	17.22
5W	62.5	25.74
10W	76.9	40.95
15W	83.3	50.98
Water	100.0	100

In the 2D IR experiments, three ultrashort femtosecond pulses are focused on the sample at different time delays. The time delay between pulses 1 and 2 is τ, and that between 2 and 3 is T_w. Owing to the structural dynamics of the solvent molecules and the reorientation of the solute, the initial CN stretching frequencies of the solute change as a function of T_w. For a particular T_w, 2D IR spectrum (Figure 4.1 and 4.2) correlates the initial solute frequencies after first pulse interaction (ω_τ, excitation frequencies) with the final solute frequencies after third pulse interaction (ω_t, detection frequencies). The blue peaks ($\omega_\tau \sim 2060$ cm^{-1}, $\omega_t \sim 2060$ cm^{-1}) correspond to v = 0→1 transition and the red peaks ($\omega_\tau \sim 2060$ cm^{-1}, $\omega_t \sim 2030$ cm^{-1}) correspond to v = 1→2 transitions, shifted by the vibrational anharmonicity along ω_t. The 2D IR peaks are diagonally elongated at a shorter T_w due to a greater correlation between the initial and the final CN frequencies. However, the correlation decreases with the evolution of frequencies over time, and the peaks gradually become upright with an increase in T_w. Figure 4.1and 4.2 indicates that the peaks become upright at a shorter T_w as reline's water content increases. As the faster structural dynamics of the solvent leads to a faster correlation decay, the T_w -dependent 2D IR spectra in different solvation environment are consistent with the decrease in the DES viscosity upon water addition (Table 4.2).

Table 4.2 Viscosity of reline upon addition of water.

Reline-Water system	Viscosity measured at 33.5 ºC (cP)
Reline	>600
3W	11.6
5W	5.6
10W	2.6
15W	1.9
Water	0.74

We have extracted the FFCF encoded in the T_w-dependent 2D IR spectra for two different polarization conditions, $\langle XXXX \rangle$ and $\langle XXYY \rangle$, in terms of the center line slope (CLS) decay[23] (Figure 4.3 and Tables 4.3-4.4). For reline, the CLS for the $\langle XXXX \rangle$ polarization (green) shows a slower decay than that for the $\langle XXYY \rangle$ polarization (yellow). The polarization-selective CLS decays are also observed for 3W and 5W, albeit the difference in the decays decreases with the increase in the water content. Interestingly, the CLS decays become identical for both $\langle XXXX \rangle$ and $\langle XXYY \rangle$ polarization conditions at 10W within experimental error. Further addition of water shows no polarization-dependence of the CLS decays.

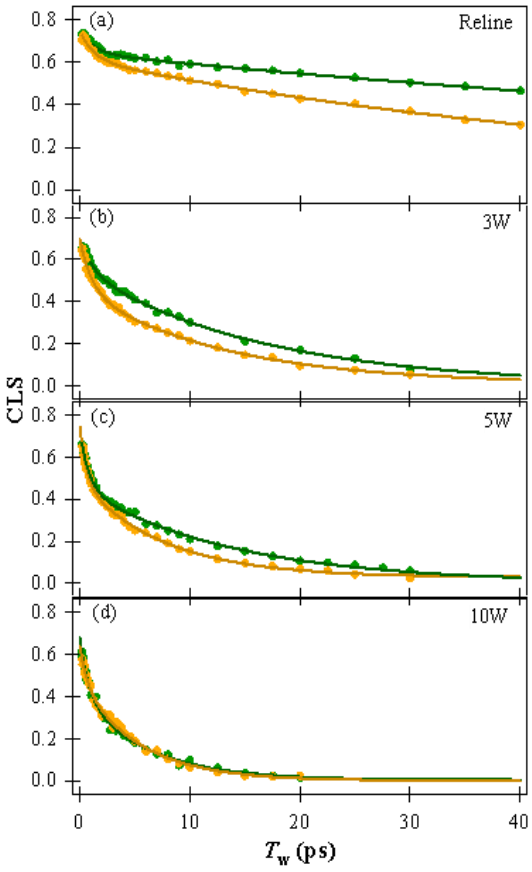

Figure 4.3 CLS decay curves of SCN^- in reline and in reline-water mixtures for $\langle XXXX \rangle$ (green) and $\langle XXYY \rangle$ (yellow) polarization conditions. Polarization selectivity is observed for reline, 3W, and 5W. The CLS decays become identical at 10W within experimental error.

Table 4.3 Bi-exponential fitting parameters of SCN^- CLS decay for $\langle XXXX \rangle$ polarization in reline, reline-water mixtures, and water(D_2O). ($a_1 + a_2$) denotes the initial CLS value at 200 fs.

	a_1	τ_1 (ps)	a_2	τ_2 (ps)	($a_1 + a_2$)
Reline	0.09±0.00	1.3±0.16	0.64±0.00	123.4±2.46	0.73
3W	0.12±0.01	1.2±0.17	0.54±0.01	16.5±0.56	0.66
5W	0.21±0.01	0.8±0.06	0.44±0.01	4.1±0.36	0.65
10W	0.21±0.03	0.8±0.16	0.39±0.02	6.0±1.03	0.60
15W	0.23±0.03	0.5±0.09	0.35±0.03	3.1±0.32	0.58
D_2O	0.09±0.07	0.2±0.20	0.20±0.08	1.0±0.30	0.29

Table 4.4 Bi-exponential fitting parameters of SCN^- CLS decay for $\langle XXYY \rangle$ polarization in reline, reline-water mixtures, and water(D_2O). ($a_1 + a_2$) denotes the initial CLS value at 200 fs.

	a_1	τ_1 (ps)	a_2	τ_2 (ps)	($a_1 + a_2$)
Reline	0.11± 0.00	1.3±0.13	0.61±0.00	57.7±1.34	0.72
3W	0.20±0.01	1.1± 0.12	0.44±0.01	12.9± 1.41	0.64
5W	0.19± 0.01	0.6±0.05	0.44±0.01	7.7±0.20	0.63
10W	0.13± 0.02	0.7± 0.19	0.46±0.02	5.4± 0.34	0.59
15W	0.25±0.06	0.7±0.18	0.27±0.06	3.5±0.71	0.52
D_2O	0.07± 0.01	0.1± 0.03	0.22±0.01	1.0±0.08	0.29

We have analysed the anisotropy decay kinetics of the different reline-water systems (Figure 4.4 and Table 4.5) to understand the origin of the polarization-dependence of the CLS decays. The CLS decay timescales in both $\langle XXXX \rangle$ and $\langle XXYY \rangle$ polarization conditions are slower than that of the corresponding anisotropy decay timescales (~6 ps) for reline, 3W, and 5W. The CLS decays for 10W and above are either comparable or faster than the anisotropy decays. These results strongly support that the polarization-selective CLS in

Figures 4.3a-c arise from RISD, where the solute reorientation occurs without complete randomization of the DES structure. In a viscous solvent like reline, a component of the solvent structure contributing to the overall CN vibrational band can be considered static on the solute reorientation timescale, giving rise to the polarization selectivity.[23]

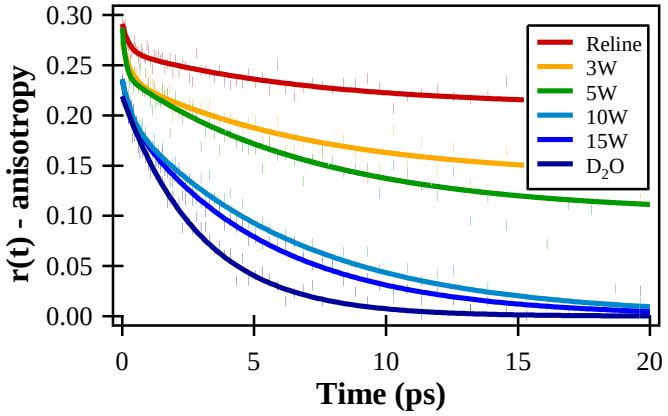

Figure 4.4 Anisotropy decay of SCN^- in reline and in various reline-water (D_2O) mixtures.

Table 4.5 Fitting parameters of anisotropy decay of SCN^- in various reline-water mixtures

Reline-Water molar ratio	a_1	τ_1 (ps)	a_2	τ_2 (ps)	Offset
Reline	10%	0.25 ± 0.08	19%	7.25 ± 1.16	71%
3W	13%	0.30 ± 0.11	36%	7.16 ± 0.07	51%
5W	15%	0.13 ± 0.05	52%	7.20 ± 1.43	33%
10W	16%	0.34 ± 0.15	84%	6.56 ± 0.28	0
15W	14%	0.36 ± 0.08	86%	5.33 ± 0.14	0
D_2O	100%	2.95 ± 0.07	-	-	0

The blue-shift in the CN IR peak (Figure 4.5 and Table 4.6) with increasing water content indicates an increment in solute-water hydrogen bonding interaction.[30] The results obtained from the FTIR and 2D IR experiments provide detail information about the cybotactic region of NH_4SCN in reline and reline-water mixture. The decrease in the difference between the $\langle XXXX \rangle$ and $\langle XXYY \rangle$ decays from reline to 5W arises due to the increase in the

rapidly fluctuating (~1.5 ps)[24, 31] water molecules around the solute with increasing hydration. However, the polarization-selective decays at 3W and 5W demonstrate that the solute is still interacting with the slowly fluctuating reline through the transition dipole's angular motion. In other words, the polarization dependence implies the presence of DES components around the solute at these hydration levels. In fact, the very existence of polarization selective decay for a reline-water mixture is a signature of a solute-DES interaction.

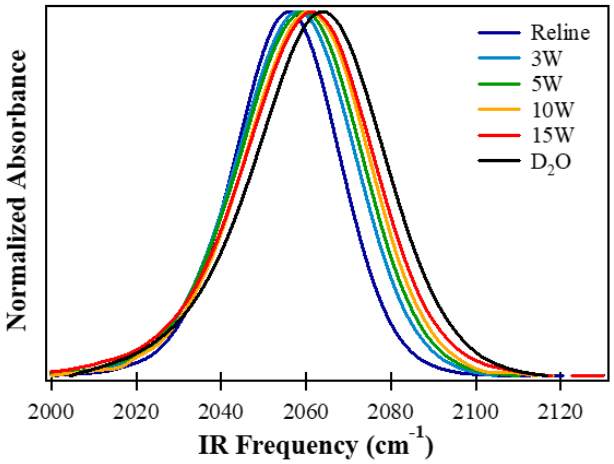

Figure 4.5 FTIR spectrum of ammonium thiocyanate in reline, in various reline-water mixtures, and in neat water. The peak maximum shows a gradual blue-shift with increasing hydration level of the solvent.

Table 4.6 CN stretch peak characteristics of ammonium thiocyanate in reline, reline-water mixtures, and water.

Reline-Water system	IR peak frequency (cm^{-1})	FWHM (cm^{-1})
Reline	2055.6	29.1
3W	2057.6	33.0
5W	2058.6	34.0
10W	2060.5	34.3
15W	2060.6	35.6
Water	2063.2	36.4

At 10W, the solute is predominantly solvated by the water molecules that fluctuate at a timescale faster or comparable to the solute's reorientation (Figure 4.6). This phenomenon gives rise to identical CLS decays at 10W in different polarization conditions. Any further increase in the hydration level (up to neat water) does not further perturb the solvation shell of the solute, and the CLS decays remain identical, independent of polarization conditions. From the solute's perspective, the transition from a deep eutectic solution (solute-DES interaction) to an aqueous solution (only solute-water interaction) occurs at ~10W (41 wt% water). It is to be noted that although the CLS decays become identical at 10W in both the polarization conditions, the CLS decay timescales continue to gradually accelerate beyond 10W (Table 4.3-4.4) with further increase in the water content. This gradual acceleration might imply that the local solvation continues to evolve beyond 10W and thereby contradicts our hypothesis of an aqueous environment around the solute is formed at 41 wt% water.

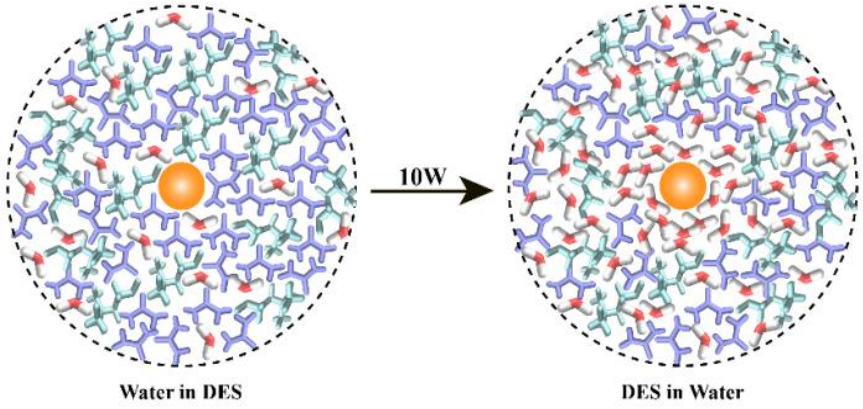

Figure 4.6 Schematic diagram for "Water in DES" and "DES in Water" transition. The solute molecule is represented by an orange sphere. The solute-water interactions replace all the solute-DES interactions at 10W, thereby creating a neat water-like environment around the solute.

To obtain better insights about the local solvation, we have looked into the vibrational anharmonicity. Previous studies of thiocyanate reported that proximity to the cations usually

results in the lowering of the vibrational anharmonicity.[32-35] We have estimated the anharmonicity to gradually increase from ~27 cm^{-1} in reline to ~35 cm^{-1} at 10W (Table 4.7). However, the anharmonicity does not change for 15W and neat water within the experimental error limit. This trend in the anharmonicity is in agreement with the gradual replacement of the ionic DES components around the solute by water molecules up to 10W.

Table 4.7 Anharmonicity of CN stretch of SCN^- in reline, in reline-water(D_2O) mixtures and in water(D_2O).

Reline-water system	Anharmonicity of SCN^- (cm^{-1})
Reline	27.1
3W	30.8
5W	31.9
10W	34.6
15W	34.3
Water	35

We have also performed MD simulations to further probe the local solvation around the solute. The force field parameters for the selected solute which is NH_4SCN are shown in Table 4.8. Although earlier simulation reports investigated the bulk nature of reline-water interaction at different hydration levels,[7, 9, 15] the local solvation around a solute was not explored. We have calculated the spatial distribution function (SDF) which provides the three-dimensional density distribution of urea and choline around the solute in neat reline. Figure 4.7a indicates that, although choline contains a hydroxyl group which can directly interact with the CN, solute-urea interaction is preferred over solute-choline interaction in neat reline. Previous studies of thiocyanate in aqueous solutions reported viscosity dependent slowdown of the solute rotational dynamics due to interactions with small cations with high charge density.[33] The preferential interaction of the solute with urea over choline (albeit a much larger cation) shows that local environment of the solute plays a more

prominent role in DES than the macroscopic viscosity. We have also computed the water/urea and water/choline ratios within 5 and 10 Å of the solute in different reline-water mixtures. The ratios, averaged along the trajectories, show an increase with increasing water content of reline (Table 4.9). However, a very interesting phenomenon is observed when the ratios are plotted as a function of time. Figure 4.7b indicates that the water/urea ratio gradually increases from 3W and reaches the maximum value at 10W. Beyond 10W, this ratio remains constant. However, the ratios keep switching between high and low values, thereby indicating a solvent exchange process where the water molecules around the solute are replaced by the reline components from time to time. The frequency of the solvent exchange increases with increasing water content. It has previously been reported that molecular exchange between solvent components slows down the solvation dynamics and results in a slower spectral diffusion in an aqueous mixture than in water.[36-38] Thus, the simulation results show that the experimental CLS decay timescales can be interpreted on the basis of solvent exchange. Even though the solute senses an overall aqueous environment at 10W, the decrease in the mole fraction of the reline components in the outer solvation shell with increase in water content plausibly leads to a faster solvent exchange and thereby an acceleration of the CLS decay timescales.

Table 4.8 Force field parameters of ammonium thiocyanate (NH_4SCN).

	Atom	q (e)	σ (Å)	ε ($KJ.mol^{-1}$)
SCN^-	S	-0.716271	3.5635	1.046
	C	0.351075	3.3996	0.8786
	N1	-0.634805	3.250	0.7113
NH_4^+	N4	-0.853966	3.250	0.7112
	H1	0.463491	1.069	0.6568

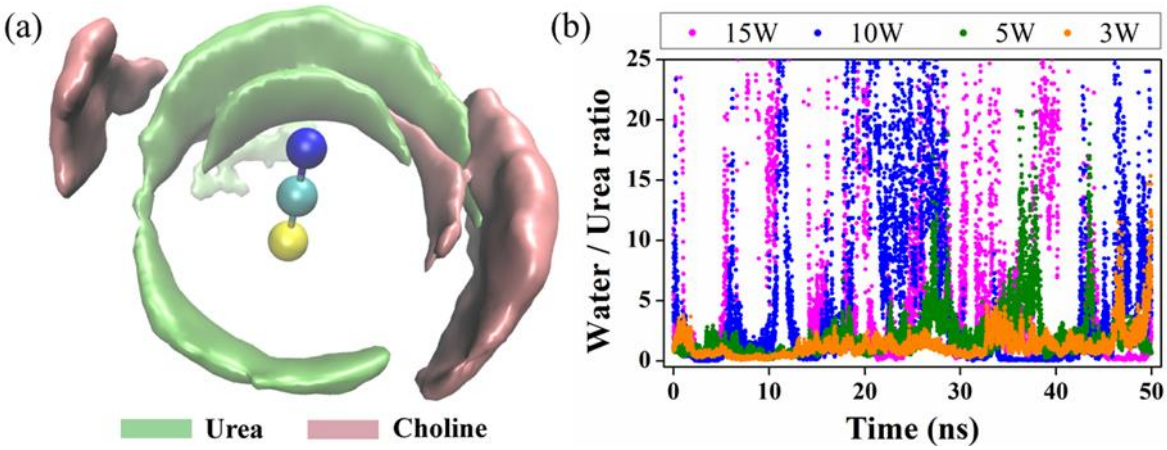

Figure 4.7 (a) Spatial distribution function (SDF) of urea and choline around SCN^- in neat reline. (b) Graph of water/urea ratio within 10 Å of the SCN^- vs time in different reline-water mixtures.

Table 4.9 The water/urea and water/choline ratios within 5 and 10 Å of the SCN^- in different reline-water mixtures.

Reline-Water system	Water/Urea ratio		Water/choline ratio	
	within 5 Å of the SCN^-	within 10 Å of the SCN^-	within 5 Å of the SCN^-	within 10 Å of the SCN^-
Reline	0	0	0	0
3W	1.4	1.0	3.1	2.6
5W	1.7	1.5	4.4	3.8
10W	2.1	1.8	7.9	7.1
15W	4.2	3.8	11.4	11.2
20W	4.8	4.2	14.1	13.6

Overall, our computational results indicate that although water interacts with the solute at 5W, a considerable number of heterogeneous reline constituents persist in the thiocyanate solvation shell. At 10W and above, solute-solvent interactions predominantly arise from thiocyanate-water interactions, subsequently decreasing the heterogeneity around the solute.

This molecular picture was further validated from experiments using the vibrational lifetimes (T_1), and the CLS values at a short T_w (~200 fs) (Table 4.10 and Table 4.3-4.4).

Table 4.10 Population decay time constants of the CN stretch in reline, in reline-water(D_2O) mixtures and in water(D_2O).

DES/D_2O system	Population decay time of SCN^- (ps)
Reline	19.6 ± 0.1
3W	11.4 ± 0.1
5W	10.8 ± 0.1
10W	11.4 ± 0.1
15W	11.6 ± 0.1
D_2O	10.5 ± 0.1

We have measured T_1 for different reline-D_2O mixtures using pump-probe spectroscopy (Figure 4.4 and Table 4.10). In pure reline, T_1 of the CN vibrational mode is ~20 ps. The T_1 values in all other mixtures are constant (~11 ps) within experimental error. The CN vibration's coupling with the resonant water mode (bending + libration) through hydrogen bond interaction can explain the invariability of vibrational relaxation timescales at all hydration levels.[39] The constant T_1 indicates the presence of water in the solute solvation shell, even at 3W. As the thiocyanate vibrational lifetime in H_2O is much shorter than that in D_2O,[40] T_1 in reline-H_2O might be a more sensitive probe of solute hydration. We have additionally measured T_1 for different reline-H_2O mixtures (Table 4.11). Our results show that T_1 of the CN vibrational mode in H_2O gradually decreases with increase in water on content up to 10W. Beyond 10W, T_1 is almost constant with the experimental error. This trend in the lifetime indicates that the solute is predominantly solvated by water molecules at 10W. The initial amplitude of the CLS at a very short T_w is a measure of the dynamical heterogeneity around the solute. The decrease in the initial CLS amplitude (Figure 4.3, Table

4.3-4.4) from reline to 10W implies a gradual replacement of slowly moving DES components by fast fluctuating water molecules in the thiocyanate solvation shell.

Table 4.11 Population decay time constants of the CN stretch of SCN^- in reline, in reline-water mixtures and in water (H_2O).

DES/water system	Population decay time of SCN^- (ps)
Reline	19.6 ± 0.1
3W	7.1 ± 0.2
5W	4.9 ± 0.2
10W	2.6 ± 0.3
15W	2.5 ± 0.3
Water	2.0 ± 0.1

4.4 Conclusion

In summary, we provide an upper hydration limit of reline beyond which the solute experiences a water-like environment. Interestingly, our results demonstrate that this upper hydration limit (41 wt% water or 10W) is considerably lower than the limit proposed by Hammond et al. (51 wt% water or 15W) from the neutron diffraction study.[8] However, the diffraction results provided us an upper hydration limit from the solvent's perspective, i.e., when each reline constituent (choline cation, chloride anion, and urea) are solvated by water. The polarization-selective 2D IR results demonstrate that the solute may experience an aqueous environment much before water solvates all the reline constituents. Further, this report illustrates that polarization dependence of the structural dynamics could identify when the solute experiences a transition from the heterogeneous DES environment to an aqueous solution. For a wide range of applications, researchers are presently exploiting hydration as a tool to overcome the limitations of green solvents like DESs and RTILs.[4, 7,

[15, 41] This study opens up an avenue to investigate similar transitions from the solute's perspective for viscous green solvents with varying constituents.

4.5 References

1. Smith, E. L.; Abbott, A. P.; Ryder, K. S., Deep Eutectic Solvents (DESs) and Their Applications. *Chem. Rev.* **2014**, *114*, 11060-11082.

2. Wagle, D. V.; Zhao, H.; Baker, G. A., Deep Eutectic Solvents: Sustainable Media for Nanoscale and Functional Materials. *Acc. Chem. Res.* **2014**, *47*, 2299-2308.

3. Hammond, O. S.; Li, H.; Westermann, C.; Al-Murshedi, A. Y. M.; Endres, F.; Abbott, A. P.; Warr, G. G.; Edler, K. J.; Atkin, R., Nanostructure of the deep eutectic solvent/platinum electrode interface as a function of potential and water content. *Nanoscale Horiz.* **2019**, *4*, 158-168.

4. Liao, H.-G.; Jiang, Y.-X.; Zhou, Z.-Y.; Chen, S.-P.; Sun, S.-G., Shape-Controlled Synthesis of Gold Nanoparticles in Deep Eutectic Solvents for Studies of Structure–Functionality Relationships in Electrocatalysis. *Angew. Chem. Int. Ed.* **2008**, *47*, 9100-9103.

5. Hammond, O. S.; Edler, K. J.; Bowron, D. T.; Torrente-Murciano, L., Deep eutectic-solvothermal synthesis of nanostructured ceria. *Nat. Commun* **2017**, *8*, 14150.

6. Hammond, O. S.; Bowron, D. T.; Edler, K. J., The Effect of Water upon Deep Eutectic Solvent Nanostructure: An Unusual Transition from Ionic Mixture to Aqueous Solution. *Angew. Chem., Int. Ed.* **2017,** *56,* 9782-9785.

7. Kumari, P.; Shobhna; Kaur, S.; Kashyap, H. K., Influence of Hydration on the Structure of Reline Deep Eutectic Solvent: A Molecular Dynamics Study. *ACS Omega* **2018**, *3*, 15246-15255.

8. Ma, C.; Laaksonen, A.; Liu, C.; Lu, X.; Ji, X., The peculiar effect of water on ionic liquids and deep eutectic solvents. *Chem. Soc. Rev.* **2018**, *47*, 8685-8720.

9. Sarkar, S.; Maity, A.; Chakrabarti, R., Microscopic structural features of water in aqueous–reline mixtures of varying compositions. *Phys. Chem. Chem. Phys.* **2021,** *23*, 3779-3793.

10. Shah, D.; Mansurov, U.; Mjalli, F. S., Intermolecular interactions and solvation effects of dimethylsulfoxide on type III deep eutectic solvents. *Phys. Chem. Chem. Phys.* **2019**, *21*, 17200-17208.

11. Dugoni, G. C.; Di Pietro, M. E.; Ferro, M.; Castiglione, F.; Ruellan, S.; Moufawad, T.; Moura, L.; Costa Gomes, M. F.; Fourmentin, S.; Mele, A., Effect of Water on Deep Eutectic Solvent/β-Cyclodextrin Systems. *ACS Sustain. Chem. Eng.* **2019**, *7*, 7277-7285.

12. Durand, E.; Lecomte, J.; Baréa, B.; Dubreucq, E.; Lortie, R.; Villeneuve, P., Evaluation of deep eutectic solvent–water binary mixtures for lipase-catalyzed lipophilization of phenolic acids. *Green Chem.* **2013**, *15*, 2275-2282.

13. Gutierrez, M. a. C.; Ferrer, M. a. L.; Mateo, C. R.; del Monte, F., Freeze-Drying of Aqueous Solutions of Deep Eutectic Solvents: A Suitable Approach to Deep Eutectic Suspensions of Self-Assembled Structures. *Langmuir* **2009**, *25*, 5509-5515.

14. Passos, H.; Tavares, D. J. P.; Ferreira, A. M.; Freire, M. G.; Coutinho, J. o. A. P., Are Aqueous Biphasic Systems Composed of Deep Eutectic Solvents Ternary or Quaternary Systems? *ACS Sustain. Chem. Eng.* **2016**, *4*, 2881-2886.

15. Shah, D.; Mjalli, F. S., Effect of water on the thermo-physical properties of Reline: An experimental and molecular simulation based approach. *Phys. Chem. Chem. Phys.* **2014**, *16*, 23900-23907.

16. Zhang, Q.; De Oliveira Vigier, K.; Royer, S. b.; Jerome, F., Deep eutectic solvents: syntheses, properties and applications. *Chem. Soc. Rev.* **2012**, *41*, 7108-7146.

17. Bucko, M.; Culliton, D.; Betts, A. J.; Bajat, J. B., The Electrochemical Deposition of Zn-Mn Coating from Choline Chlorideâ€“Urea Deep Eutectic Solvent. *Trans. Inst. Met. Finish.* **2017**, *95*, 60-64.

18. Liao, Y. S.; Chen, P. Y.; Sun, I. W., Electrochemical Study and Recovery of Pb Using 1:2 Choline Chloride/Urea Deep Eutectic Solvent: A Variety of Pb Species PbSO4, PbO2, and PbO Exhibits the Analogous Thermodynamic Behavior. *Electrochim. Acta* **2016**, *214*, 265-275.

19. Agieienko, V.; Buchner, R., Densities, Viscosities, and Electrical Conductivities of Pure Anhydrous Reline and Its Mixtures with Water in the Temperature Range (293.15 to 338.15) K. *J. Chem. Eng. Data* **2019**, *64*, 4763−4774.

20. D'Agostino, C.; Gladden, L. F.; Mantle, M. D.; Abbott, A. P.; Ahmed, E. I.; Al-Murshedi, A. Y. M.; Harris, R. C., Molecular and ionic diffusion in aqueous â€“ deep eutectic solvent mixtures: probing inter-molecular interactions using PFG NMR. *Phys. Chem. Chem. Phys.* **2015**, *17*, 15297-15304.

21. Fetisov, E. O.; Harwood, D. B.; Kuo, I. F. W.; Warrag, S. E. E.; Kroon, M. C.; Peters, C. J.; Siepmann, J. I., First-Principles Molecular Dynamics Study of a Deep Eutectic Solvent: Choline Chloride/Urea and Its Mixture with Water. *J. Phys. Chem. B* **2018**, *122*, 1245-1254.

22. Posada, E.; Lopez-Salas, N.; Jimenez Rioboo, R. J.; Ferrer, M. L.; Gutierrez, M. C.; del Monte, F., Reline Aqueous Solutions Behaving As Liquid Mixtures of H-bonded Co-solvents: Microphase Segregation and Formation of Co-continuous Structures As Indicated

by Brillouin and 1H NMR Spectroscopies. *Phys. Chem. Chem. Phys.* **2017**, *19*, 17103-17110.

23. Tamimi, A.; Bailey, H. E.; Fayer, M. D., Alkyl Chain Length Dependence of the Dynamics and Structure in the Ionic Regions of Room-Temperature Ionic Liquids. *J. Phys. Chem. B* **2016**, *120*, 7488-7501.

24. Kwak, K.; Park, S.; Finkelstein, I. J.; Fayer, M. D., Frequency-frequency correlation functions and apodization in two-dimensional infrared vibrational echo spectroscopy: A new approach. *J. Chem. Phys.* **2007**, *127*, 124503-124517.

25. Kramer, P. L.; Nishida, J.; Fayer, M. D., Separation of experimental 2D IR frequency-frequency correlation functions into structural and reorientation-induced contributions. *J. Chem. Phys.* **2015**, *143*, 124505-124516.

26. Cui, Y.; Fulfer, K. D.; Ma, J.; Weldeghiorghis, T. K.; Kuroda, D. G., Solvation dynamics of an ionic probe in choline chloride-based deep eutectic solvents. *Phys. Chem. Chem. Phys.* **2016**, *18*, 31471-31479.

27. Bian, H.; Wen, X.; Li, J.; Chen, H.; Han, S.; Sun, X.; Song, J.; Zhuang, W.; Zheng, J., Ion clustering in aqueous solutions probed with vibrational energy transfer. *Proc. Natl. Acad. Sci. USA* **2011**, *108*, 4737-4742.

28. Li, J.; Bian, H.; Chen, H.; Wen, X.; Hoang, B. T.; Zheng, J., Ion Association in Aqueous Solutions Probed through Vibrational Energy Transfers among Cation, Anion, and Water Molecules. *J. Phys. Chem. B* **2013**, *117*, 4274-4283.

29. Chen, H.; Wen, X.; Guo, X.; Zheng, J., Intermolecular vibrational energy transfers in liquids and solids. *Phys. Chem. Chem. Phys.* **2014**, *16*, 13995-14014.

30. Deb, P.; Haldar, T.; Kashid, S. M.; Banerjee, S.; Chakrabarty, S.; Bagchi, S., Correlating Nitrile IR Frequencies to Local Electrostatics Quantifies Noncovalent Interactions of Peptides and Proteins. *J. Phys. Chem. B* **2016**, *120*, 4034-4046.

31. Kramer, P. L.; Nishida, J.; Giammanco, C. H.; Tamimi, A.; Fayer, M. D., Observation and theory of reorientation-induced spectral diffusion in polarization-selective 2D IR spectroscopy. *J. Chem. Phys.* **2015**, *142*, 184505-184508.

32. Roy, V. P.; Kubarych, K. J., Interfacial Hydration Dynamics in Cationic Micelles Using 2D-IR and NMR. *J. Phys. Chem. B* **2017**, *121*, 9621-9630.

33. Bian, H.; Chen, H.; Zhang, Q.; Li, J.; Wen, X.; Zhuang, W.; Zheng, J., Cation Effects on Rotational Dynamics of Anions and Water Molecules in Alkali (Li+, Na+, K+, Cs+) Thiocyanate (SCN^-) Aqueous Solutions. *J. Phys. Chem. B* **2013**, *117*, 7972-7984.

34. Park, S.; Ji, M.; Gaffney, K. J., Ligand Exchange Dynamics in Aqueous Solution Studied with 2D IR Spectroscopy. *J. Phys. Chem. B* **2010**, *114*, 6693-6702.

35. Kiefer, L. M.; Kubarych, K. J., NOESY-Like 2D-IR Spectroscopy Reveals Non-Gaussian Dynamics. *J. Phys. Chem. Lett.* **2016**, *7*, 3819-3824.

36. Dunbar, J. A.; Arthur, E. J.; White, A. M.; Kubarych, K. J., Ultrafast 2D-IR and Simulation Investigations of Preferential Solvation and Cosolvent Exchange Dynamics. *J. Phys. Chem. B* **2015**, *119*, 6271-6279.

37. Kiefer, LauraÂ M.; Kubarych, K. J., Solvent exchange in preformed photocatalyst-donor precursor complexes determines efficiency. *Chem. Sci.* **2018**, *9*, 1527-1533.

38. Kashid, S. M.; Jin, G. Y.; Chakrabarty, S.; Kim, Y. S.; Bagchi, S., Two-Dimensional Infrared Spectroscopy Reveals Cosolvent-Composition-Dependent Crossover in Intermolecular Hydrogen-Bond Dynamics. *J. Phys. Chem. Lett.* **2017**, *8*, 1604-1609.

39. Hamm, P.; Lim, M.; Hochstrasser, R. M., Vibrational energy relaxation of the cyanide ion in water. *J. Chem. Phys.* **1997**, *107*, 10523-10531

40. Czurlok, D.; Gleim, J.; Lindner, J. r.; Vohringer, P., Vibrational Energy Relaxation of Thiocyanate Ions in Liquid-to-Supercritical Light and Heavy Water. A Fermi Golden Rule Analysis. *J. Phys. Chem. Lett.* **2014**, *5*, 3373–3379.

41. Dong, J. Y.; Hsu, Y. J.; Wong, D. S. H.; Lu, S. Y., Growth of ZnO Nanostructures with Controllable Morphology Using a Facile Green Antisolvent Method. *J. Phys. Chem. C* **2010**, *114*, 8867-8872.

Chapter 5

Dissecting carbonyl vibrational responses of vibrational coupling and hydrogen-bond dynamics of small molecules in complex solvation environments.

5.1 Introduction

Solute−solvent interactions profoundly impact the structure, function, and dynamics of chemical and biological systems. Recently, vibrational probes have been used to interrogate the site-specific interaction and local electrostatic field in various molecular systems.[1-8] Carbonyl groups are ubiquitous in nature; their high oscillator strength make them useful vibrational probes.[8-13] The variations in the environment surrounding the carbonyl vibrational probes are manifested in the peak positions, width, or lineshape of the carbonyl stretch. Ester group containing the carbonyl moiety occurs in various organic moieties and compounds of biological origin (modified proteins, natural products, lipids) and is commonly used as a site-specific vibrational probe.[9, 13-15] A recent study investigated a change in the lineshape of the ester carbonyl governed by hydrogen bonding with water - a universal hydrogen bonding partner in various biological media.[16-17] Along with water, alcohols are widely used as a cosolvent to study the folding–unfolding mechanism of biomolecules.[18-25] Despite the merit, the effect of hydrogen bonding of carbonyls with alcohols in the spectral lineshapes adds an additional complexity to the problem.[14, 16, 26]

Recently, the multiple well-resolved IR peaks of ester carbonyl in alcohols have been assigned to the non-hydrogen bonded, single hydrogen bonded (1hb), and double hydrogen bonded population (2hb).[16, 26] However, another study speculates about IR peaks arising from the presence of hydrogen bond mediated Fermi resonance (FR) with the ester molecule in its aqueous solution.[27] Lack of a consensus regarding the IR absorption profile in hydrogen bonding environments restricts the use of ester moieties as a site-specific vibrational probe in the hydrogen bonding environment. To verify the aforementioned plausible origins of the IR transitions, molecular level understanding of vibrational frequency position, line shape, and the hydrogen bond interaction of the ester carbonyl group need to be thoroughly explored.

In this work, we have used methyl acetate (MA) and ethyl acetate (EA) as model ester compounds in different alcohols with varying side chains that mimic the hydrogen bonding environment (structures are shown in the Figure 5.1). We have performed FTIR and 2D IR spectroscopies on MA and EA. The IR experiments show three overlapping peaks (~ 1748 cm^{-1}, ~1730 cm^{-1}, ~1711 cm^{-1}) within the broad IR absorption profile (between 1650 cm^{-1} - 1800 cm^{-1}). In this study, the conclusive results obtained from the 2D IR experiments revealed the signatures of both hydrogen bonding and vibrational coupling within the IR lineshapes. Here, we have demonstrated that the lowest frequency peaks (~1711 cm^{-1}) arise from the FR and are not due to a doubly hydrogen bonded population of the ester carbonyls. In addition, the side chain dependent differential solvent exchange dynamics surrounding the ester molecules has also been investigated. This study will be helpful for the unambiguous assignment of multiple peaks from the complex lineshapes of ester in various hydrogen bonding environments.

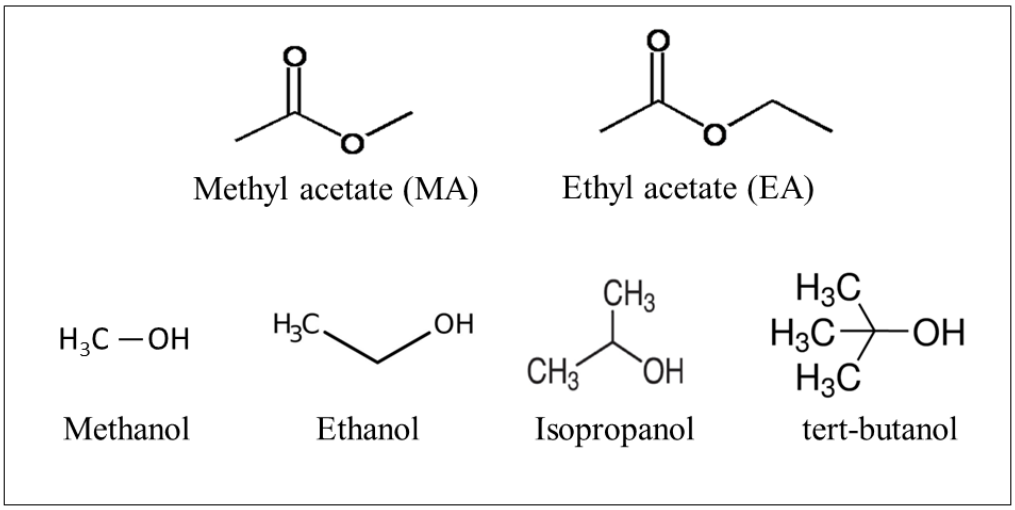

Figure 5.1 The structure of methyl acetate (MA) ad Ethyl acetate (EA). The structures of alcohols used in this study also shown in this figure.

5.2 Materials and sample preparation

Methyl acetate (>99.8%), Methyl acetate (ChCl, >98.9%), Methanol (>99.9%), Ethanol (>99.9%), Isopropanol (>99.9%), and tert-butanol (>99.9%) were purchased from Sigma-Aldrich and used without further purification. Each compound was dissolved independently in different alcohols such that the final concentration of the liquid sample is 0.1M for the IR and 2D IR experiments.

5.3 Results and discussion

The linear IR absorption experiments are performed on the MA and EA in different alcohols of varying side-chains. The representative FTIR spectra are shown in Figure 5.2. The hydrophobicity and bulkiness increase from methanol to t-butanol. Both MA and EA show three well resolved peaks in all alcohols. Upon fitting the IR absorption spectra with three peaks, a monotonic blue shift is observed for the two higher frequency peaks (~1748 cm^{-1} and ~1730 cm^{-1}) from methanol to t-butanol, but the lowest frequency peak (~1711 cm^{-1}) does not show any systematic change with respect to the solvent (Table 5.1). To start with, we consider all possible origins of these multiple peaks. In a previous study, these three peaks have been assigned to the non-hydrogen bonded (~1748 cm^{-1}), hydrogen bonded with a single solvent molecule (1hb, ~1730 cm^{-1}) and hydrogen bonded with two solvent molecules (2hb, ~1711 cm^{-1}). The pictorial representation of different hydrogen bonded populations of the ester with methanol are shown in Figure 5.3a. Now the questions are; 1) does the presence of 1hb and 2hb populations of the ester can provide a significant separation between peaks at (~1730 cm^{-1}) and (~1711 cm^{-1}) that can easily detect by FTIR spectroscopy? 2) Why is the 2hb population (~1711 cm^{-1}) not showing the expected blue shift from methanol to t-butanol?

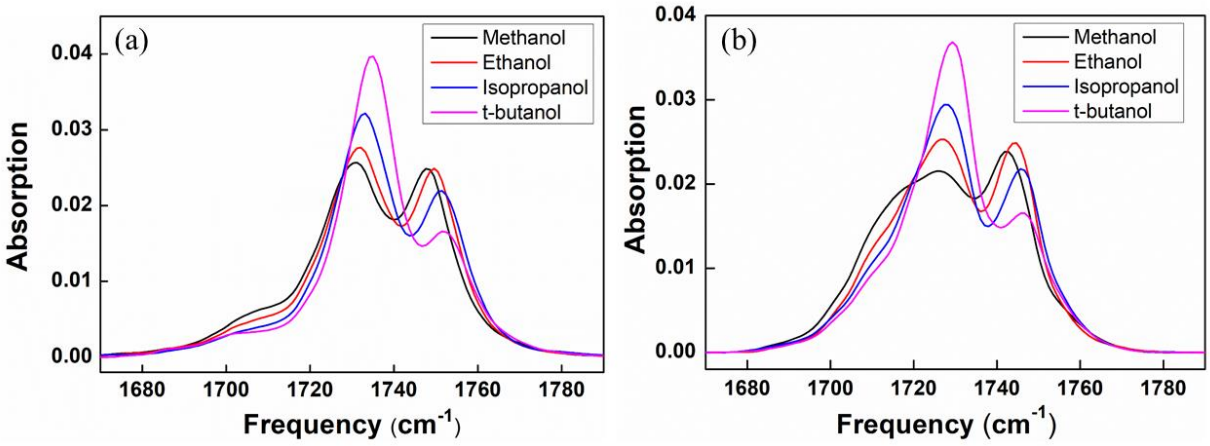

Figure 5.2 a) FTIR spectrum of methyl acetate in different alcohols. b) FTIR spectrum of ethyl acetate in different alcohols.

Table 5.1 FTIR fiited peak frequencies of methyl acetate and ethyl acetate in different alcohols.

Methyl acetate				
	Methanol	Ethanol	Isopropanol	t-butanol
Highest frequency peak	1748.20	1750.06	1752.03	1753.56
Middle peak	1730.30	1731.37	1732.69	1734.51
Lowest frequency peak	1711.52	1711.53	1711.26	1710.27
Ethyl acetate				
Highest frequency peak	1743.02	1744.57	1746.22	1747.03
Middle peak	1726.21	1727.14	1727.74	1728.83
Lowest frequency peak	1711.98	1713.22	1713.16	1713.40

In another study, the FR between the skeletal deformation and the carbonyl stretch has been speculated for the multiple IR lineshape of methyl acetate in water. Fermi resonance occurs when an energy of overtone or a combination band of any particular vibration matches with the fundamental band of another vibration.[28] The transition involved in IR absorption spectroscopy and possible transitions involved in the FR are shown in Figure 5.3b and 5.3c respectively. The decrease in the separation between the absorption frequency of fundamental band and Fermi peak result in the increase in intensity of the less intense Fermi

peak. The intensity borrowing mechanism involved in the FR are shown in Figure 5.3d. The invariability of the peak position with change in solvent and the increase in the intensity of (~1711 cm^{-1}) peaks with the decrease in the separation between (~1711 cm^{-1}) peak and (~1730 cm^{-1}) peak suggest the presence of FR.

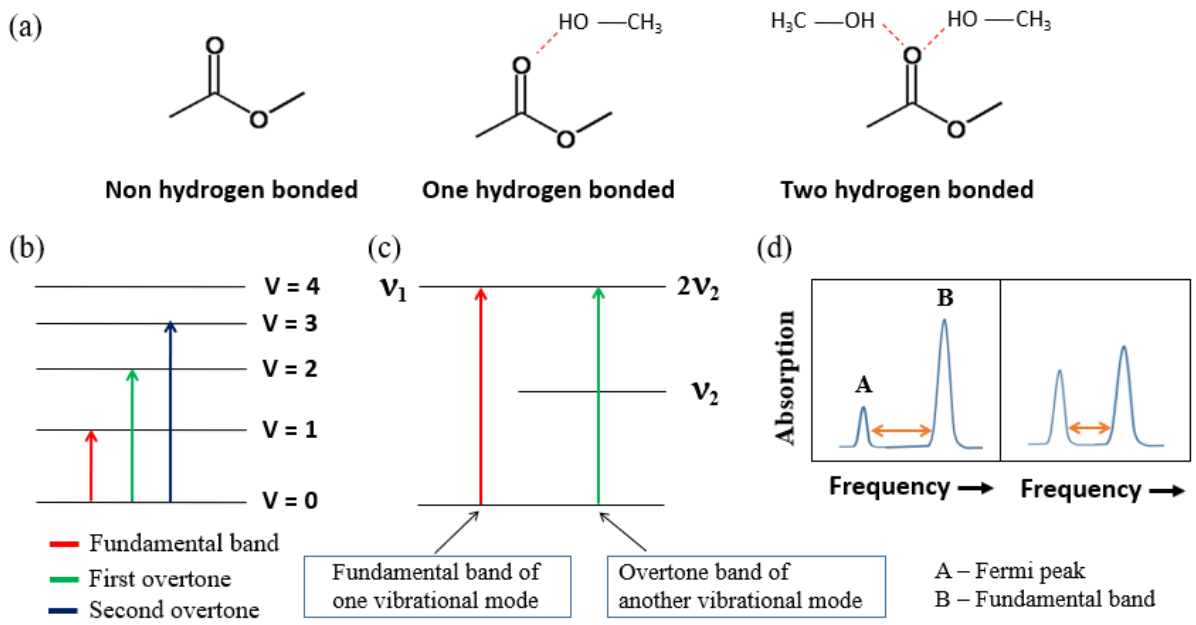

Figure 5.3 a) Schematic representation of different hydrogen bonded populations of methyl acetate in methanol. b) Possible transitions involved in FR are shown in different colors. c) Enegy level diagram for the fundamental and overtone band of two different vibrational modes d) The pictorial representation of intensity borrowing mechanism of FR.

To validate the presence of FR, we have performed 2D IR spectroscopy on the MA and EA in different alcohols. In addition, 2D IR spectroscopy will also allow us to verify the dynamic exchange between multiple hydrogen bonded structures of ester, as speculated in earlier reports. The time and the polarization dependence of the 2D IR cross peaks will allow us to differentiate whether the transitions arise from FR or hydrogen bonded populations. In past decades, 2D IR spectroscopy evolved as a potential tool to measure the ultrafast fluctuations, structural evolution and interchanging dynamics of various chemical and biological systems. The spectral data is plotted in two dimensions which further explores

the vibrational transitions that are difficult to identify with IR absorption spectroscopy. Although 2D IR spectroscopy is akin to 2D NMR, in contrast to 2D NMR, it measures the dynamics at sub-picosecond timescale. 2D IR spectroscopy is a third-order non-linear spectroscopic technique, where three successive femtosecond IR pulses interact with a sample that generates the vibrational echo signal. The 2D IR data is represented as a correlation between the excitation frequency (ω_τ) versus detection frequency (ω_t), which exhibits the vibrational transitions that occur during the coherence and detection period. The ultrafast structural fluctuations of molecules and specific solute-solvent interaction manifest as a change in the peak position and spectral line shapes in 2D IR spectrum.

2D IR experiment involves three time intervals; 1) coherence time (τ) where the molecules labeled with the initial frequency ω_τ 2) population or waiting time (T_w) where ultrafast fluctuation or chemical exchange dynamics happens 3) Detection time (t) where vibrational echo signal emitted with a final frequency ω_t of the labeled molecules. The typical 2D IR spectrum consists of one diagonal peak corresponding to v= 0 – 1 transition (blue peak). Another off-diagonal peak corresponds to v= 1 – 2 transition (red peak), which shifted to lower frequency along the ω_t axis due to the vibrational anharmonicity. The diagonal (v = 0 – 1) peak arises from ground state bleaching and stimulated emission, while off-diagonal (v = 1 – 2) peak coming from excited state absorption. Here, we have only described the specific dynamical processes used in this study (For complete details, refer to section 2.5 of chapter 2).

The chemical exchange process involves the exchange between the population associated with one chemical species with another chemical species during the population period. The evolution of the off-diagonal cross peaks in the 2D IR spectrum as a function of T_w is commonly used as a proxy to the chemical exchange processes. At very short T_w, ~ 0 ps, when the two species are unable to interchange, only two peaks occur along the diagonal.

With the increase in the waiting time, two chemical species interchanging between one another under thermal equilibrium results in the growth of two off-diagonal cross peaks in the 2D IR spectrum. The 2D IR spectrum of MA and EA in different alcohols is shown in Figure 5.4; the corresponding FTIR spectrum is also shown at the top of the 2D IR spectrum. In previous studies[29-30], the vibrational coupling between different modes has been provided a cross peak at zero waiting time. The 2D IR spectrum of MA and EA in all alcohols also shows a off-diagonal cross peaks for the ~1730 cm^{-1} and ~1711 cm^{-1} at T_w=0 ps (Figure 5.4). Due to the low intensity of third peak at ~1711 cm^{-1}, off diagonal cross peaks are not clearly visible in MA but for EA these cross peaks are clearly visible. These direct experimental observations are in contrast to the chemical exchange process between different H-bonded populations, where the cross-peaks typically do not appear at very early waiting times.[31-34] The existence of cross peaks at T_w = 0 ps further supports the assignment of a peak at ~1711 cm^{-1} to FR.

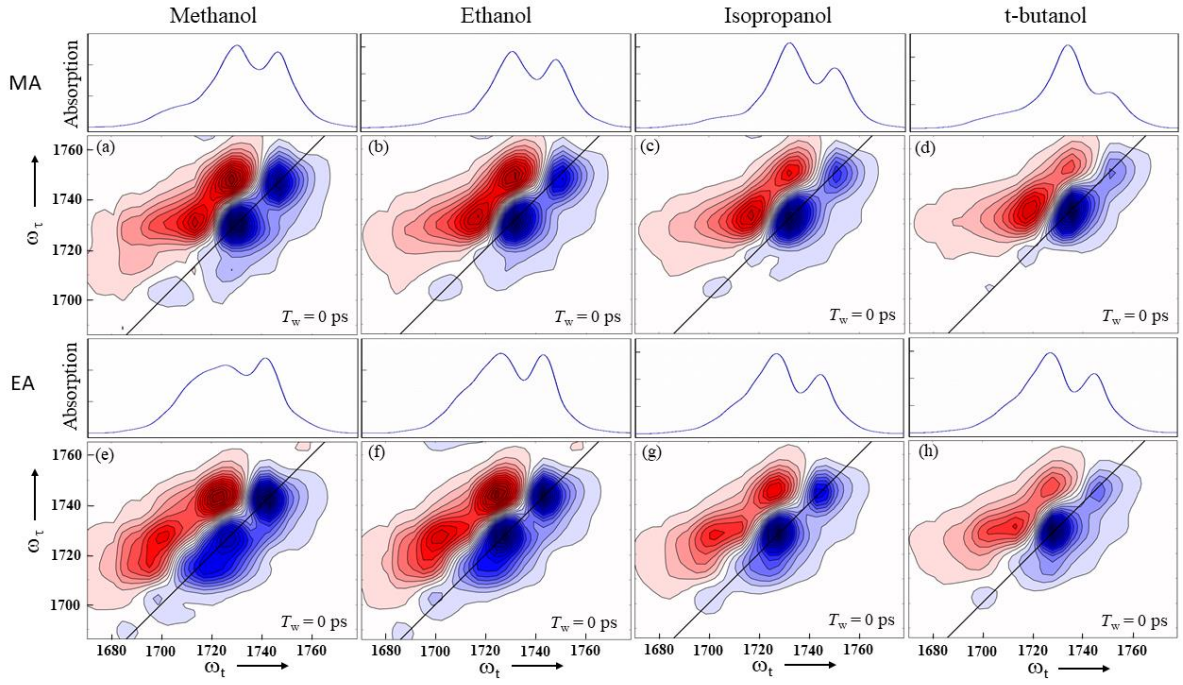

Figure 5.4 The 2D IR spectra of methyl acetate and ethyl acetate in methanol to t-butanol are shown in the figure a-d and e-h respectively. The FTIR spectra in the corresponding alcohol are shown at the top of the 2D IR spectrum.

In figure 5.4, we focused only on the 2D IR spectral signature at T_w=0ps and successfully assigned the peak ~1711 cm^{-1} to FR. But question regarding the previously reported different hydrogen bonded populations of ester molecules still remains unanswered.? In this regard, we have performed 2D IR experiment on MA and EA in all alcohols and looked into the off-diagonal cross peaks between the ~1748 cm^{-1} and ~1730 cm^{-1} as a function of T_w (Figure 5.5 and 5.6). As shown in Figure 5.5 and Figure 5.6, the intensity of cross peak increases from T_w = 0 ps to T_w = 2 ps, which further indicates the exchange between the different hydrogen bonded population occurs at ~1748 cm^{-1} and ~1730 cm^{-1} of ester in different alcohols. The observed spectral characteristics further suggest that the 1hb and 2hb is merged in a broad hydrogen bonded population at ~1730 cm^{-1} and increase in waiting time shows exchange with the non-hydrogen bonded population occurs at ~1748 cm^{-1}.

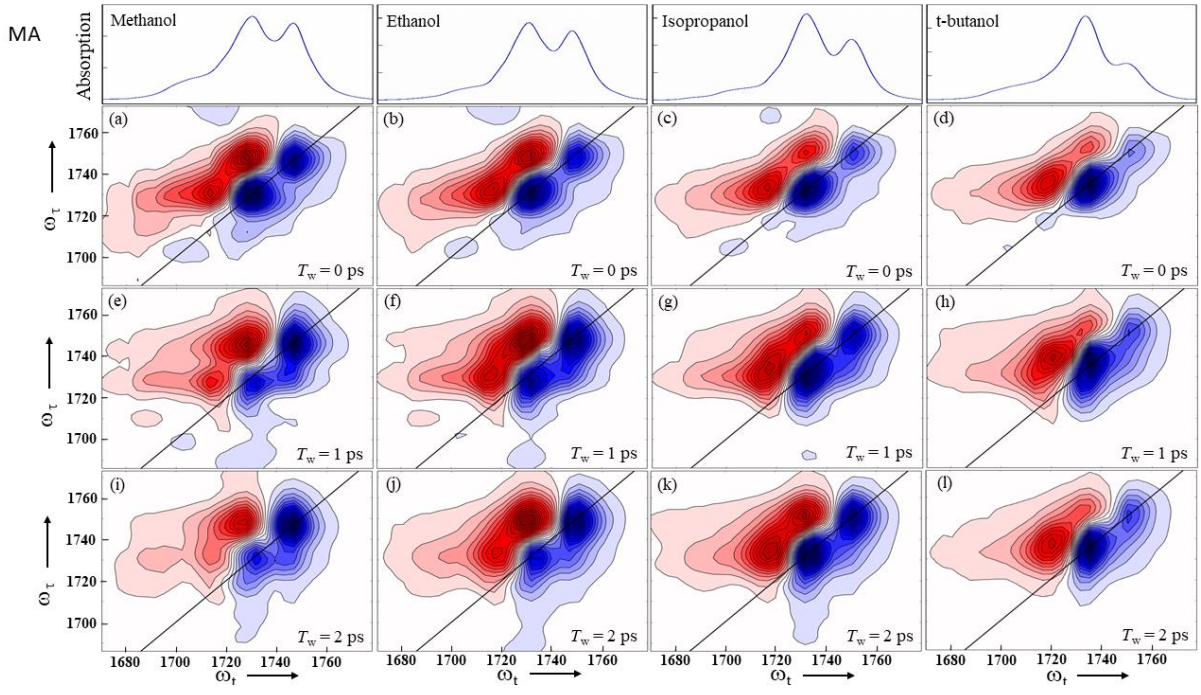

Figure 5.5 Waiting time dependent 2D IR spectrum of methyl acetate in different alcohols.

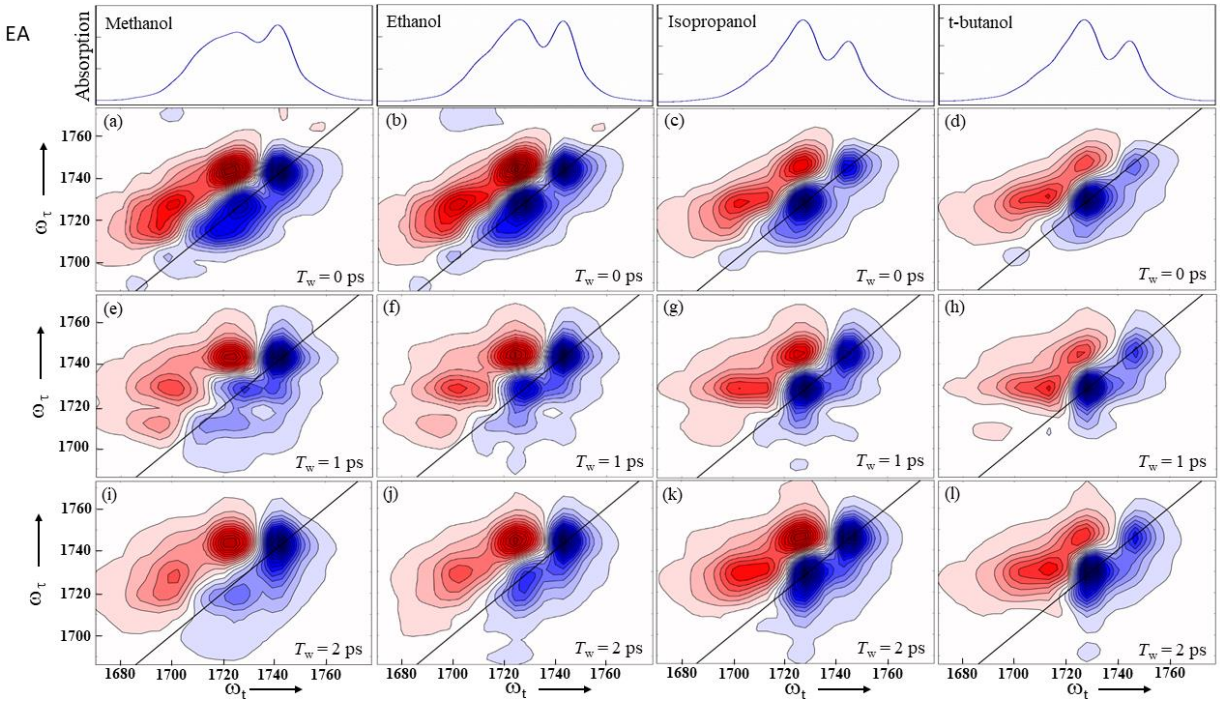

Figure 5.6 Waiting time dependent 2D IR spectrum of ethyl acetate in different alcohols.

Due to the inductive effect, the hydrogen bonding capacity of the hydroxyl group decreases from methanol to t-butanol, so more hydrogen bonded population for the ester is expected in methanol than the t-butanol. In contrast, we have observed an increment in the hydrogen bonded population ranging from methanol to t-butanol. (see T_w = 0 ps in Figure 5.5 and Figure 5.6). This unexpected behavior can be possible due to previously reported ring structure formation in alcohols[35-36] (intermolecular hydrogen bonding between alcohol molecules) which is might be more possible in methanol than the bulky t-butanol. Due to steric effect, instead of forming alcohol-alcohol hydrogen bonding, t-butanol predominantly forms hydrogen bonding with the ester carbonyl which leads to an increase hydrogen bonded population of the ester molecules.

The solvent molecules surrounding the dissolved solute molecules are exchanging in and out from the first solvation shell of the solute.[37] The smaller size of methanol molecules can able to exhibits a faster exchange than the bulkier t-butanol molecules. The faster exchange of methanol molecules can change the proximity of hydrogen bonded partner (hydroxyl

group) surrounds to ester molecules, which can be manifested as a prominent cross peaks at T_w = 2 ps in methanol and not in the t-butanol. (see T_w = 2ps in Figure 5.5 and Figure 5.6). Here, the spectral feature provides qualitative information about the side chain-dependent solvent exchange. We plan to perform the quantitative analysis of the hydrogen bond exchange rate in different alcohol in future work of this study.

5.4 Conclusion

Ester carbonyl groups are ubiquitous in nature and are commonly used as a vibrational probe. The multiple overlapping peaks made it difficult to use ester carbonyl as a site-specific reporter of interaction and dynamics. Previous reports have speculated various peaks involved in the multiple lineshapes for either different hydrogen bonded populations or the Fermi resonance between the skeletal vibration and the carbonyl stretch of ester in protic solvents. The ambiguity in the previous assignment demanded a thorough analysis of the ester molecules in the hydrogen bonding environments. In this study, we have performed FTIR and 2D IR spectroscopy on the methyl acetate and ethyl acetate, which is widely used as a model compound in the ester vibrational study. The results obtained from the FTIR spectroscopy speculates ~ 1711 cm^{-1} due to the presence of FR instead of hydrogen bonded population with two solvent molecules. The FR was further confirmed by monitoring off-diagonal cross peaks at T_w=0 ps between the peaks at ~ 1730 cm^{-1} and ~ 1711 cm^{-1} in the 2D IR spectrum. In addition, the waiting time dependent 2D IR spectroscopic experiments further helped us to assign the non-hydrogen bonded (~ 1748 cm^{-1}) and hydrogen bonded population (~ 1730 cm^{-1}). The effect of a steric factor on the formation of alcohol-alcohol and solute-alcohol hydrogen bonding has also been discussed. The site chain dependent differential exchange of alcohol molecules has also been monitored by using the off-diagonal cross peaks at T_w=2. . These unambiguous peak assignments of ester in alcohols

will be helpful to study the complex biological environment where multiple hydrogen bonding partners might generate complicated lineshapes of ester vibrational probes.

5.5 References

1. Ma, J.; Pazos, I. M.; Zhang, W.; Culik, R. M.; Gai, F., Site-Specific Infrared Probes of Proteins. *Annu Rev Phys Chem* **2015,** *66*, 357-377.

2. Adhikary, R.; Zimmermann, J.; Romesberg, F. E., Transparent Window Vibrational Probes for the Characterization of Proteins With High Structural and Temporal Resolution. *Chem. Rev.* **2017,** *117*, 1927-1969.

3. Kim, H.; Cho, M., Infrared Probes for Studying the Structure and Dynamics of Biomolecules. *Chem. Rev.* **2013,** *113* (8), 5817-5847.

4. Ye, S.; Huber, T.; Vogel, R.; Sakmar, T. P., FTIR analysis of GPCR activation using azido probes. *Nat Chem Biol* **2009,** *5*, 397-399.

5. Taskent-Sezgin, H.; Chung, J.; Banerjee, P. S.; Nagarajan, S.; Dyer, R. B.; Carrico, I.; Raleigh, D. P., Azidohomoalanine: a conformationally sensitive IR probe of protein folding, protein structure, and electrostatics. *Angew Chem Int Ed Engl* **2010,** *49*, 7473-7475.

6. Shrestha, R.; Cardenas, A. E.; Elber, R.; Webb, L. J., Measurement of the Membrane Dipole Electric Field in DMPC Vesicles Using Vibrational Shifts of p-Cyanophenylalanine and Molecular Dynamics Simulations. *J. Phys. Chem. B* **2015,** *119*, 2869-2876.

7. Deb, P.; Haldar, T.; Kashid, S. M.; Banerjee, S.; Chakrabarty, S.; Bagchi, S., Correlating Nitrile IR Frequencies to Local Electrostatics Quantifies Noncovalent Interactions of Peptides and Proteins. *J. Phys. Chem. B* **2016,** *120*, 4034-4046.

8. Fried, S. D.; Bagchi, S.; Boxer, S. G., Measuring Electrostatic Fields in Both Hydrogen-Bonding and Non-Hydrogen-Bonding Environments Using Carbonyl Vibrational Probes. J. Am. Chem. Soc. **2013,** *135*, 11181-11192.

9. Schneider, S. H.; Boxer, S. G., Vibrational Stark Effects of Carbonyl Probes Applied to Reinterpret IR and Raman Data for Enzyme Inhibitors in Terms of Electric Fields at the Active Site. *J. Phys. Chem. B* **2016,** *120*, 9672-9684.

10. Park, E. S.; Boxer, S. G., Origins of the Sensitivity of Molecular Vibrations to Electric Fields: Carbonyl and Nitrosyl Stretches in Model Compounds and Proteins. *J. Phys. Chem. B* **2002,** *106*, 5800-5806.

11. Kurz, L. C.; Drysdale, G. R., Evidence from Fourier transform infrared spectroscopy for polarization of the carbonyl of oxaloacetate in the active site of citrate synthase. *Biochemistry* **1987,** *26*, 2623-7.

12. Tonge, P. J.; Carey, P. R., Length of the acyl carbonyl bond in acyl-serine proteases correlates with reactivity. *Biochemistry* **1990,** *29*, 10723-7.

13. Yu, Y.; Shi, L., Vibrational solvatochromism of the ester carbonyl vibration of PCBM in organic solutions. J. Chem. Phys. **2019,** *151*, 064501.

14. Pazos, I. M.; Ghosh, A.; Tucker, M. J.; Gai, F., Ester carbonyl vibration as a sensitive probe of protein local electric field. *Angew Chem Int Ed Engl* **2014,** *53*, 6080-4.

15. Liu, J.; Huang, X.; Fan, H.; Su, W.; Chen, X.; Zhang, W., Ester-derivatized indoles as sensitive infrared probes for local environment. *Chem. Phys. Lett.* **2020,** *742*, 137139.

16. Banno, M.; Ohta, K.; Tominaga, K., Ultrafast vibrational dynamics and solvation complexes of methyl acetate in methanol studied by sub-picosecond infrared spectroscopy. J. Raman Spectrosc. **2008,** *39* (11), 1531-1537.

17. Candelaresi, M.; Pagliai, M.; Lima, M.; Righini, R., Chemical Equilibrium Probed by Two-Dimensional IR Spectroscopy: Hydrogen Bond Dynamics of Methyl Acetate in Water. *J. Phys. Chem. A* **2009,** *113*, 12783-12790.

18. Kamatari, Y. O.; Konno, T.; Kataoka, M.; Akasaka, K., The methanol-induced transition and the expanded helical conformation in hen lysozyme. *Protein Sci* **1998,** *7*, 681-688.

19. Roccatano, D.; Colombo, G.; Fioroni, M.; Mark, A. E., Mechanism by which 2,2,2-trifluoroethanol/water mixtures stabilize secondary-structure formation in peptides: a molecular dynamics study. *Proc. Natl. Acad. Sci. U. S. A.* **2002,** *99*, 12179-12184.

20. Babu, K. R.; Douglas, D. J., Methanol-Induced Conformations of Myoglobin at pH 4.0. *Biochemistry* **2000,** *39*, 14702-14710.

21. Barteri, M.; Gaudiano, M. C.; Mei, G.; Rosato, N., New stable folding of beta-lactoglobulin induced by 2-propanol. *Biochim Biophys Acta* **1998,** *1383*, 317-26.

22. Kentsis, A.; Sosnick, T. R., Trifluoroethanol Promotes Helix Formation by Destabilizing Backbone Exposure: Desolvation Rather than Native Hydrogen Bonding Defines the Kinetic Pathway of Dimeric Coiled Coil Folding. *Biochemistry* **1998,** *37*, 14613-14622.

23. Cinelli, S.; Onori, G.; Santucci, A., Effect of Aqueous Alcohol Solutions on the Thermal Transition of Lysozyme: A Calorimetric Study. *J. Phys. Chem. B* **1997,** *101*, 8029-8034.

24. Khan, F.; Khan, R. H.; Muzammil, S., Alcohol-induced versus anion-induced states of alpha-chymotrypsinogen A at low pH. *Biochim Biophys Acta* **2000,** *1481*, 229-36.

25. Mukherjee, S.; Deshmukh, A. A.; Mondal, S.; Gopal, B.; Bagchi, B., Destabilization of Insulin Hexamer in Water–Ethanol Binary Mixture. *J. Phys. Chem. B* **2019,** *123*, 10365-10375.

26. Chuntonov, L.; Pazos, I. M.; Ma, J.; Gai, F., Kinetics of Exchange between Zero-, One-, and Two-Hydrogen-Bonded States of Methyl and Ethyl Acetate in Methanol. *J. Phys. Chem. B* **2015,** *119*, 4512-4520.

27. Ghosh, A.; Cohn, B.; Prasad, A. K.; Chuntonov, L., Quantifying conformations of ester vibrational probes with hydrogen-bond-induced Fermi resonances. *J. Chem. Phys.* **2018,** *149*, 184501.

28. Falcke, H.; Eberle, S. H., Raman spectroscopic identification of carbonic acid. *Water Research* **1990,** *24*, 685-688.

29. Tucker, M. J.; Kim, Y. S.; Hochstrasser, R. M., 2D IR photon echo study of the anharmonic coupling in the OCN region of phenyl cyanate. *Chem. phys. lett.* **2009,** *470*, 80-84.

30. Park, J. Y.; Mondal, S.; Kwon, H.-J.; Sahu, P. K.; Han, H.; Kwak, K.; Cho, M., Effect of isotope substitution on the Fermi resonance and vibrational lifetime of unnatural amino acids modified with IR probe: A 2D-IR and pump-probe study of 4-azido-L-phenyl alanine. *J. Chem. Phys.* **2020,** *153*, 164309.

31. Kashid, S. M.; Jin, G. Y.; Bagchi, S.; Kim, Y. S., Cosolvent Effects on Solute–Solvent Hydrogen-Bond Dynamics: Ultrafast 2D IR Investigations. *J. Phys. Chem. B* **2015,** *119*, 15334-15343.

32. Kim, Y. S.; Hochstrasser, R. M., Chemical exchange 2D IR of hydrogen-bond making and breaking. *Proc. Natl. Acad. Sci. U. S. A.* **2005,** *102*, 11185.

33. Zheng, J.; Kwak, K.; Asbury, J.; Chen, X.; Piletic, I. R.; Fayer, M. D., Ultrafast dynamics of solute-solvent complexation observed at thermal equilibrium in real time. *Science* **2005,** *309*, 1338-43.

34. Zheng, J.; Kwak, K.; Chen, X.; Asbury, J. B.; Fayer, M. D., Formation and Dissociation of Intra−Intermolecular Hydrogen-Bonded Solute−Solvent Complexes: Chemical Exchange Two-Dimensional Infrared Vibrational Echo Spectroscopy. *J. Am. Chem. Soc.* **2006,** *128*, 2977-2987.

35. Golub, P.; Doroshenko, I.; Pogorelov, V.; Sablinskas, V.; Balevicius, V.; Ceponkus, J., Temperature Evolution of Cluster Structures in Ethanol. *Dataset Papers in Physics* **2013,** *2013*, 473294.

36. Zoranić, L.; Sokolić, F.; Perera, A., Microstructure of neat alcohols: A molecular dynamics study. *J. Chem. Phys.* **2007,** *127*, 024502.

37. Makarov, V. A.; Feig, M.; Andrews, B. K.; Pettitt, B. M., Diffusion of Solvent around Biomolecular Solutes: A Molecular Dynamics Simulation Study. *Biophysical Journal* **1998,** *75* (1), 150-158.

Chapter 6

Summary and Future Scope

6.1 Summary

Specific and non-specific interactions play key roles in the structure-function relation of molecular system, ranging from small organic molecules to large biomolecules. A comprehensive study of these non-covalent interactions provides information about the protein-ligand interaction and different solute-solvent interactions at a molecular level. Although several spectroscopic techniques are used to quantify various interactions, the macroscopic observables are unable to explore the site-specific changes in the system. In this context, molecular probes have been widely used in many spectroscopic methods due to their high sensitivity to the surrounding environment. The intrinsic vibrational absorbance or fluorescent emission of spectroscopic probes are used to quantify the interaction and dynamics of the system under interest. To widen the application of spectroscopic probes, along with the development of new spectroscopic probes, a complete update on the current molecular probes is highly necessary.

In this thesis, different spectroscopic probes with their specific spectroscopic characteristics and applications have been discussed.

In chapter 3, we have investigated the origin of the dual absorption spectrum of warfarin which is a fluorescent probe and potent anticoagulant drug in biology. Based on the combined experimental and theoretical calculation, we have eliminated the contribution of any structural isomer of warfarin in its dual absorption profile. Furthermore, we have observed that the transition occurs between the two closely spaced occupied molecular orbitals to the lowest unoccupied molecular orbital associated with the coumarin moiety of warfarin. In addition, we have determined that warfarin exists in its open chain deprotonated when it binds to the human serum albumin (HSA).

In chapter 4, the variation of the deep eutectic solvent (DES) nanostructure around the dissolved solute upon addition of water is investigated by polarization-selective two-dimensional infrared spectroscopy and molecular dynamics simulations. The ammonium thiocyanate (NH_4SCN) is used as a vibrational probe for this purpose. In this study, we have investigated a solute perspective transition of deep eutectic solvation environment to an aqueous solution which is lower than the previously reported for the "water in DES" to "DES in water" transition.

In chapter 5, the origin of the spectral line shape of the ester compounds in protic solvents is investigated by using linear and 2D IR spectroscopy. The results obtained from the IR and 2D IR experiment indicate that the hydrogen bond induced fermi resonance is the plausible origin of the additional line shape. The different hydrogen bonded populations and differential solvent dynamics around the solute also have been discussed.

6.2 Future scope

6.2.1 Determination of local electric field of warfarin binding site in human serum albumin.

Carbonyl (C=O) groups are present in different drugs, proteins and other biomolecules. Due to its high extinction coefficient, C=O stretching mode is commonly used as a vibrational (IR) probe.[1-3] A change in the environment surrounding the probe modulates the electric field exerted on the IR probe, causing a shift in the vibrational frequency. Furthermore, the vibrational frequencies of C=O groups are linearly sensitive towards the electrostatic field through the vibrational Stark effect (VSE) (Figure 6.1a).[1, 4-5] X-ray crystal structures indicate that the warfarin binds to Sudlow site I of the human serum albumin (HSA) mainly through its coumarin moiety.[6] To understand the warfarin-HSA binding, it is essential to estimate the electric field exerted by the active site onto the warfarin. This can be achieved

by using 4-hydroxycoumarin (4-HC, structure is shown in Figure 6.1b) as a model vibrational probe that will mimic the coumarin moiety of warfarin. The linear sensitivity between ester carbonyl stretching frequency of 4HC and the calculated electric field in the different solvents of varying polarity can be used as a calibration line to predict the electric field exerted on the warfarin in the warfarin-HSA complex. This field-frequency approach will be helpful to understand the electrostatic environment surrounding the various drugs that specifically bind to the Sudlow site I of HSA.

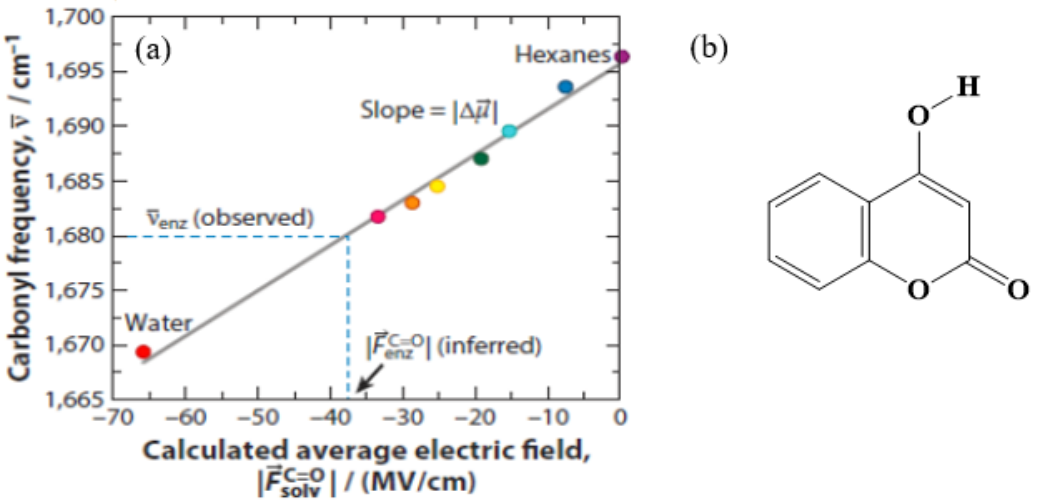

Figure 6.1 (a) The plot of carbonyl stretching frequency against calculated average electric field.(*Annu. Rev. Biochem.* **2017,** *86,* 387-415) (b) Structure of 4-hydroxycoumarin (4-HC).

6.2.2 Estimation of electric field and hydrogen bonding status of hydrophobic DES using nitrile as a vibrational probe.

In the case of deep eutectic solvent (DES), hydrophilic DES gain significant attention than its hydrophobic counterparts. In 2015, Van Osch and co-workers prepared the first hydrophobic DES (HDES) by mixing a different hydrogen bond donor (HBD) and hydrogen bond acceptor (HBA) at a specific molar ratio.[7] HBD and HBA are environmentally benign compounds which qualitatively makes HDES a suitable choice for a green solvent media in

various applications. Prior to use of HDES in different application in the presence of solute, the detailed knowledge about local solvation structures of HDES around a solute need to be explored. HDES mainly formed a biphasic mixture with the aqueous solution,[8] but a small amount of water is miscible in the HDES which can change the microscopic solvation of HDES surrounds to the dissolved solute. Water can act as another hydrogen bond donor in the HDES-water mixture. From the application perspective, it is important to quantify the hydrogen bonding interaction and change in the electrostatic environment around the solute as a function of the addition of water. In this work, we will use benzonitrile as a vibrational probe. The solvatochromism of benzonitrile shows a V-shaped field-frequency plot as shown in Figure 6.2.[9] To investigate the hydrogen bonding status and electrostatic environment of HDES, the field versus frequency calibration plot of benzonitrile dissolved in different solvents can be utilized. The nitrile stretch of benzonitrile will work as the vibrational probe. This work will be helpful to identify the solute perspective extent of hydration and change in the local environment surrounds the dissolved solute.

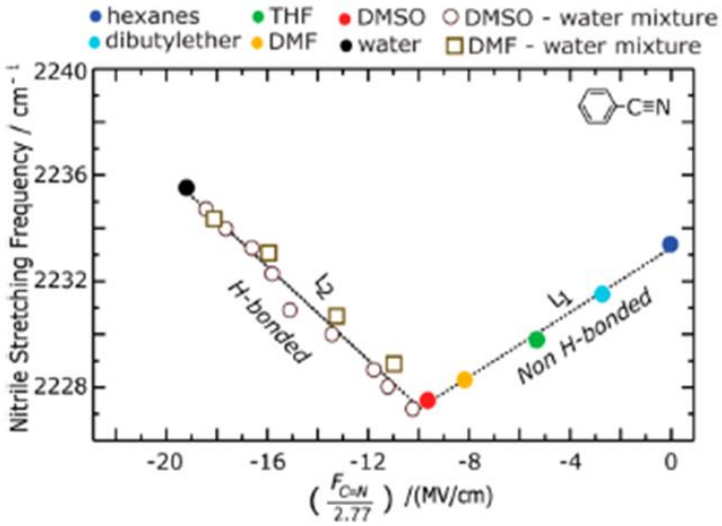

Figure 6.2 The plot of nitrile stretching frequency of benzonitrile versus the calculated electric field from MD simulation.(*J. Phys. Chem. B* **2016**, 120, 17, 4034–4046)

6.2.3 Study of drugs passage thorough the bilayer system – differential hydrogen bonding approach using PCT and PCM as vibrational probes.

Intermolecular and intramolecular hydrogen bonding associated with the drug molecules plays a vital role in passive diffusion of drugs across cell membranes. Recently, the effect of intramolecular hydrogen bonding (IMHB) on the penetration of a drug molecule through a lipid membrane has been studied by using a molecular dynamics simulation.[10] The previous results indicate that the intramolecular hydrogen bond (IMHB) favors the permeability of the drug molecule in the hydrophobic core of the lipid bilayer.[10] In contrast, the polar group of the drugs decreases this affinity towards the lipophilic part. The interaction between the drug and its surrounding environments needs to be investigated to understand the specific bioactivity. In this work, we will use 2-oxo-1-pyrrolidine acetamide (PCT) which can form both intra and intermolecular hydrogen bonding. In addition, we will synthesize 3-oxo-1-pyrrolidine acetamide (PCM), which is unable to form intramolecular hydrogen bonding. The structures of PCT and PCM are shown in Figure 6.3. In this work, we will use the linear and two-dimensional IR (2D IR) spectroscopic method combined with MD simulation to measure the interactions and dynamics of drugs during their diffusion through the lipid bilayer.

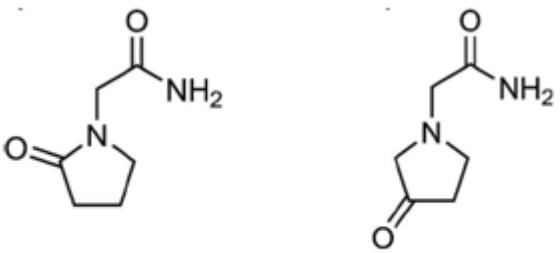

PCT **PCM**

Figure 6.3 The structure of 2-oxo-1-pyrrolidine acetamide (PCT) and 3-oxo-1-pyrrolidine acetamide (PCM).

6.3. References

1. Fried, S. D.; Bagchi, S.; Boxer, S. G., Measuring Electrostatic Fields in Both Hydrogen-Bonding and Non-Hydrogen-Bonding Environments Using Carbonyl Vibrational Probes. *J. Am. Chem. Soc.* **2013,** *135*, 11181-11192.

2. Kashid, S. M.; Bagchi, S., Experimental Determination of the Electrostatic Nature of Carbonyl Hydrogen-Bonding Interactions Using IR-NMR Correlations. *J. Phys. Chem. Lett.* **2014,** *5*, 3211-3215.

3. Haldar, T.; Kashid, S. M.; Deb, P.; Kesh, S.; Bagchi, S., Pick and Choose the Spectroscopic Method to Calibrate the Local Electric Field inside Proteins. *J. Phys. Chem. Lett.* **2016,** *7*, 2456-2460.

4. Fried, S. D.; Bagchi, S.; Boxer, S. G., Extreme electric fields power catalysis in the active site of ketosteroid isomerase. *Science* **2014,** *346*, 1510-1514.

5. Fried, S. D.; Boxer, S. G., Measuring Electric Fields and Noncovalent Interactions Using the Vibrational Stark Effect. *Acc. Chem. Res.* **2015,** *48*, 998-1006.

6. Petitpas, I.; Bhattacharya, A. A.; Twine, S.; East, M.; Curry, S., Crystal structure analysis of warfarin binding to human serum albumin: anatomy of drug site I. *J. Biol. Chem.* **2001,** *276*, 22804-22809.

7. van Osch, D. J. G. P.; Zubeir, L. F.; van den Bruinhorst, A.; Rocha, M. A. A.; Kroon, M. C., Hydrophobic deep eutectic solvents as water-immiscible extractants. *Green Chemistry* **2015,** *17*, 4518-4521.

8. Martins, M. A. R.; Crespo, E. A.; Pontes, P. V. A.; Silva, L. P.; Bülow, M.; Maximo, G. J.; Batista, E. A. C.; Held, C.; Pinho, S. P.; Coutinho, J. A. P., Tunable Hydrophobic Eutectic Solvents Based on Terpenes and Monocarboxylic Acids. *ACS Sustain. Chem. Eng.* **2018,** *6*, 8836-8846.

9. Deb, P.; Haldar, T.; Kashid, S. M.; Banerjee, S.; Chakrabarty, S.; Bagchi, S., Correlating Nitrile IR Frequencies to Local Electrostatics Quantifies Noncovalent Interactions of Peptides and Proteins. *J. Phys. Chem. B* **2016,** *120*, 4034-4046.

10. Coimbra, J. T. S.; Feghali, R.; Ribeiro, R. P.; Ramos, M. J.; Fernandes, P. A., The importance of intramolecular hydrogen bonds on the translocation of the small drug piracetam through a lipid bilayer. *RSC Adv.* **2021,** *11*, 899-908.

ABSTRACT

Name of the Student: Sushil Suresh Sakpal **Registration No**.:10CC16A26019

Faculty of Study: Chemical Science **Year of Submission**: 2021

AcSIR academic centre/CSIR Lab: CSIR-National Chemical Laboratory, Pune

Name of the Supervisor: Dr. Sayan Bagchi

Title of the thesis: Spectroscopic Investigation of Molecular Probes.

Molecular probes are spectroscopic reporters of interactions. As the interactions are transient, these probes also provide dynamical information. As both interactions and dynamics are key structure-function relation, the probes contribute to the understanding of the system's behaviour. Molecular probes provide either the global or the local structural and dynamical information at different length scales. For example, the fluorescent probes provide local information, but fails to furnish bond-specific details. On the other hand, the vibrational probes provides the bond-specific local information. This thesis includes spectroscopic responses from a variety of molecular probes in small molecules and proteins. The use of just one spectroscopic technique at times fails to provide an unambiguous understanding of the system. It has been shown here that a combination of spectroscopic techniques, used in tandem with theoretical calculations, leads to a conclusive understanding. From a dynamical viewpoint, the solute's reorientation and the solvent's fluctuation can contribute to the frequency evolution of the system. Polarization dependence of the time-resolved information decouples the motions. Time-resolved vibrational spectroscopy can differentiate the coupled vibrations from conformational interconversion. In a nutshell, this thesis provides a detailed report on the subtle manoeuvres in different spectroscopic techniques using various molecular probes to overcome the ambiguity in our fundamental understanding of the molecular systems.

List of Publication(s) in SCI Journal(s) Emanating from the Thesis Work

1) **Sakpal, S. S**.; Ghosh, D.; Manae, M. A.; Hazra, A.; Bagchi, S. The Curious Case of Aqueous Warfarin: Structural Isomers or Distinct Excited States? *J. Phys. Chem. B, 125, 11, 2871-78 (2021)*
2) **Sakpal, S. S**.; Deshmukh, S. H.; Chaterjee, S.; Ghosh, D.; Bagchi, S.; Transition of a Deep Eutectic Solution to Aqueous Solution: A Dynamical Perspective of the Dissolved Solute. J. Phys. Chem. Lett. 2021, 12, 8784–8789

List of Publications Non-Emanating from the Thesis Work

1) Chatterjee, S.; Ghosh, D.; Haldar, T.; Deb, P.; **Sakpal, S. S**.; Deshmukh, S. H.; Kashid, S. M.; Bagchi, S.; Hydrocarbon Chain-Length Dependence of Solvation Dynamics in Alcohol-Based Deep Eutectic Solvents: A Two-Dimensional Infrared Spectroscopic Investigation, J. Phys. Chem. B, 123, 44, 9355–9 (2019).
2) Ghosh, D.; Deshmukh, S. H.; Chatterjee, S.; **Sakpal, S. S**.; Haldar, T.; Dhakad, A.; Kashid, S. M.; Bagchi, S.; Two Dimensional Infrared Spectroscopy: A Structure Sensitive Technique with Ultrafast Time Resolution, Modern techniques of spectroscopy pp 39-56 (2021)
3) Rai D. K. J; Sahariah, B.; **Sakpal, S. S**.; Bar, K. A.; Bagchi, S.; and Sarma, B. K.; Evidence of an n_N(amide) $\rightarrow \pi^*_{Ar}$ Interaction in N-Alkyl-N,N′-diacylhydrazines, Org. Lett. (2021)
4) Baruah, K.; Sahariah, B.; **Sakpal, S. S**.; Rai D. K. J; Bar, K. A.; Bagchi, S.;, and Sarma, B. K.; Stabilization of Azapeptides by $N_{amide}\cdots H–N_{amide}$ Hydrogen Bonds. Org. Lett., 23, 13, 4949–4954 (2021)

List of papers with abstract presented (oral or poster) at national or international conferences/seminars.

1) **"Science Day Celebration 2020"** held at CSIR National Chemical laboratory Pune. (Presented poster)
2) **"Ultrafast Sciences (UFS) 2019"** organized by IIT Bombay, Mumbai, India. (Presented poster)

THE JOURNAL OF PHYSICAL CHEMISTRY B
A JOURNAL OF THE AMERICAN CHEMICAL SOCIETY

pubs.acs.org/JPCB

Article

The Curious Case of Aqueous Warfarin: Structural Isomers or Distinct Excited States?

Sushil S. Sakpal,[#] Deborin Ghosh,[#] Meghna A. Manae, Anirban Hazra,* and Sayan Bagchi*

Cite This: *J. Phys. Chem. B* 2021, 125, 2871−2878

Read Online

ACCESS | Metrics & More | Article Recommendations | Supporting Information

ABSTRACT: Warfarin is a potent anti-coagulant drug and is on the World Health Organization's List of Essential Medicines. Additionally, it displays fluorescence enhancement upon binding to human serum albumin, making warfarin a prototype fluorescent probe in biology. Despite its biological significance, the current structural assignment of warfarin in aqueous solution is based on indirect evidence in organic solvents. Warfarin is known to exist in different isomeric forms—open-chain, hemiketal, and anionic forms—based on the solvent and pH. Moreover, warfarin displays a dual absorption feature in several solvents, which has been employed to study the ring-chain isomerism between its open-chain and hemiketal isomers. In this study, our pH-dependent experiments on warfarin and structurally constrained warfarin derivatives in aqueous solution demonstrate that the structural assignment of warfarin solely on the basis of its absorption spectrum is erroneous. Using a combination of steady-state and time-resolved spectroscopic experiments, along with quantum chemical calculations, we assign the observed dual absorption to two distinct $\pi \rightarrow \pi^*$ transitions in the 4-hydroxycoumarin moiety of warfarin. Furthermore, we unambiguously identify the isomeric form of warfarin that binds to human serum albumin in aqueous buffer.

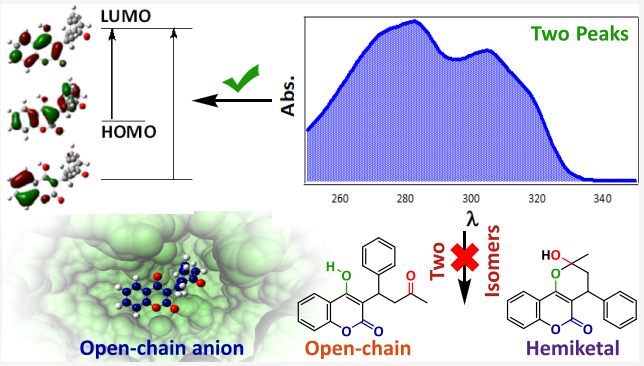

INTRODUCTION

Coumarin derivatives are of significant interest due to their pharmaceutical importance as well as their fluorescent properties. Warfarin, a coumarin derivative of clinical significance, is a highly potent anti-coagulant drug that reduces the risk of strokes and heart attacks by preventing blood clots in veins.[1−3] Moreover, warfarin binds to human serum albumin (HSA),[4] the most abundant protein in blood plasma that transports hormones, fatty acids, bilirubin, and drugs in the human body.[5,6] The high affinity and selectivity of warfarin toward HSA and the substantial increase in its fluorescence upon binding to the protein make warfarin a prototype fluorescent probe in biology.[7] Fluorescence lifetimes of warfarin in aqueous solution, free or bound to blood plasma proteins, have been correlated to blood coagulation.[8] Interestingly, warfarin is known to exist in various isomeric forms.[9−12] The conjugation between the functional groups gives rise to the coumarin and the chromone structures in various solvents (Figure 1).[13,14] Moreover, proximity of the hydroxyl and the carbonyl moieties allows open-chain and cyclic hemiketal conformations, leading to four possible isomers of warfarin. In addition, the deprotonated forms (anion) also contribute to the structural diversity of warfarin in water. Therefore, the structural determination of warfarin in water is important from the perspective of biological applications.[15]

Surprisingly, the current structural interpretation of warfarin in aqueous solution is based on indirect spectroscopic evidence in non-aqueous solvents. Nuclear magnetic resonance (NMR) studies in different organic solvents have indicated the predominance of the coumarin structural form over chromone.[13,16,17] In addition, the coexistence of hemiketal and open-chain isomeric forms has been suggested from NMR peak positions.[16−18] However, the structural details of warfarin in an aqueous medium are unavailable from NMR due to the low solubility of warfarin in water. More recently, absorption spectroscopy in organic solvents and in solvent mixtures has been employed in lieu of NMR to identify the warfarin isomers. The warfarin absorption spectrum consists of two overlapping peaks in the 250−350 nm range, which have been assigned to the hemiketal (~280 nm) and the open chain isomers (~310 nm).[19] Although the absorption experiments were not performed in an aqueous solution, several structural studies on the ring-chain isomerism as well as various biological applications of warfarin have used these absorption

Received: December 3, 2020
Revised: February 18, 2021
Published: March 17, 2021

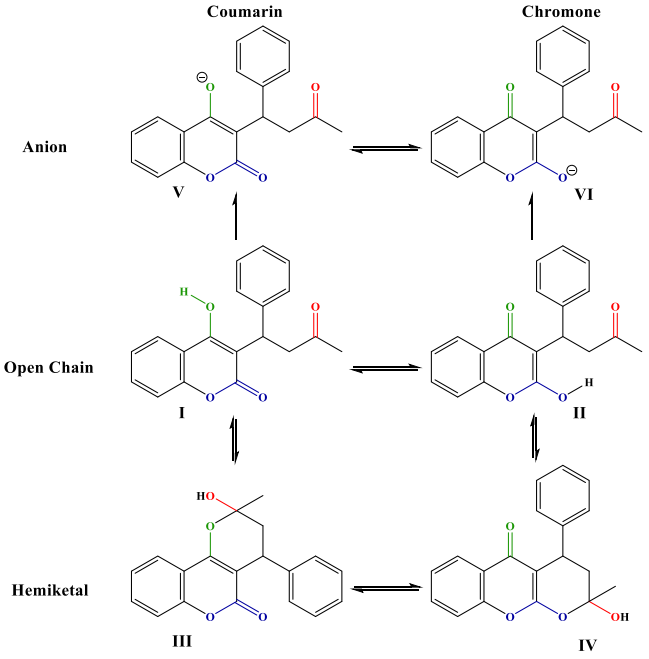

Figure 1. Possible isomers of warfarin: (**I**) coumarin open chain, (**II**) chromone open chain, (**III**) coumarin hemiketal, (**IV**) chromone hemiketal, (**V**) coumarin anionic, and (**VI**) chromone anionic. The hydroxyl, ketone, and ester functional groups are shown in green, red, and blue, respectively.

spectrum-based structural interpretations.[10,11,20−27] The interpretation gets even more ambiguous with another recent study suggesting that these two absorption peaks of warfarin arise not from the different isomeric forms but from $n \rightarrow \pi^*$ and $\pi \rightarrow \pi^*$ transitions.[23] The biological significance of warfarin and the existence of several coumarin-based drug molecules demand an unambiguous structural assignment in the aqueous medium.

In this report, we investigate the origin of the dual absorption of warfarin in aqueous solution using a combination of time-averaged and time-resolved spectroscopic experiments and quantum mechanical calculations. Absorption and emission experiments on warfarin in aqueous solutions at different pH values are performed. In addition, experiments are performed on warfarin derivatives with structural constraints such that only one of the isomeric forms is available for warfarin. Interestingly, we observe a similar dual absorption pattern for both the structurally constrained warfarin derivatives, irrespective of being restricted to one particular isomer. These results demonstrate that the lower and the higher wavelength transitions in the absorption spectrum of warfarin do not arise from two different structural isomers. This is further corroborated by steady-state emission spectroscopy. Our results show that the ring-chain isomerism of molecules structurally related to warfarin cannot be explained using the relative populations of the two absorption bands as they have been done in the past. Further, our results also show that the dual absorption is due to two distinct $\pi \rightarrow \pi^*$ transitions of warfarin. Quantum chemical calculations indicate that the dual absorption band arises due to distinct transitions to accessible excited states. The transitions take place from two energetically close occupied molecular orbitals (MOs) to the lowest unoccupied molecular orbital (LUMO) pertaining to the coumarin moiety of warfarin. Time-resolved emission spectroscopy on coumarin derivatives confirms that warfarin exists in its anionic form in water at a pH greater than 6.0. Further, experiments are performed in the presence of HSA to identify the isomer of warfarin that binds to the blood plasma protein in aqueous buffer. Our results reveal that warfarin adopts an open-chain anionic form when bound to HSA, independent of the pH of the aqueous buffer.

MATERIALS AND METHODS

Chemicals. Warfarin (analytical standard), 4-hydroxycoumarin (98%), pyranocoumarin (analytical standard), and HSA were purchased from Sigma-Aldrich, and their purity was checked using the high-performance liquid chromatography−mass spectrometry (HPLC-MS) technique. Methoxywarfarin and 4-methoxycoumarin were synthesized using the normal methylation method, and purity of the synthesized compounds was checked by NMR spectroscopy and the HPLC-MS technique.[28] All solvents were of spectroscopy grade (Sigma-Aldrich).

Spectroscopic Experiments. Absorption and fluorescence spectra were measured in a Shimadzu UV−vis−NIR (360$^+$) spectrophotometer and a PTI Quanta Master steady-state spectrofluorometer, respectively. A quartz cell of a 1 cm path length was used as the sample chamber. Freshly prepared ∼60 μM solutions of warfarin and its related compounds were used for this purpose. Picosecond fluorescence dynamics studies of the fluorophore solutions were performed with a time-correlated single-photon counting (TCSPC) system employing a picosecond laser operating with λ_{ex} = 310 nm and a pulse width of ∼50 ps.

Quantum Chemical Calculations. Geometries of 4-hydroxycoumarin, 4-methoxycoumarin, and different isomeric forms of warfarin were optimized using density functional theory (DFT) with the hybrid functional B3LYP[29,30] and the 6-31+G(d,p) basis set. The effect of the solvent was incorporated during geometry optimization using the SMD solvation model.[31] The calculation of transition energies and oscillator strengths of the higher singlet excited states were performed using time-dependent density functional theory (TDDFT) with the same functional and basis set. It was shown that transition energies calculated by the TDDFT method matched well with experimental values for coumarin derivatives.[32−35] Molecular orbital diagrams of all possible forms of every compound were computed at the Hartree−Fock (HF) level of theory with the 6-31+G(d,p) basis set. The equation-of-motion coupled-cluster singles and doubles (EOM-CCSD) method, with the same 6-31+G(d,p) basis set, was used to calculate accurate oscillator strengths of isolated 4-methoxycoumarin. The DFT, TDDFT, and HF calculations were performed using the Gaussian 09 program,[36] and the EOM-CCSD calculations were carried out using Molpro 2012.[37,38]

RESULTS AND DISCUSSION

The ground-state structures of different isomeric forms of warfarin in water are optimized using DFT (Table 1). We consider every possible structural conformer of warfarin to remove any bias reported in previous studies. The open-chain and the cyclic hemiketal coumarin structures (**I** and **III**) are found to be more stable than the corresponding chromone structures (**II** and **IV**). Moreover, in the case of any equilibrium between **I** and **III**, the equilibrium is expected to shift toward the lower energy hemiketal isomer. Estimation of

https://doi.org/10.1021/acs.jpcb.0c10824
J. Phys. Chem. B 2021, 125, 2871−2878

Table 1. Calculated Spectral Parameters for $S_0 \rightarrow S_1$ Electronic Transitions of Various Forms of Warfarin in Water (SMD Solvation Model) Using DFT and TDDFT B3LYP/6-31+G(d,p)

	open chain		hemiketal		anion
structure	I	II	III	IV	(V/VI)[a]
relative ground-state energy (kcal/mol)	3.6	10.6	0.0	8.0	288.4
absorption λ_{max} (nm)	316.7	309.7	303.1	309.7	319.3
oscillator strength (f)	0.56	0.03	0.66	0.04	0.44

[a]See the Supporting Information for details.

the $S_0 \rightarrow S_1$ transition wavelengths and the corresponding oscillator strengths further suggests that the chromone conformers are not only energetically unfavorable but also would not contribute to the absorption spectrum of warfarin. The structures **V** and **VI** corresponding to the warfarin anion are merely resonance structures, and thus, a single species of the deprotonated form of warfarin is present in solution at higher pH.

Absorption spectra of warfarin in aqueous solution show two distinct absorption peaks centered at ∼280 and ∼310 nm at lower pH (Figure 2a). An increase in the pH results in the decrease in the absorbance of the ∼280 nm peak along with a concomitant increase in the absorbance of the ∼310 nm peak.

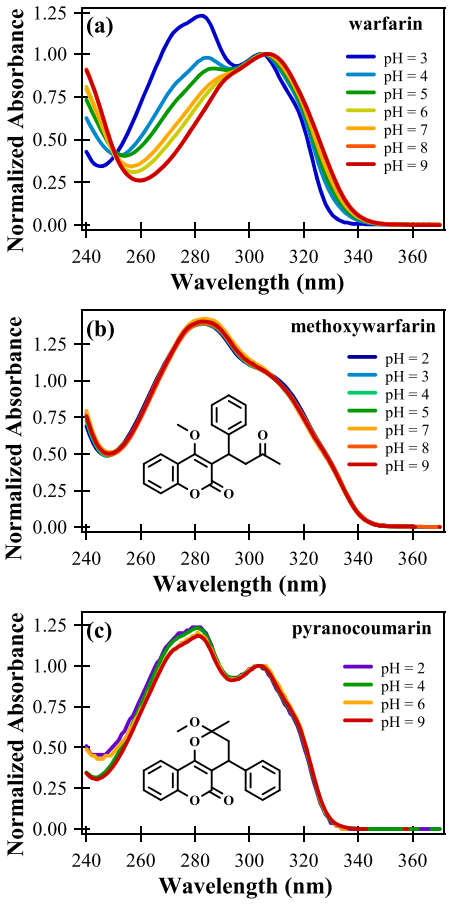

Figure 2. Normalized (at 310 nm) absorption spectra of (a) warfarin, (b) methoxywarfarin, and (c) pyranocoumarin in aqueous solution of different pH. The structures of methoxywarfarin and pyranocoumarin are shown along with the spectra.

Moreover, a small red shift is observed in the band at ∼310 nm for pH values greater than 5. On the basis of previous structural assignments (Figure S1 in the Supporting Information), the dual absorption pattern in water can be speculated to arise from the open chain (∼310 nm) and the hemiketal isomers (∼280 nm).[19,20] Although this speculation may appear qualitatively consistent with our calculated wavelengths, confounding results are obtained when control experiments are performed on structurally constrained warfarin derivatives.

Two structurally constrained warfarin derivatives, methoxywarfarin and pyranocoumarin (structures in Figure 2b and Figure 2c, respectively), are chosen, which by virtue of their structures, are restricted to exclusively open-chain and hemiketal conformers, respectively. Surprisingly, similar to warfarin, both methoxywarfarin and pyranocoumarin have dual absorptions at ∼280 and ∼310 nm (Figure 2b and Figure 2c, respectively), irrespective of their confinement to one specific isomeric form. However, unlike warfarin, the absorption spectra of methoxywarfarin and pyranocoumarin do not show any pH dependence. The inability of methoxywarfarin and pyranocoumarin to convert to the anionic form is the likely explanation for the invariance of the absorption spectra with changing pH. As the stability of pyranocoumarin may be debatable in acidic solution (see the Supporting Information for details), absorption experiments are further performed in non-aqueous solvents to confirm the dual absorption pattern of pyranocoumarin (Figure S2 in the Supporting Information). These observations in structurally constrained warfarin derivatives are in conflict with the earlier structural assignments of warfarin on the sole basis of the absorption spectrum.[19] This gives rise to the following question: what then is the origin of the two bands?

A recent report has mentioned that the dual absorption of warfarin arises from $n \rightarrow \pi^*$ and $\pi \rightarrow \pi^*$ transitions.[23] As a single carbon−carbon bond fission of warfarin results in 4-hydroxycoumarin and phenylbutanone (structures are shown in Figure 3a) without any change in the conjugation length, the absorption spectrum of warfarin can be considered to be a combination of the absorption spectra of the two moieties. Negligible absorption due to the $n \rightarrow \pi^*$ transition of the keto-carbonyl group at ∼260 nm is observed for phenylbutanone (Figure 3a). The absorption spectrum of 4-hydroxycoumarin (Figure 3a,b) shows similar spectral signatures and pH dependence as that of warfarin. pH-independent dual absorption of 4-methoxycoumarin (Figure 3c), similar to that of 4-methoxywarfarin, further suggests that the single absorption band at higher pH in both warfarin and 4-hydroxycoumarin (pK_a of 4.1)[15] arises due to the anionic species. More importantly, both the transition frequency and the weak intensity of the $n \rightarrow \pi^*$ absorption in phenylbutanone suggest that the $n \rightarrow \pi^*$ transition does not contribute to the dual absorption of warfarin. These results clearly indicate that the 4-hydroxycoumarin moiety of warfarin is solely responsible for the dual absorption pattern. This is a significant conclusion, although the assignment of the two bands still remains unresolved.

In a previous report on coumarin, the dual absorption was hypothesized to arise from HOMO → LUMO and HOMO-1 → LUMO transitions.[39,40] As our results suggest that the dual absorption profile of warfarin arises exclusively from the 4-hydroxycoumarin moiety, TDDFT calculations are performed for all possible Franck−Condon transitions on the optimized

https://doi.org/10.1021/acs.jpcb.0c10824
J. Phys. Chem. B 2021, 125, 2871−2878

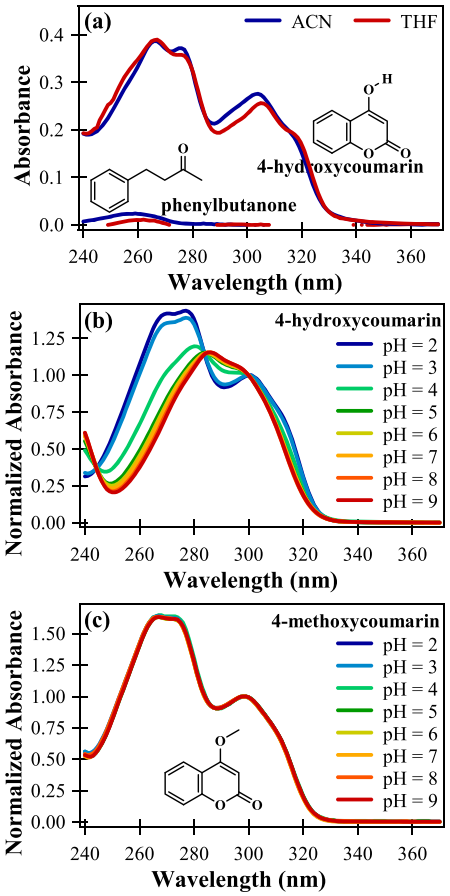

Figure 3. Absorption spectra of (a) phenylbutanone and 4-hydroxycoumarin in ACN and THF; normalized absorption spectra of (b) 4-hydroxycoumarin and (c) 4-methoxycoumarin in aqueous solutions of different pH. The structures of phenylbutanone, 4-hydroxycoumarin, and 4-methoxycoumarin are shown along with the spectra.

geometries of 4-hydroxycoumarin (neutral and anionic), 4-methoxycoumarin, and warfarin (all coumarin-type isomers). The HF molecular orbitals (MOs) are also computed. Schematic representations of all possible transitions in 4-hydroxycoumarin, its anion and 4-methoxycoumarin (within 260−340 nm), the corresponding oscillator strengths (f), and the MOs are shown in Figure 4a−c and Figure S3a−c (see the Supporting Information). Additional schematic representations from similar calculations on different coumarin-type isomers of warfarin in the range of experimental absorption are shown in Figure 4d−f and Figure S3d−f (see the Supporting Information). Figure 4 and Figure S3 clearly show that only π orbitals are involved in every transition. Furthermore, the n-type orbitals are quite buried and the first n-type orbital below the highest occupied molecular orbital (HOMO) is HOMO 5 or HOMO-6, as presented in Figures S4 and S5 in the Supporting Information. Therefore, these calculations provide further theoretical support to disregard the contribution of the $n \rightarrow \pi^*$ transition to the absorption spectrum. According to energy profile diagrams, HOMO → LUMO, HOMO-1 → LUMO $\pi \rightarrow \pi^*$ transitions contribute to the dual absorption of 4-hydroxycoumarin and 4-methoxycoumarin. The dual absorption nature of warfarin at lower pH can also be explained to arise from transitions originating from distinct but energetically close occupied orbitals to the LUMO. The DFT calculated wavelengths agree well with those obtained from experiments. Theoretically, thecalculated oscillator strength corresponding to any transition is comparable with the experimentally observed optical density. For deprotonated warfarin and 4-hydroxycoumarin, oscillator strengths are relatively high for HOMO → LUMO transitions, while they are small for other higher energy transitions. These results explain the experimentally observed single absorption nature of the anionic species at high pH. In addition, the calculated absorption wavelength is the highest for the warfarin anion, which also explains the red shift observed in the warfarin absorption spectrum with an increase in pH.

The only observation that is not reproduced by the TDDFT calculations is the relative intensities of the lower and higher wavelength transitions in the experimental absorption spectra of warfarin and 4-hydroxycoumarin at low pH. Therefore, a more accurate, albeit computationally expensive method, EOM-CCSD, has been used to perform calculations on 4-methoxycoumarin to address this issue (Table 2).[41] 4-Methoxycoumarin is selected instead of warfarin to reduce computational cost as well as to restrict any contribution from the anionic form in the dual absorption. This calculation has been carried out in the gas phase because the inclusion of solvent effects increases computational costs significantly; moreover, EOM-CCSD calculations with continuum solvation models are known to have large errors.[42] The oscillator strengths predicted by EOM-CCSD are remarkably consistent with experimental absorbance. The absolute values of the excitation energies predicted by EOM-CCSD are higher than those predicted by TDDFT and the experiment, and this is possibly due to cancellation of errors in TDDFT and because EOM-CCSD calculations are performed for the isolated molecule corresponding to the gas phase, while the experimental spectrum is obtained in solution.

To validate the theoretical predictions, steady-state and time-resolved emission studies are performed on warfarin. In agreement with the earlier reports, emission bands, independent of the excitation wavelengths, are observed at ∼356 and ∼390 nm at pH = 3 and 9, respectively (Figure 5a and Figure 5b, respectively).[10,19,27] If warfarin exists as different structural isomers, then multiple distinct emission bands are expected. The single emission band supports the theoretical prediction that the dual absorption arises not from structural isomers but rather due to excitations from two distinct energetically accessible states. As radiative emission occurs exclusively for the $S_1 \rightarrow S_0$ transition, any fluorophore excited to S_2 (second excited singlet state) would initially decay to S_1 through internal conversion. This explains the single emission band of warfarin at 356 nm, irrespective of exciting the molecule to S_2 (280 nm) or S_1 (310 nm). On the other hand, at pH = 9, the red-shifted single emission peak at 392 nm is the emission of the warfarin anion. DFT calculations performed on excited-state structures of warfarin (Table S1 in the Supporting Information) agree well with the experimental results.

Earlier studies, limited by instrumental resolution, have speculated ultrafast excited-state dynamics of warfarin to be responsible for the single emission peak in steady-state fluorescence spectra.[10,19,27] Time-resolved emission experiments on warfarin at pH = 3 and 9 with λ_{ex} = 310 nm are performed. Time profiles, collected at several wavelengths across the steady-state fluorescence spectra (Figure 5c,d), exhibit a uniform decay rate at pH = 3, irrespective of emission wavelengths, indicating the absence of any excited-state

https://doi.org/10.1021/acs.jpcb.0c10824
J. Phys. Chem. B 2021, 125, 2871−2878

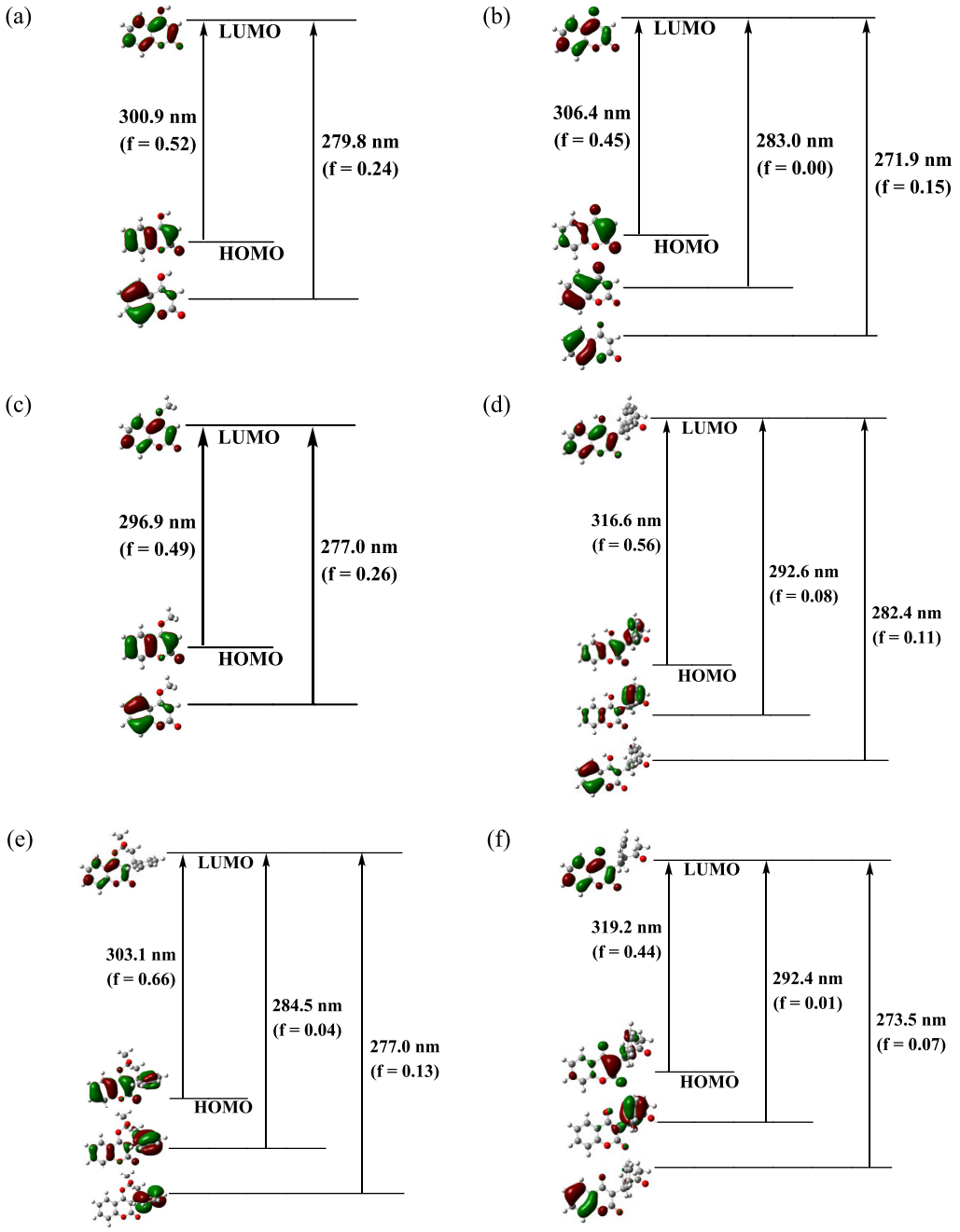

Figure 4. Energy level diagrams for (a) 4-hydroxycoumarin and (b) its anion, (c) 4-methoxycoumarin, and warfarin in its (d) open-chain, (e) cyclic hemiketal, and (f) anionic forms in the aqueous medium (SMD solvation model). Molecular orbitals are calculated at the HF/6-31+G(d,p) level of theory, while the excitation energies are calculated using the TDDFT B3LYP/6-31+G(d,p) method.

Table 2. Calculated Spectral Parameters for Electronic Transitions of 4-Methoxycoumarin in Vacuum at the EOM-CCSD/6-31+G(d,p) Level of Theory

	absorption λ_{max} (nm)	oscillator strength (f)	predominant orbitals involved
first allowed transition	272.0	0.10	HOMO → LUMO
second allowed transition	235.1	0.24	(HOMO-1) → LUMO and HOMO → LUMO

dynamic process of a time scale slower than 50 ps in warfarin. A single exponential fit to the emission time profile at 360 nm provides the fluorescence lifetime of warfarin at pH = 3 to be ~55 ps. Emission time profiles of deprotonated warfarin at pH = 9 also indicate a constant, yet slower, decay rate of ~125 ps, irrespective of the emission wavelength. These observed emission lifetimes are consistent with the fluorescence quantum yields (φ) at pH = 3 (φ = 2.71 × 10^{-3}) and 9 (φ = 4.77 × 10^{-3}), calculated using anthracene as a standard reference compound at its excitation wavelength (305 nm) in cyclohexane (φ = 0.36).[43] The calculated non-radiative decay rate, found to be ~2.3 times slower at pH = 9, further validates the presence of the anionic species at higher pH. The rigidity due to extended conjugation in the anion suppresses the non-radiative decay channel, thereby increasing the emission quantum yield as well as emission lifetime of deprotonated

https://doi.org/10.1021/acs.jpcb.0c10824
J. Phys. Chem. B 2021, 125, 2871−2878

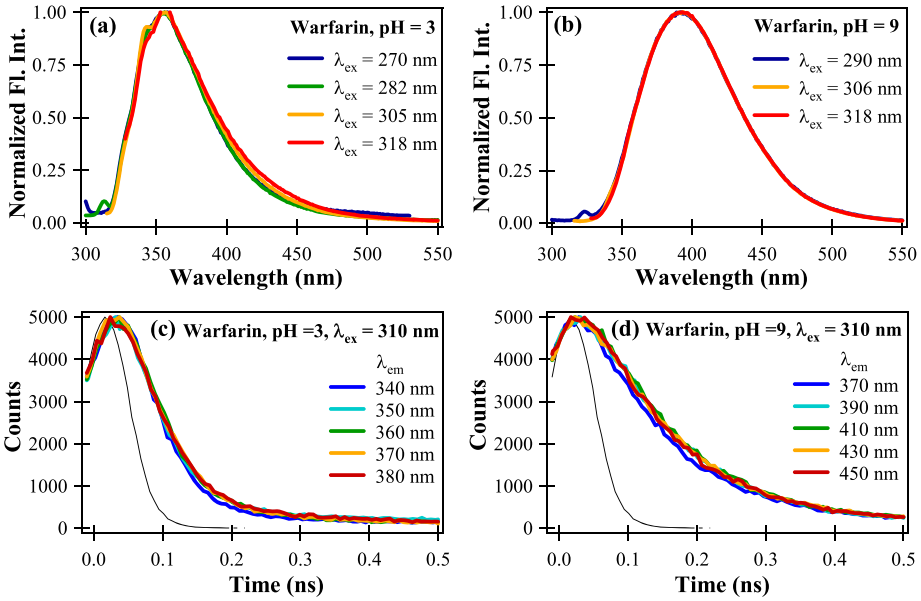

Figure 5. Normalized emission spectra of warfarin in (a) pH = 3 and (b) pH = 9 at different excitation wavelengths.Time-resolved fluorescence profiles of warfarin in (c) pH = 3 and (d) pH = 9 at different emission wavelengths, as indicated (λ_{ex} = 310 nm). Black solid line represents instrumental response function (IRF).

warfarin. As discussed earlier, our theoretical calculations indicate that a single species of deprotonated warfarin is present in solution at higher pH.

Since warfarin is used as an anti-coagulant drug as well as a prototype fluorescent probe in biology, it is imperative to ascertain which isomeric form of warfarin binds to HSA. The reported X-ray diffraction data of the crystal structure of the warfarin-HSA complex are consistent with the open-chain form of the warfarin molecule;[44] however, the protonated or deprotonated status of warfarin, when bound to HSA, cannot be determined from X-ray diffraction. To determine the protonation status of warfarin in the enzyme environment, we perform absorption and emission experiments of the warfarin-HSA complex at three different pH values (3, 7.4, and 9). The absorption spectrum at any pH shows a single absorption band at ∼310 nm (Figure S6a in the Supporting Information). The emission spectrum shows a single fluorescence peak at ∼382 nm (Figure S6b in the Supporting Information). Interestingly, the absorption as well as emission spectra of HSA-bound warfarin is almost independent of pH. Close resemblance of the absorption spectra of warfarin, when bound to HSA, with its deprotonated form indicates that warfarin is present in the open-chain anionic form in the HSA binding pocket. However, the emission spectrum shows an ∼10 nm blue shift from that obtained for deprotonated warfarin in aqueous solution (pH = 9). The high microviscosity of the binding pocket, as compared to the surrounding, can explain the blue shift of the emission maximum. In a previous report,[45] a gradual blue shift of warfarin emission maxima has been reported with increasing viscosity of the solvent. Above experimental evidence also suggest that the pH of the protein solution has minimal effect on the warfarin binding site and that the warfarin molecule is confined in the protein pocket.

CONCLUSIONS

Using a combined theoretical and experimental study of warfarin, we confirm that the coumarin moiety of warfarin is solely responsible for the absorption spectrum of warfarin in its aqueous form. We demonstrate that the dual absorption feature in the absorption spectrum is not indicative of the presence of multiple isomeric structures of warfarin in solution but rather due to excitations arising from two closely spaced occupied molecular orbitals terminating at the lowest unoccupied molecular orbital. Our study also illustrates that the ring-chain isomerism of molecules structurally similar to warfarin, as reported in previous studies, cannot be explained using the spectral features of the warfarin absorption spectrum. Further, this report decisively eliminates the possibility of the $n \rightarrow \pi^*$ transition contributing to the dual absorption feature of warfarin. The steady-state and the time-resolved emission experiments provide additional support to distinguish between the neutral and the anionic isomers of warfarin. Further, these results allow us to determine that warfarin exists in the open-chain anionic form in the active site of HSA. Finally, as the coumarin moiety, which mostly contributes to the absorption and emission spectrum of warfarin, is present in many drugs, our study will be helpful in examining various drug−receptor interactions.

ASSOCIATED CONTENT

Supporting Information

The Supporting Information is available free of charge at https://pubs.acs.org/doi/10.1021/acs.jpcb.0c10824.

Structure of the warfarin anion, absorption spectra of warfarin and pyranocoumarin, pyranocoumarin in acidic pH solution, calculated spectral parameters of warfarin, and absorption and emission spectra of the warfarin-HSA complex (PDF)

AUTHOR INFORMATION

Corresponding Authors

Anirban Hazra − *Department of Chemistry, Indian Institute of Science Education and Research, Pune 411008, India;* orcid.org/0000-0003-2012-381X; Email: ahazra@iiserpune.ac.in

https://doi.org/10.1021/acs.jpcb.0c10824
J. Phys. Chem. B 2021, 125, 2871−2878

Sayan Bagchi − *Physical and Materials Chemistry Division, CSIR-National Chemical Laboratory, Pune 411008, India; Academy of Scientific and Innovative Research (AcSIR), Ghaziabad 201002, India;* orcid.org/0000-0001-6932-3113; Email: s.bagchi@ncl.res.in

Authors

Sushil S. Sakpal − *Physical and Materials Chemistry Division, CSIR-National Chemical Laboratory, Pune 411008, India; Academy of Scientific and Innovative Research (AcSIR), Ghaziabad 201002, India*

Deborin Ghosh − *Physical and Materials Chemistry Division, CSIR-National Chemical Laboratory, Pune 411008, India*

Meghna A. Manae − *Department of Chemistry, Indian Institute of Science Education and Research, Pune 411008, India*

Complete contact information is available at: https://pubs.acs.org/10.1021/acs.jpcb.0c10824

Author Contributions

#S.S.S. and D.G. contributed equally to this work.

Notes

The authors declare no competing financial interest.

■ ACKNOWLEDGMENTS

This work was financially supported by SERB India (EMR/2016/000576). D.G. acknowledges SERB India for the NPDF fellowship (PDF/2018/000046). S.S.S. acknowledges UGC for the fellowship. The authors would like to thank Prof. Anindya Datta, IIT Bombay, for help with the time-resolved fluorescence experiments.

■ REFERENCES

(1) Li, T.; Chang, C. Y.; Jin, D. Y.; Lin, P. J.; Khvorova, A.; Stafford, D. W. Identification of the gene for vitamin K epoxide reductase. *Nature* **2004**, *427*, 541−544.

(2) Rost, S.; Fregin, A.; Ivaskevicius, V.; Conzelmann, E.; Hörtnagel, K.; Pelz, H.-J.; Lappegard, K.; Seifried, E.; Scharrer, I.; Tuddenham, E. G.; Müller, C. R.; Strom, T. M.; Oldenburg, J. Mutations in VKORC1 cause warfarin resistance and multiple coagulation factor deficiency type 2. *Nature* **2004**, *427*, 537−541.

(3) Mohr, J. P.; Thompson, J. L. P.; Lazar, R. M.; Levin, B.; Sacco, R. L.; Furie, K. L.; Kistler, J. P.; Albers, G. W.; Pettigrew, L. C.; Adams, H. P., Jr.; Jackson, C. M.; Pullicino, P. A comparison of warfarin and aspirin for the prevention of recurrent ischemic stroke. *N. Engl. J. Med.* **2001**, *345*, 1444−1451.

(4) Peyrin, E.; Guillaume, Y. C.; Guinchard, C. Characterization of Solute Binding at Human Serum Albumin Site II and its Geometry Using a Biochromatographic Approach. *Biophys. J.* **1999**, *77*, 1206−1212.

(5) Liu, R.; Perez-Aguilar, J. M.; Liang, D.; Saven, J. G. Binding Site and Affinity Prediction of General Anesthetics to Protein Targets Using Docking. *Anesth. Analg.* **2012**, *114*, 947−955.

(6) Nicholson, J. P.; Wolmarans, M. R.; Park, G. R. The role of albumin in critical illness. *Br. J. Anaesth.* **2000**, *85*, 599−610.

(7) CF, C. Optical studies of drug-protein complexes. IV. The interaction of warfarin and dicoumarol with human serum albumin. *Mol. Pharmacol.* **1970**, *1*, 1−12.

(8) Rosengren, A. M.; Karlsson, B. C. G.; Nicholls, I. A. Monitoring the distribution of warfarin in blood plasma. *ACS Med. Chem. Lett.* **2012**, *3*, 650−652.

(9) Smirnova, T. D.; Nevryueva, N. V.; Shtykov, S. N.; Kochubei, V. I.; Zhemerichkin, D. A. Determination of warfarin by sensitized fluorescence using organized media. *J. Anal. Chem.* **2009**, *64*, 1114−1119.

(10) Al-Dubaili, N.; Saleh, N. Sequestration Effect on the Open-Cyclic Switchable Property of Warfarin Induced by Cyclodextrin: Time-Resolved Fluorescence Study. *Molecules* **2017**, *22*, 1326.

(11) Vasquez, J. M.; Vu, A.; Schultz, J. S.; Vullev, V. I. Fluorescence enhancement of warfarin induced by interaction with beta-cyclodextrin. *Biotechnol. Prog.* **2009**, *25*, 906−914.

(12) Otagiri, M.; Imai, T.; Koinuma, H.; Matsumoto, U. Spectroscopic study of the interaction of coumarin anticoagulant drugs with polyvinylpyrrolidone. *J. Pharm. Biomed. Anal.* **1989**, *7*, 929−935.

(13) Valente, E. J.; Lingafelter, E. C.; Porter, W. R.; Trager, W. F. Structure of warfarin in solution. *J. Med. Chem.* **1977**, *20*, 1489−1493.

(14) Valente, E. J.; Porter, W. R.; Trager, W. F. Conformations of selected 3-substituted 4-hydroxycoumarins in solution by nuclear magnetic resonance. Warfarin and phenprocoumon. *J. Med. Chem.* **1978**, *21*, 231−234.

(15) Nowak, P. M.; Sagan, F.; Mitoraj, M. P. Origin of Remarkably Different Acidity of Hydroxycoumarins—Joint Experimental and Theoretical Studies. *J. Phys. Chem. B* **2017**, *121*, 4554−4561.

(16) Giannini, D. D.; Chan, K. K.; Roberts, J. D. Carbon-13 Nuclear Magnetic Resonance Spectroscopy. Structure of the Anticoagulant Warfarin and Related Compounds in Solution. *Proc. Natl. Acad. Sci. U. S. A.* **1974**, *71*, 4221−4223.

(17) Pisklak, M.; Maciejewska, D.; Herold, F.; Wawer, I. Solid state structure of coumarin anticoagulants: warfarin and sintrom. 13C CPMAS NMR and GIAO DFT calculations. *J. Mol. Struct.* **2003**, *649*, 169−176.

(18) Guasch, L.; Peach, M. L.; Nicklaus, M. C. Tautomerism of Warfarin: Combined Chemoinformatics, Quantum Chemical, and NMR Investigation. *J. Org. Chem.* **2015**, *80*, 9900−9909.

(19) Karlsson, B. C. G.; Rosengren, A. M.; Andersson, P. O.; Nicholls, I. A. The Spectrophysics of Warfarin: Implications for Protein Binding. *J. Phys. Chem. B* **2007**, *111*, 10520−10528.

(20) Rosengren, A. M.; Karlsson, B. C. G. Spectroscopic evidence for the presence of the cyclic hemiketal form of warfarin in aqueous solution: Consequences for bioavailability. *Biochem. Biophys. Res. Commun.* **2011**, *407*, 318−320.

(21) Guasch, L.; Sitzmann, M.; Nicklaus, M. C. Enumeration of Ring−Chain Tautomers Based on SMIRKS Rules. *J. Chem. Inf. Model.* **2014**, *54*, 2423−2432.

(22) Kumar, P.; Kumar, V.; Gupta, R. Detection of the anticoagulant drug warfarin by palladium complexes. *Dalton Trans.* **2017**, *46*, 10205−10209.

(23) Kumari, R.; Nath, M. Synthesis and characterization of novel trimethyltin(IV) and tributylltin(IV) complexes of anticoagulant, WARFARIN: Potential DNA binding and plasmid cleaving agents. *Inorg. Chem. Commun.* **2018**, *95*, 40−46.

(24) Dar, A. A.; Chat, O. A. Cosolubilization of Coumarin30 and Warfarin in Cationic, Anionic, and Nonionic Micelles: A Micelle−Water Interfacial Charge Dependent FRET. *J. Phys. Chem. B* **2015**, *119*, 11632−11642.

(25) Karlsson, B. C. G.; Olsson, G. D.; Friedman, R.; Rosengren, A. M.; Henschel, H.; Nicholls, I. A. How Warfarin's Structural Diversity Influences Its Phospholipid Bilayer Membrane Permeation. *J. Phys. Chem. B* **2013**, *117*, 2384−2395.

(26) Malde, A. K.; Stroet, M.; Caron, B.; Visscher, K. M.; Mark, A. E. Predicting the Prevalence of Alternative Warfarin Tautomers in Solution. *J. Chem. Theory Comput.* **2018**, *14*, 4405−4415.

(27) Karlsson, B. C. G.; Rosengren, A. M.; Andersson, P. O.; Nicholls, I. A. Molecular Insights on the Two Fluorescence Lifetimes Displayed by Warfarin from Fluorescence Anisotropy and Molecular Dynamics Studies. *J. Phys. Chem. B* **2009**, *113*, 7945−7949.

(28) Chou, P. T.; Martinez, M. L.; Clements, J. H. Reversal of Excitation Behavior of Proton-Transfer vs. Charge-Transfer by Dielectric Perturbation of Electronic Manifolds. *J. Phys. Chem.* **1993**, *97*, 2618−2622.

(29) Lee, C.; Yang, W.; Parr, R. G. Development of the Colle-Salvetti correlation-energy formula into a functional of the electron density. *Phys. Rev. B* **1988**, *37*, 785−789.

(30) Becke, A. D. Density-functional thermochemistry. III. The role of exact exchange. *J. Chem. Phys.* **1993**, *98*, 5648−5652.
(31) Marenich, A. V.; Cramer, C. J.; Truhlar, D. G. Universal Solvation Model Based on Solute Electron Density and on a Continuum Model of the Solvent Defined by the Bulk Dielectric Constant and Atomic Surface Tensions. *J. Phys. Chem. B* **2009**, *113*, 6378−6396.
(32) Jacquemin, D.; Perpète, E. A.; Assfeld, X.; Scalmani, G.; Frisch, M. J.; Adamo, C. The geometries, absorption and fluorescence wavelengths of solvated fluorescent coumarins: A CIS and TD-DFT comparative study. *Chem. Phys. Lett.* **2007**, *438*, 208−212.
(33) Cerón-Carrasco, J. P.; Fanuel, M.; Charaf-Eddin, A.; Jacquemin, D. Interplay between solvent models and predicted optical spectra: A TD-DFT study of 7-OH-coumarin. *Chem. Phys. Lett.* **2013**, *556*, 122−126.
(34) Jacquemin, D.; Perpète, E. A.; Scuseria, G. E.; Ciofini, I.; Adamo, C. TD-DFT Performance for the Visible Absorption Spectra of Organic Dyes: Conventional versus Long-Range Hybrids. *J. Chem. Theory Comput.* **2008**, *4*, 123−135.
(35) Jacquemin, D.; Planchat, A.; Adamo, C.; Mennucci, B. TD-DFT Assessment of Functionals for Optical 0−0 Transitions in Solvated Dyes. *J. Chem. Theory Comput.* **2012**, *8*, 2359−2372.
(36) Frisch, M. J.; Trucks, G. W.; Schlegel, H. B.; Scuseria, G. E.; Robb, M. A.; Cheeseman, J. R.; Scalmani, G.; Barone, V.; Mennucci, B.; Petersson, G. A. et al., *Gaussian 09* Revision A.01, Gaussian, Inc.: Wallingford CT 2009.
(37) Werner, H.-J.; Knowles, P. J.; Knizia, G.; Manby, F. R.; Schütz, M.; Celani, P.; Korona, T.; Lindh, R.; Mitrushenkov, A.; Rauhut, G. *version 2010.1, a package of ab initio programs* 2010.
(38) Werner, H.-J.; Knowles, P. J.; Knizia, G.; Manby, F. R.; Schütz, M. Molpro: a general-purpose quantum chemistry program package. *WIREs Comput. Mol. Sci.* **2012**, *2*, 242−253.
(39) Moore, T. A.; Harter, M. L.; Song, P.-S. Ultraviolet spectra of coumarins and psoralens. *J. Mol. Spectrosc.* **1971**, *40*, 144−157.
(40) Song, P.-S.; Gordon, W. H., III Spectroscopic study of the excited states of coumarin. *J. Phys. Chem.* **1970**, *74*, 4234−4240.
(41) Caricato, M.; Trucks, G. W.; Frisch, M. J.; Wiberg, K. B. Oscillator Strength: How Does TDDFT Compare to EOM-CCSD? *J. Chem. Theory Comput.* **2011**, *7*, 456−466.
(42) Ren, S.; Harms, J.; Caricato, M. An EOM-CCSD-PCM Benchmark for Electronic Excitation Energies of Solvated Molecules. *J. Chem. Theory Comput.* **2017**, *13*, 117−124.
(43) Berlman, I. B., *Handbook of Fluorescence Spectra of Aromatic Molecules;* Academic Press: New York, 1971.
(44) Petitpas, I.; Bhattacharya, A. A.; Twine, S.; East, M.; Curry, S. Crystal Structure Analysis of Warfarin Binding to Human Serum Albumin: ANATOMY OF DRUG SITE I. *J. Biol. Chem.* **2001**, *276*, 22804−22809.
(45) Kasai-Morita, S.; Horie, T.; Awazu, S. Influence of the N-B transition of human serum albumin on the structure of the warfarin-binding site. *Biochim. Biophys. Acta* **1987**, *915*, 277−283.

https://doi.org/10.1021/acs.jpcb.0c10824
J. Phys. Chem. B 2021, 125, 2871−2878

THE JOURNAL OF PHYSICAL CHEMISTRY LETTERS
A JOURNAL OF THE AMERICAN CHEMICAL SOCIETY

pubs.acs.org/JPCL

Letter

Transition of a Deep Eutectic Solution to Aqueous Solution: A Dynamical Perspective of the Dissolved Solute

Sushil S. Sakpal,[#] Samadhan H. Deshmukh,[#] Srijan Chatterjee, Deborin Ghosh, and Sayan Bagchi*

Cite This: *J. Phys. Chem. Lett.* 2021, 12, 8784–8789

Read Online

ACCESS | Metrics & More | Article Recommendations | Supporting Information

ABSTRACT: Disruption of the deep eutectic solvent (DES) nanostructure around the dissolved solute upon addition of water is investigated by polarization-selective two-dimensional infrared spectroscopy and molecular dynamics simulations. The heterogeneous DES nanostructure around the solute is partially retained up to 41 wt % of added water, although water molecules are gradually incorporated in the solute's solvation shell even at lower hydration levels. Beyond 41 wt %, the solute is observed to be preferentially solvated by water. This composition denotes the upper hydration limit of the deep eutectic solvent above which the solute senses an aqueous solvation environment. Interestingly, our results indicate that the transition from a deep eutectic solvation environment to an aqueous one around the dissolved solute can happen at a hydration level lower than that reported for the "water in DES" to "DES in water" transition.

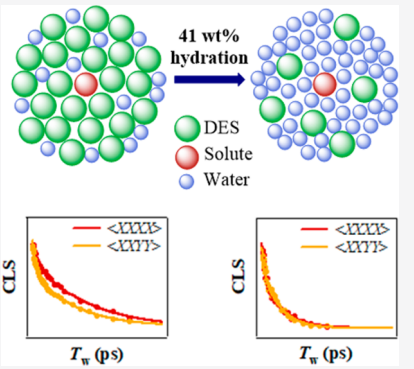

Fuelled by searching for environmentally friendly solvents for sustainable chemical processes, deep eutectic solvents (DESs) have emerged as green designer solvents with a wide range of applications.[1−5] A typical DES consists of an HB acceptor (HBA) and an HB donor (HBD), mixed in the eutectic molar ratio.[3,6−8] DES nanostructures, stabilized by intercomponent HB interactions, can be further tuned by the addition of cosolvents capable of disrupting the native HB networks.[6−10] As water can act as both HBA and HBD, these neoteric solvents are highly water-miscible and hygroscopic.[11,12] Recent reports demonstrate that water addition in the eutectic mixtures influences the DES nanostructures and consequently impacts their physicochemical properties.[6] Trends in these properties suggest an upper limit of DES hydration, above which DES behaves like an aqueous solution.[13−15]

Reline, composed of urea (HBD) and choline chloride (ChCl, HBA) in a 2:1 molar ratio, is one of the most widely studied DESs. This solvent has extensive use in biodiesel synthesis, surface coating, and enzymatic reactions.[16−18] Owing to the hygroscopic nature of both urea and ChCl, the presence of water changes the macroscopic properties of reline and perturbs the DES nanostructure.[19] Experimental and theoretical studies have reported water's effect on the physicochemical properties and molecular arrangement of reline.[6,15,20−22] Notably, an unusual transition from an ionic mixture ("water in reline") to an aqueous solution ("reline in water") at 51 wt % water was recently reported by Hammond et al. using neutron diffraction experiments and empirical potential surface refinement (EPSR).[8]

Although various reports studied the disruption of reline nanostructure at certain hydration levels,[6,7,9,15] all the studies focused on understanding the phenomenon from the solvent's perspective in the absence of any dissolved solute. The effect of increasing water content in reline from the solute's perspective has yet to be explored. A favorable arrangement of the DES components around the solute provides an ideal environment for applications like selective catalysis and efficient synthesis.[2] The disruption of the preferred molecular organization in the presence of water might perturb the favorable solute−reline interactions, limiting the use of reline in such applications. Furthermore, water is often intentionally added to improve the DES properties, for example, to lower viscosity.[6,15] Does the solute sense the transition from a heterogeneous ionic mixture to an aqueous solution at the same water content reported by Hammond et al.? In other words, what is the hydration limit above which the interactions between the solute molecule and the DES components cease to exist?

Herein, we report the polarization-selective evolution of the solute's vibrational frequencies, which provides the answers to the questions mentioned above. We also perform molecular dynamics (MD) simulations on different reline−water systems in the solute's presence to obtain a molecular understanding of the solute−solvent interactions at different hydration levels.

Received: June 30, 2021

https://doi.org/10.1021/acs.jpclett.1c02118
J. Phys. Chem. Lett. 2021, 12, 8784–8789

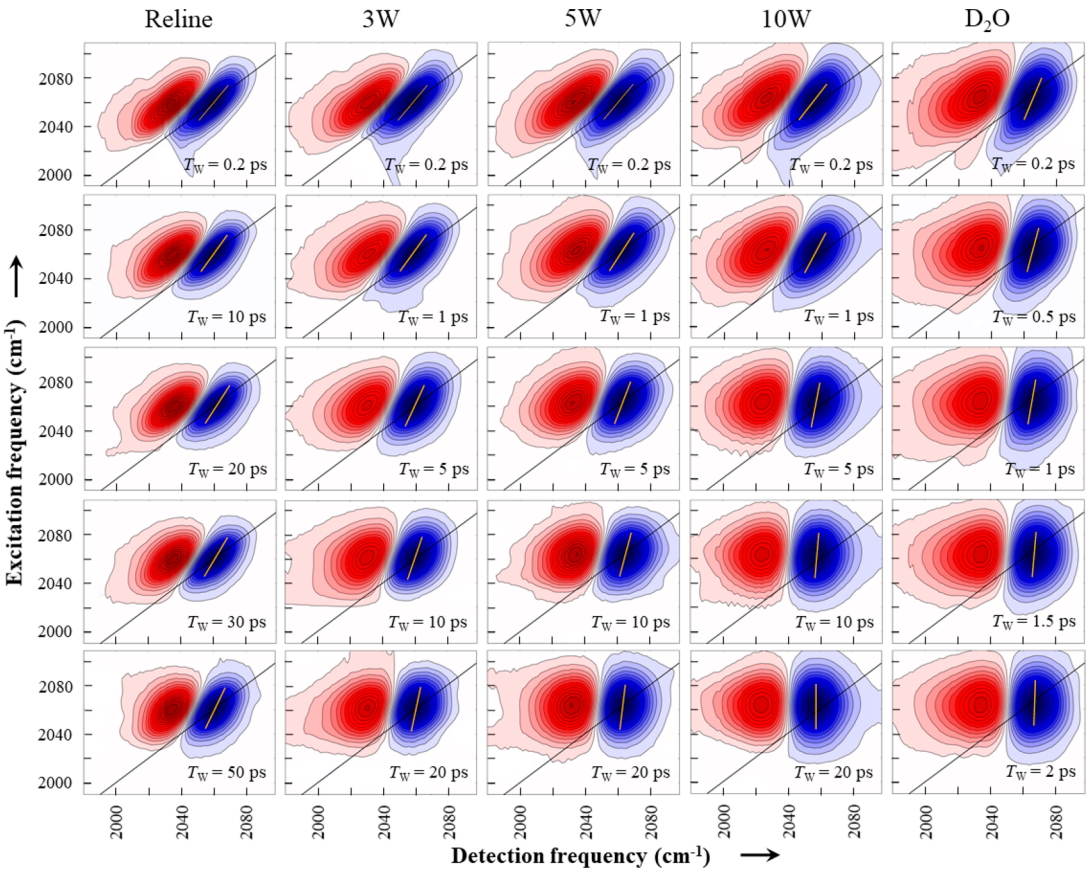

Figure 1. 2D IR spectra of SCN^- in reline, in reline−water (D_2O) mixtures, and in water (D_2O) at $\langle XXXX \rangle$ polarization condition. The peak pairs correspond to $\bar{\nu}_{CN}$. The water content increases from left to right. For a certain hydration level, T_w increases from top to bottom. The CLS is shown in each 2D IR spectrum with a yellow line.

The structural dynamics of the solvent produce frequency evolution within its inhomogeneously broadened vibrational bands. These dynamics are quantified by the frequency−frequency correlation function (FFCF) through time-dependent line shape analysis of two-dimensional infrared (2D IR) spectra.[23,24] When dissolved in a relatively slow-moving solvent, the solute can reorient on a much faster timescale than the solvent's complete structural evolution. The rapid reorientation of the solute contributes to a polarization selectivity of the frequency evolution over time, known as reorientation-induced spectral diffusion (RISD).[25] A recent report on room-temperature ionic liquids (RTILs) shows that polarization dependence of the solute's FFCF can distinguish a slowly evolving environment from an aqueous solution.[23] Considering the gradual lowering of viscosity upon increasing water content in the DESs, polarization-selective 2D IR spectroscopy is suitable to identify the transition from a eutectic to an aqueous environment from the solute's perspective. As thiocyanate is one of the common vibrational probes,[26−29] we have performed polarization-selective 2D IR experiments on ammonium thiocyanate dissolved in reline and reline−water mixtures (Figures 1 and S1). We prepared a series of aqueous reline mixtures (xW) by mixing x (ranging from 0 to 15) moles of water (D_2O) with one mole of reline. Water−reline molar ratios (xW) of 3W, 5W, 10W, and 15W were used (the detailed weight % and mol % are given in Table S1 of the Supporting Information) as solvents along with neat reline and water.

In the 2D IR experiments, three ultrashort femtosecond pulses are focused on the sample at different time delays. The time delay between pulses 1 and 2 is τ, and that between 2 and 3 is T_w. Owing to the structural dynamics of the solvent molecules and the reorientation of the solute, the initial CN stretching frequencies of the solute change as a function of T_w. For a particular T_w, the 2D IR spectrum (Figures 1 and S1) correlates the initial solute frequencies after first pulse interaction (ω_τ, excitation frequencies) with the final solute frequencies after third pulse interaction (ω_t, detection frequencies). The blue peaks ($\omega_\tau \approx 2060$ cm^{-1}, $\omega_t \approx 2060$ cm^{-1}) correspond to $\nu = 0 \rightarrow 1$ transition and the red peaks ($\omega_\tau \approx 2060$ cm^{-1}, $\omega_t \approx 2030$ cm^{-1}) correspond to $\nu = 1 \rightarrow 2$ transitions, shifted by the vibrational anharmonicity along ω_t. The 2D IR peaks are diagonally elongated at a shorter T_w because of a greater correlation between the initial and the final CN frequencies. However, the correlation decreases with the evolution of frequencies over time, and the peaks gradually become upright with an increase in T_w. Figure 1 indicates that the peaks become upright at a shorter T_w as reline's water content increases. As the faster structural dynamics of the solvent leads to a faster correlation decay, the T_w -dependent 2D IR spectra in different solvation environment are consistent with the decrease in the DES viscosity upon water addition (Table S2).

We have extracted the FFCF encoded in the T_w -dependent 2D IR spectra for two different polarization conditions, $\langle XXXX \rangle$ and $\langle XXYY \rangle$, in terms of the center line slope (CLS) decay[23] (Figure 2a−d and Tables S3 and S4). For

https://doi.org/10.1021/acs.jpclett.1c02118
J. Phys. Chem. Lett. 2021, 12, 8784−8789

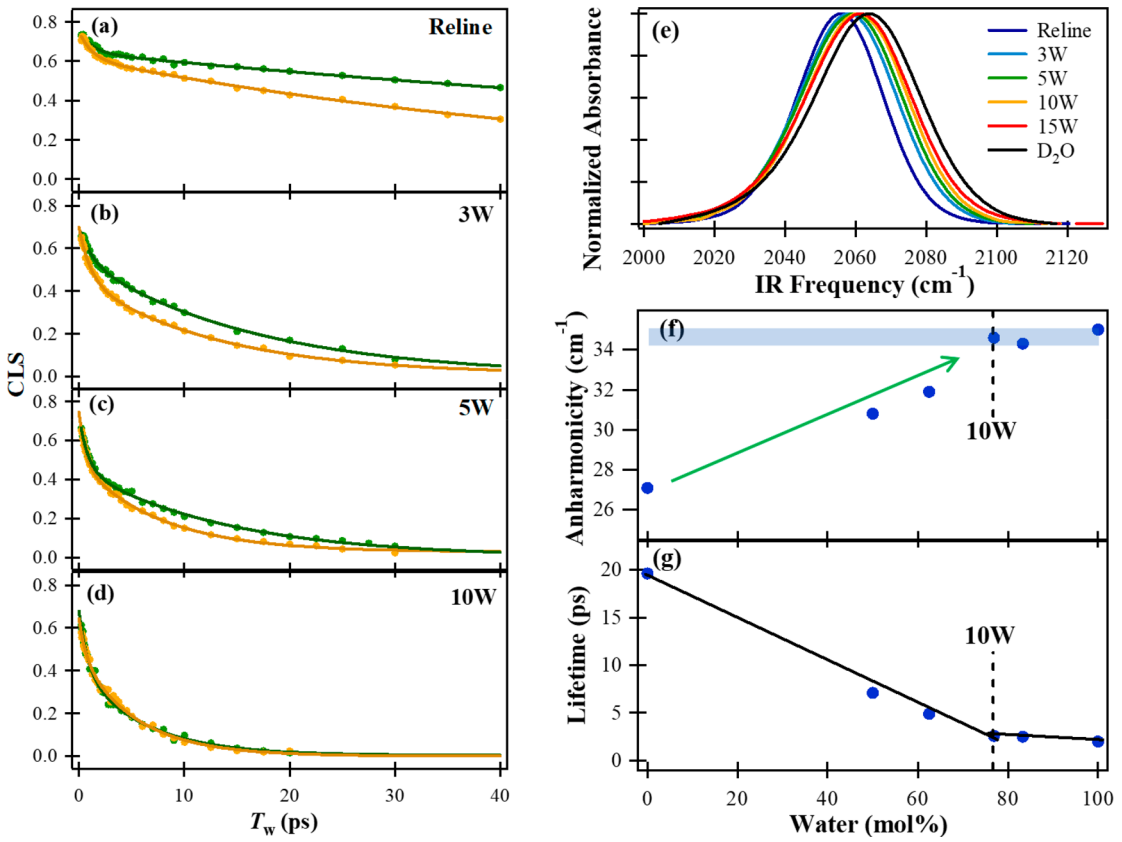

Figure 2. (a–d) CLS decay curves of SCN^- in reline and in reline–water mixtures for ⟨*XXXX*⟩ (green) and ⟨*XXYY*⟩ (yellow) polarization conditions. Polarization selectivity is observed for reline, 3W, and 5W. The CLS decays become identical at 10W within experimental error. (e) FTIR spectrum of ammonium thiocyanate in reline, in various reline–D_2O mixtures, and in neat D_2O. The peak maximum shows a gradual blue-shift with increasing hydration level of the solvent. (f) SCN^- anharmonicity in reline and reline–D_2O mixtures shows a gradual increase up to 10W (green arrow), beyond which the anharmonicity remains constant (shaded region) within experimental error bar. (g) SCN^- vibrational lifetime in reline and reline–H_2O mixtures suggests a nonmonotonic change in the solvation environment at 10W.

reline, the CLS for the ⟨*XXXX*⟩ polarization (green) shows a slower decay than that for the ⟨*XXYY*⟩ polarization (yellow). The polarization-selective CLS decays are also observed for 3W and 5W, although the difference in the decays becomes smaller with the increase in the water content. Interestingly, the CLS decays become identical for both ⟨*XXXX*⟩ and ⟨*XXYY*⟩ polarization conditions at 10W within experimental error. Further addition of water shows no polarization-dependence of the CLS decays.

We have analyzed the anisotropy decay kinetics of the different reline–water systems (Figure S2 and Table S5) to understand the origin of the polarization dependence of the CLS decays. The CLS decay timescales in both ⟨*XXXX*⟩ and ⟨*XXYY*⟩ polarization conditions are slower than that of the corresponding anisotropy decay timescales (~6 ps) for reline, 3W, and 5W. The CLS decays for 10W and above are either comparable to or faster than the anisotropy decays. These results strongly support that the polarization-selective CLS decays in Figure 2a–c arise from RISD, where the solute reorientation occurs without complete randomization of the DES structure. In a viscous solvent like reline, a component of the solvent structure contributing to the overall CN vibrational band can be considered static on the solute reorientation timescale, giving rise to the polarization selectivity.[23]

The blue-shift in the CN IR peak (Figure 2e and Table S6) with increasing water content indicates an increment in solute–water HB interaction.[30] The decrease in the difference between the ⟨*XXXX*⟩ and ⟨*XXYY*⟩ decays from reline to 5W arises because of the increase in the rapidly fluctuating (~1.5 ps)[24,31] water molecules around the solute with increasing hydration. However, the polarization-selective decays at 3W and 5W demonstrate that the solute is still interacting with the slowly fluctuating reline through the transition dipole's angular motion. In other words, the huge difference between the fluctuation timescales between reline and water implies that the polarization dependence arises because of the presence of DES components around the solute at these hydration levels. A plausible explanation toward the identical CLS decays at 10W is that the solute is predominantly solvated by the water molecules that fluctuate at a timescale faster than or comparable to the solute's reorientation. Any further increase in the hydration level (up to neat water) would not further perturb the solvation shell of the solute, and the CLS decays remain identical, independent of polarization conditions. From the solute's perspective, the transition from a deep eutectic solution (solute–DES interaction) to an aqueous solution (only solute–water interaction) occurs at ~10W (41 wt % water).

However, it is to be noted that the merging of the CLS decays alone cannot provide a molecular picture of the transition in the solvation environment. In fact, although the CLS decays become identical at 10W in both the polarization conditions, the CLS decay timescales continue to gradually accelerate beyond 10W (Tables S3 and S4) with further

https://doi.org/10.1021/acs.jpclett.1c02118
J. Phys. Chem. Lett. 2021, 12, 8784–8789

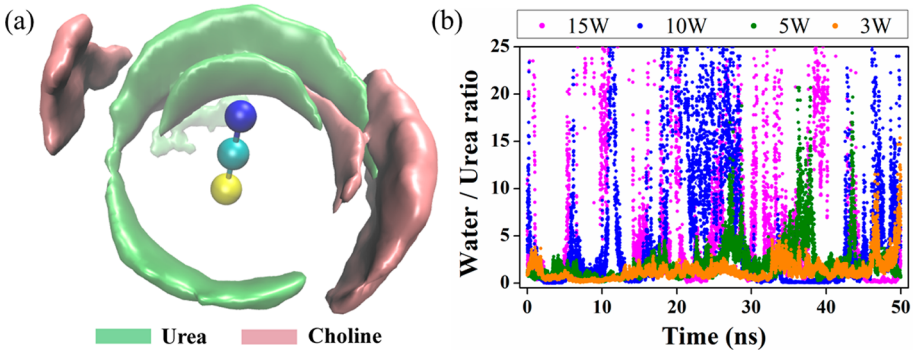

Figure 3. (a) Spatial distribution function (SDF) of urea and choline around SCN^- in neat reline. (b) Graph of water/urea ratio within 10 Å of the SCN^- vs time in different reline−water mixtures.

increase in the water content. This gradual acceleration might imply that the local solvation continues to evolve beyond 10W and thereby contradicts our hypothesis that an aqueous environment around the solute is formed at 41 wt % water. To verify the transition from a deep eutectic solution to an aqueous solution, we have further looked into complementary experimental observables and MD simulations.

To obtain better insights about the local solvation, we have looked into the vibrational anharmonicity. Previous studies of thiocyanate reported that proximity to the cations usually results in the lowering of the vibrational anharmonicity.[32−35] We have estimated the anharmonicity to gradually increase from ∼27 cm^{-1} in reline to ∼35 cm^{-1} at 10W (Table S7 and Figure 2f). However, the anharmonicity does not change for 15W and neat water within the experimental error limit. This trend in the anharmonicity is in agreement with the gradual replacement of the ionic DES components around the solute by water molecules up to 10W.

We have also performed MD simulations to further probe the local solvation around the solute. Although earlier simulation reports investigated the bulk nature of the reline−water interaction at different hydration levels,[7,9,15] the local solvation around a solute was not explored. We have calculated the spatial distribution function (SDF) which provides the three-dimensional density distribution of urea and choline around the solute in neat reline. Figure 3a indicates that, although choline contains a hydroxyl group which can directly interact with the CN, solute−urea interaction is preferred over solute−choline interaction in neat reline. Previous studies of thiocyanate in aqueous solutions reported viscosity-dependent slowdown of the solute rotational dynamics due to interactions with small cations with high charge density.[33] The preferential interaction of the solute with urea over choline (albeit a much larger cation) shows that local environment of the solute plays a larger role in DES than the macroscopic viscosity. We have also computed the water/urea and water/choline ratios within 5 and 10 Å of the solute in different reline−water mixtures. The ratios, averaged along the trajectories, show an increase with increasing water content of reline (Table S8). However, a very interesting phenomenon is observed when the ratios are plotted as a function of time. Figure 3b indicates that the water/urea ratio gradually increases from 3W and reaches the maximum value at 10W. Beyond 10W, this ratio remains constant. However, the ratios keep switching between high and low values, thereby indicating a solvent exchange process where the water molecules around the solute are replaced by the reline components from time to time. The frequency of the solvent exchange increases with increasing water content. It has previously been reported that molecular exchange between solvent components slow down the solvation dynamics and results in a slower spectral diffusion in an aqueous mixture than in water.[36−38] Thus, the simulation results show that the experimental CLS decay timescales can be interpreted on the basis of solvent exchange. Even though the solute senses an overall aqueous environment at 10W, the decrease in the mole fraction of the reline components in the outer solvation shell with increase in water content plausibly leads to a faster solvent exchange and thereby an acceleration of the CLS decay timescales.

Overall, our computational results indicate that although water interacts with the solute at 5W, a considerable number of heterogeneous reline constituents persist in the thiocyanate solvation shell. At 10W and above, solute−solvent interactions predominantly arise from thiocyanate−water interactions, subsequently decreasing the heterogeneity around the solute. This molecular picture was further validated from experiments using the vibrational lifetimes (T_1) and the CLS values at a short T_w (∼200 fs) (Table S9 and Tables S3 and S4, respectively).

We have measured T_1 for different reline−D_2O mixtures using pump−probe spectroscopy (Figure S3 and Table S9). In pure reline, T_1 of the CN vibrational mode is ∼20 ps. The T_1 values in all other mixtures are constant (∼11 ps) within experimental error. The CN vibration's coupling with the resonant water mode (bending + libration) through HB interaction can explain the invariability of vibrational relaxation timescales at all hydration levels.[39] The constant T_1 indicates the presence of water in the solute solvation shell, even at 3W. As the thiocyanate vibrational lifetime in H_2O is much shorter than that in D_2O,[40] T_1 in reline−H_2O might be a more sensitive probe of solute hydration. We have additionally measured T_1 for different reline−H_2O mixtures (Table S10). Our results show that T_1 of the CN vibrational mode in H_2O gradually decreases with increase in water content up to 10W. Beyond 10W, T_1 is almost constant within the experimental error. This trend in the lifetime indicates that the solute is predominantly solvated by water molecules at 10W. The initial amplitude of the CLS at a very short T_w is a measure of the dynamical heterogeneity around the solute. The decrease in the initial CLS amplitude (Figure 2a−d and Tables S3 and S4) from reline to 10W implies a gradual replacement of slowly moving DES components by fast fluctuating water molecules in the thiocyanate solvation shell (Figure 4).

https://doi.org/10.1021/acs.jpclett.1c02118
J. Phys. Chem. Lett. 2021, 12, 8784−8789

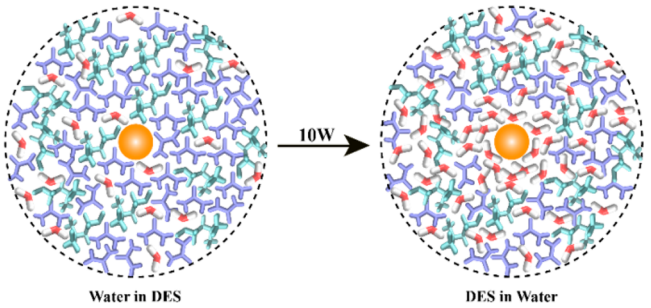

Figure 4. Schematic diagram for "Water in DES" and "DES in Water" transition. The solute molecule is represented by an orange sphere. The solute−water interactions replace all the solute−DES interactions at 10W, thereby creating a neat water-like environment around the solute.

In summary, we provide an upper hydration limit of reline beyond which the solute experiences a water-like environment. Interestingly, our results demonstrate that this upper hydration limit (41 wt % water or 10W) is considerably lower than the limit proposed by Hammond et al. (51 wt % water or 15W) from the neutron diffraction study.[8] However, the diffraction results provided us an upper hydration limit from the solvent's perspective, i.e., when each reline constituent (choline cation, chloride anion, and urea) is solvated by water. The polarization-selective 2D IR results demonstrate that the solute may experience an aqueous environment much before water solvates all the reline constituents. Further, this report illustrates that polarization dependence of the structural dynamics could identify when the solute experiences a transition from the heterogeneous DES environment to an aqueous solution. For a wide range of applications, researchers are presently exploiting hydration as a tool to overcome the limitations of green solvents like DESs and RTILs.[4,7,15,41] This study opens up an avenue to investigate similar transitions from the solute's perspective for viscous green solvents with varying constituents.

■ ASSOCIATED CONTENT

Supporting Information

The Supporting Information is available free of charge at https://pubs.acs.org/doi/10.1021/acs.jpclett.1c02118.

Synthesis of DES and preparation of DES−water mixtures, IR and 2D IR spectroscopy, molecular dynamics simulations, additional figures and tables (PDF)

■ AUTHOR INFORMATION

Corresponding Author

Sayan Bagchi − *Physical and Materials Chemistry Division, National Chemical Laboratory (CSIR-NCL), Pune 411008, India; Academy of Scientific and Innovative Research (AcSIR), Ghaziabad 201002, India;* orcid.org/0000-0001-6932-3113; Email: s.bagchi@ncl.res.in

Authors

Sushil S. Sakpal − *Physical and Materials Chemistry Division, National Chemical Laboratory (CSIR-NCL), Pune 411008, India; Academy of Scientific and Innovative Research (AcSIR), Ghaziabad 201002, India*

Samadhan H. Deshmukh − *Physical and Materials Chemistry Division, National Chemical Laboratory (CSIR-NCL), Pune 411008, India; Academy of Scientific and Innovative Research (AcSIR), Ghaziabad 201002, India*

Srijan Chatterjee − *Physical and Materials Chemistry Division, National Chemical Laboratory (CSIR-NCL), Pune 411008, India; Academy of Scientific and Innovative Research (AcSIR), Ghaziabad 201002, India;* orcid.org/0000-0001-9701-4158

Deborin Ghosh − *Physical and Materials Chemistry Division, National Chemical Laboratory (CSIR-NCL), Pune 411008, India*

Complete contact information is available at: https://pubs.acs.org/10.1021/acs.jpclett.1c02118

Author Contributions

#S.S.S. and S.H.D. contributed equally to this work.

Notes

The authors declare no competing financial interest.

■ ACKNOWLEDGMENTS

S.B. thanks CSIR-NCL and SERB, India (SR/S2/RJN-142/2012 and EMR/2016/000576) for financial support. D.G. acknowledges SERB India (PDF/2018/000046) for financial support. The support and the resources provided by "PARAM Brahma Facility" under the National Supercomputing Mission, Government of India at the Indian Institute of Science Education and Research (IISER) Pune are gratefully acknowledged. S.S.S. acknowledges UGC and S.H.D acknowledges CSIR for research fellowships.

■ REFERENCES

(1) Smith, E. L.; Abbott, A. P.; Ryder, K. S. Deep Eutectic Solvents (DESs) and Their Applications. *Chem. Rev.* **2014**, *114*, 11060−11082.

(2) Wagle, D. V.; Zhao, H.; Baker, G. A. Deep eutectic solvents: sustainable media for nanoscale and functional materials. *Acc. Chem. Res.* **2014**, *47*, 2299−2308.

(3) Hammond, O. S.; Li, H.; Westermann, C.; Al-Murshedi, A. Y. M.; Endres, F.; Abbott, A. P.; Warr, G. G.; Edler, K. J.; Atkin, R. Nanostructure of the deep eutectic solvent/platinum electrode interface as a function of potential and water content. *Nanoscale Horiz.* **2019**, *4*, 158−168.

(4) Liao, H.-G.; Jiang, Y.-X.; Zhou, Z.-Y.; Chen, S.-P.; Sun, S.-G. Shape-Controlled Synthesis of Gold Nanoparticles in Deep Eutectic Solvents for Studies of Structure−Functionality Relationships in Electrocatalysis. *Angew. Chem., Int. Ed.* **2008**, *47*, 9100−9103.

(5) Hammond, O. S.; Edler, K. J.; Bowron, D. T.; Torrente-Murciano, L. Deep eutectic-solvothermal synthesis of nanostructured ceria. *Nat. Commun.* **2017**, *8*, 14150.

(6) Hammond, O. S.; Bowron, D. T.; Edler, K. J. The Effect of Water upon Deep Eutectic Solvent Nanostructure: An Unusual Transition from Ionic Mixture to Aqueous Solution. *Angew. Chem., Int. Ed.* **2017**, *56*, 9782−9785.

(7) Kumari, P.; Shobhna; Kaur, S.; Kashyap, H. K. Influence of Hydration on the Structure of Reline Deep Eutectic Solvent: A Molecular Dynamics Study. *ACS Omega* **2018**, *3*, 15246−15255.

(8) Ma, C.; Laaksonen, A.; Liu, C.; Lu, X.; Ji, X. The peculiar effect of water on ionic liquids and deep eutectic solvents. *Chem. Soc. Rev.* **2018**, *47*, 8685−8720.

(9) Sarkar, S.; Maity, A.; Chakrabarti, R. Microscopic structural features of water in aqueous−reline mixtures of varying compositions. *Phys. Chem. Chem. Phys.* **2021**, *23*, 3779−3793.

(10) Shah, D.; Mansurov, U.; Mjalli, F. S. Intermolecular interactions and solvation effects of dimethylsulfoxide on type III deep eutectic solvents. *Phys. Chem. Chem. Phys.* **2019**, *21*, 17200−17208.

(11) Dugoni, G. C.; Di Pietro, M. E.; Ferro, M.; Castiglione, F.; Ruellan, S.; Moufawad, T.; Moura, L.; Costa Gomes, M. F.; Fourmentin, S.; Mele, A. Effect of Water on Deep Eutectic Solvent/β-Cyclodextrin Systems. *ACS Sustainable Chem. Eng.* **2019**, *7*, 7277−7285.
(12) Durand, E.; Lecomte, J.; Barea, B.; Dubreucq, E.; Lortie, R.; Villeneuve, P. Evaluation of deep eutectic solvent−water binary mixtures for lipase-catalyzed lipophilization of phenolic acids. *Green Chem.* **2013**, *15*, 2275−2282.
(13) Gutierrez, M. a. C.; Ferrer, M. a. L.; Mateo, C. R.; del Monte, F. Freeze-Drying of Aqueous Solutions of Deep Eutectic Solvents: A Suitable Approach to Deep Eutectic Suspensions of Self-Assembled Structures. *Langmuir* **2009**, *25*, 5509−5515.
(14) Passos, H.; Tavares, D. J. P.; Ferreira, A. M.; Freire, M. G.; Coutinho, J. A. P. Are Aqueous Biphasic Systems Composed of Deep Eutectic Solvents Ternary or Quaternary Systems. *ACS Sustainable Chem. Eng.* **2016**, *4*, 2881−2886.
(15) Shah, D.; Mjalli, F. S. Effect of water on the thermo-physical properties of Reline: An experimental and molecular simulation based approach. *Phys. Chem. Chem. Phys.* **2014**, *16*, 23900−23907.
(16) Zhang, Q.; De Oliveira Vigier, K.; Royer, S.; Jerome, F. Deep eutectic solvents: syntheses, properties and applications. *Chem. Soc. Rev.* **2012**, *41*, 7108−7146.
(17) Bucko, M.; Culliton, D.; Betts, A. J.; Bajat, J. B. The electrochemical deposition of Zn−Mn coating from choline chloride−urea deep eutectic solvent. *Trans. Inst. Met. Finish.* **2017**, *95*, 60−64.
(18) Liao, Y. S.; Chen, P. Y.; Sun, I. W. Electrochemical study and recovery of Pb using 1:2 choline chloride/urea deep eutectic solvent: A variety of Pb species $PbSO_4$, PbO_2, and PbO exhibits the analogous thermodynamic behavior. *Electrochim. Acta* **2016**, *214*, 265−275.
(19) Agieienko, V.; Buchner, R. Densities, Viscosities, and Electrical Conductivities of Pure Anhydrous Reline and Its Mixtures with Water in the Temperature Range (293.15 to 338.15) K. *J. Chem. Eng. Data* **2019**, *64*, 4763−4774.
(20) D'Agostino, C.; Gladden, L. F.; Mantle, M. D.; Abbott, A. P.; Ahmed, E. I.; Al-Murshedi, A. Y. M.; Harris, R. C. Molecular and ionic diffusion in aqueous − deep eutectic solvent mixtures: probing inter-molecular interactions using PFG NMR. *Phys. Chem. Chem. Phys.* **2015**, *17*, 15297−15304.
(21) Fetisov, E. O.; Harwood, D. B.; Kuo, I. F. W.; Warrag, S. E. E.; Kroon, M. C.; Peters, C. J.; Siepmann, J. I. First-Principles Molecular Dynamics Study of a Deep Eutectic Solvent: Choline Chloride/Urea and Its Mixture with Water. *J. Phys. Chem. B* **2018**, *122*, 1245−1254.
(22) Posada, E.; Lopez-Salas, N.; Jimenez Rioboo, R. J.; Ferrer, M. L.; Gutierrez, M. C.; del Monte, F. Reline aqueous solutions behaving as liquid mixtures of H-bonded co-solvents: microphase segregation and formation of co-continuous structures as indicated by Brillouin and ^{1}H NMR spectroscopies. *Phys. Chem. Chem. Phys.* **2017**, *19*, 17103−17110.
(23) Tamimi, A.; Bailey, H. E.; Fayer, M. D. Alkyl Chain Length Dependence of the Dynamics and Structure in the Ionic Regions of Room-Temperature Ionic Liquids. *J. Phys. Chem. B* **2016**, *120*, 7488−7501.
(24) Kwak, K.; Park, S.; Finkelstein, I. J.; Fayer, M. D. Frequency-frequency correlation functions and apodization in two-dimensional infrared vibrational echo spectroscopy: a new approach. *J. Chem. Phys.* **2007**, *127*, 124503−124517.
(25) Kramer, P. L.; Nishida, J.; Fayer, M. D. Separation of experimental 2D IR frequency-frequency correlation functions into structural and reorientation-induced contributions. *J. Chem. Phys.* **2015**, *143*, 124505−124516.
(26) Bian, H.; Wen, X.; Li, J.; Chen, H.; Han, S.; Sun, X.; Song, J.; Zhuang, W.; Zheng, J. Ion clustering in aqueous solutions probed with vibrational energy transfer. *Proc. Natl. Acad. Sci. U. S. A.* **2011**, *108*, 4737−4742.
(27) Li, J.; Bian, H.; Chen, H.; Wen, X.; Hoang, B. T.; Zheng, J. Ion Association in Aqueous Solutions Probed through Vibrational Energy Transfers among Cation, Anion, and Water Molecules. *J. Phys. Chem. B* **2013**, *117*, 4274−4283.
(28) Chen, H.; Wen, X.; Guo, X.; Zheng, J. Intermolecular vibrational energy transfers in liquids and solids. *Phys. Chem. Chem. Phys.* **2014**, *16*, 13995−14014.
(29) Cui, Y.; Fulfer, K. D.; Ma, J.; Weldeghiorghis, T. K.; Kuroda, D. G. Solvation dynamics of an ionic probe in choline chloride-based deep eutectic solvents. *Phys. Chem. Chem. Phys.* **2016**, *18*, 31471−31479.
(30) Deb, P.; Haldar, T.; Kashid, S. M.; Banerjee, S.; Chakrabarty, S.; Bagchi, S. Correlating Nitrile IR Frequencies to Local Electrostatics Quantifies Noncovalent Interactions of Peptides and Proteins. *J. Phys. Chem. B* **2016**, *120*, 4034−4046.
(31) Kramer, P. L.; Nishida, J.; Giammanco, C. H.; Tamimi, A.; Fayer, M. D. Observation and theory of reorientation-induced spectral diffusion in polarization-selective 2D IR spectroscopy. *J. Chem. Phys.* **2015**, *142*, 184505−184508.
(32) Roy, V. P.; Kubarych, K. J. Interfacial Hydration Dynamics in Cationic Micelles Using 2D-IR and NMR. *J. Phys. Chem. B* **2017**, *121*, 9621−9630.
(33) Bian, H.; Chen, H.; Zhang, Q.; Li, J.; Wen, X.; Zhuang, W.; Zheng, J. Cation Effects on Rotational Dynamics of Anions and Water Molecules in Alkali (Li+, Na+, K+, Cs+) Thiocyanate (SCN^-) Aqueous Solutions. *J. Phys. Chem. B* **2013**, *117*, 7972−7984.
(34) Park, S.; Ji, M.; Gaffney, K. J. Ligand Exchange Dynamics in Aqueous Solution Studied with 2DIR Spectroscopy. *J. Phys. Chem. B* **2010**, *114*, 6693−6702.
(35) Kiefer, L. M.; Kubarych, K. J. NOESY-Like 2D-IR Spectroscopy Reveals Non-Gaussian Dynamics. *J. Phys. Chem. Lett.* **2016**, *7*, 3819−3824.
(36) Dunbar, J. A.; Arthur, E. J.; White, A. M.; Kubarych, K. J. Ultrafast 2D-IR and Simulation Investigations of Preferential Solvation and Cosolvent Exchange Dynamics. *J. Phys. Chem. B* **2015**, *119*, 6271−6279.
(37) Kiefer, L. M.; Kubarych, K. J. Solvent exchange in preformed photocatalyst-donor precursor complexes determines efficiency. *Chem. Sci.* **2018**, *9*, 1527−1533.
(38) Kashid, S. M.; Jin, G. Y.; Chakrabarty, S.; Kim, Y. S.; Bagchi, S. Two-Dimensional Infrared Spectroscopy Reveals Cosolvent-Composition-Dependent Crossover in Intermolecular Hydrogen-Bond Dynamics. *J. Phys. Chem. Lett.* **2017**, *8*, 1604−1609.
(39) Hamm, P.; Lim, M.; Hochstrasser, R. M. Vibrational energy relaxation of the cyanide ion in water. *J. Chem. Phys.* **1997**, *107*, 10523−10531.
(40) Czurlok, D.; Gleim, J.; Lindner, J.; Vöhringer, P. Vibrational Energy Relaxation of Thiocyanate Ions in Liquid-to-Supercritical Light and Heavy Water. A Fermi's Golden Rule Analysis. *J. Phys. Chem. Lett.* **2014**, *5*, 3373−3379.
(41) Dong, J. Y.; Hsu, Y. J.; Wong, D. S. H.; Lu, S. Y. J. Growth of ZnO Nanostructures with Controllable Morphology Using a Facile Green Antisolvent Method. *J. Phys. Chem. C* **2010**, *114*, 8867−8872.

https://doi.org/10.1021/acs.jpclett.1c02118
J. Phys. Chem. Lett. 2021, 12, 8784−8789